Structure and petrophysical properties of the Southern Chile subduction zone along 38.25°S from seismic data

von
Catalina Ramos

Dissertation
zur Erlangung des akademischen Grades
"doktor rerum naturalium"
(Dr. rer. nat.)
in der Wissenschaftsdisziplin Geophysik

eingereicht an der
Mathematisch-Naturwissenschaftlichen Fakultät
der Universität Potsdam

Potsdam, im September 2017

Structure and petrophysical properties of the Southern Chile subduction zone along 38.25°S from seismic data

Author: Catalina Ramos

First supervisor: Prof. Dr. Michael Weber
Second supervisor: Dr. James Mechie

Reviewers:
Prof. Dr. Michael Weber, Universität Potsdam, Germany
Prof. Dr. Charlotte Krawczyk, Technische Universität Berlin, Germany
Assoc. Prof. Dr. Eduardo Contreras-Reyes, Universidad de Chile, Chile

Published online at the
Institutional Repository of the University of Potsdam:
URN urn:nbn:de:kobv:517-opus4-409183
http://nbn-resolving.de/urn:nbn:de:kobv:517-opus4-409183

Erklärung

Hiermit versichere ich, dass ich die vorliegende Dissertation selbständig verfaßt und keine anderen als die angegebenen Hilfsmittel benutzt habe. Die Stellen der Arbeit, die anderen Werken wörtlich oder inhaltlich entnommen sind, wurden durch entsprechende Angaben der Quellen kenntlich gemacht. Diese Arbeit hat in gleicher oder änlicher Form noch keiner Prüfungsbehörde vorgelegen.

Catalina Ramos, Potsdam, September 2017

To Jorge and Geo

Acknowledgements

At this point, I would like to thank the people who made this academical achievement possible.

Firstly, no words are enough to thank James Mechie for all the support (academical, administrative and personal) during these years. There is no doubt I had an outstanding supervisor, who was there from the first e-mail we exchanged to answer my questions, guide me and advise me with his vast experience, showing his commitment for this research to be successful. Thank you for all I have learned from you, for your always constructive criticism and your infinite patience.

I thank Prof. Michael Weber for receiving me as a member of Section 2.2 at the GFZ, providing me of a place and equipment to carry out my research. To have a supervisor who always finds a moment to receive his students with a smile is encouraging. I also thank my colleagues from Section 2.2 and 2.7 for the nice work environment and for the constant good will to help me whenever I required it.

Manfred Stiller is thanked for his help with the TIPTEQ NVR data processing using ProMAX, for his very detailed answers (in person or via e-mail) whenever I had a question and for his never ending ideas to improve the seismic images.

Mei Feng is thanked for using her software to carry-out the one-step inversion of dispersion curves to obtain the 3D S-wave velocity model, as well as for her quick and detailed answers to each of my questions.

Christian Haberland is thanked for providing the 2D P-velocity and v p /v s models from local earthquake tomography, their respective uncertainties, as well as the local seismicity and for fruitful discussions about the interpretation of seismic velocity anomalies and the geometry of the upper-slab boundary in my region of research.

Klaus Bauer is thanked for his collaboration, applying his pre-stack line-drawing depth migration scheme on the TIPTEQ NVR data, which resulted in a reflectivity image that provided revealing information.

Thanks to Chris Irrgang for the German translations of the abstracts. If you ever do a second Ph.D. in a Spanish-speaking country I would be more than happy to translate your abstract.

The project TIPTEQ was funded by the German Ministry of Education and Research (BMBF), the German Research Foundation (DFG) and benefited from grants of the Free University of Berlin and the GFZ Potsdam. The instruments for the TIPTEQ experiments were provided by the Geophysical Instrument Pool Potsdam (GIPP) and the Free University of Berlin.

The German Academic Exchange Service (DAAD) supported me through the program "Forschungsstipendien für Doktoranden und Nachwuchswissenschaftler für mehr als 6 Monate".

The figures in this work were generated with Inkscape and GMT (Wessel et al., 2013).

Finally, I thank my family from the bottom of my heart, especially my parents Viviana and Boris. Please

receive this important achievement in my life as also yours, because I would not be writing these words, were it not for your invaluable dedication, sacrifice, efforts and above all, your love. Making you happy and proud is all I could wish for. I thank the company, the camaraderie and the many times I have laughed with Andrea, Teodoro, Pepa and Gastón. I really hold dear such moments. Be sure that even when we are so far away I always have you all in my mind and you can count on your big sister anytime ;)

To my beloved Jorge and Geo: the final product of these last four years of work is dedicated to you. Jorge, you have already heard me say that these have been the best years of my life, and it is so because you exist in my world. Thank you for letting me ride with you this crazy roller coaster called life and for being such a terrific partner in every possible way. I could not wish for more. Geo, your smile fills me with strength and motivation. It is worth every effort and it is my sunshine even in the darkest winter days.

Abstract

Active and passive source data from two seismic experiments within the interdisciplinary project TIPTEQ (from The Incoming Plate to mega Thrust EarthQuake processes) were used to image and identify the structural and petrophysical properties (such as P- and S-velocities, Poisson's ratios, pore pressure, density and amount of fluids) within the Chilean seismogenic coupling zone at 38.25°S, where in 1960 the largest earthquake ever recorded (M_w 9.5) occurred.

Two S-wave velocity models calculated using traveltime and noise tomography techniques were merged with an existing velocity model to obtain a 2D S-wave velocity model, which gathered the advantages of each individual model. In a following step, P- and S-reflectivity images of the subduction zone were obtained using different pre-stack and post-stack depth migration techniques. Among them, the recent pre-stack line-drawing depth migration scheme yielded revealing results. Next, synthetic seismograms modelled using the reflectivity method allowed, through their input 1D synthetic P- and S-velocities, to infer the composition and rocks within the subduction zone. Finally, an image of the subduction zone is given, jointly interpreting the results from this work with results from other studies.

The Chilean seismogenic coupling zone at 38.25°S shows a continental crust with highly reflective horizontal, as well as (steep) dipping events. Among them, the Lanalhue Fault Zone (LFZ), which is interpreted to be east-dipping, is imaged to very shallow depths. Some steep reflectors are observed for the first time, for example one near the coast, related to high seismicity and another one near the LFZ. Steep shallow reflectivity towards the volcanic arc could be related to a steep west-dipping reflector interpreted as fluids and/or melts, migrating upwards due to material recycling in the continental mantle wedge. The high resolution of the S-velocity model in the first kilometres allowed to identify several sedimentary basins, characterized by very low P- and S-velocities, high Poisson's ratios and possible steep reflectivity. Such high Poisson's ratios are also observed within the oceanic crust, which reaches the seismogenic zone hydrated due to bending-related faulting. It is interpreted to release water until reaching the coast and under the continental mantle wedge. In terms of seismic velocities, the inferred composition and rocks in the continental crust is in agreement with field geology observations at the surface along the profile. Furthermore, there is no requirement to call on the existence of measurable amounts of present-day fluids above the plate interface in the continental crust of the Coastal Cordillera and the Central Valley in this part of the Chilean convergent margin.

A large-scale anisotropy in the continental crust and upper mantle, previously proposed from magnetotelluric studies, is proposed from seismic velocities. However, quantitative studies on this topic in the continental crust of the Chilean seismogenic zone at 38.25°S do not exist to date.

Zusammenfassung

Innerhalb des interdisziplinären Projektes TIPTEQ (from The Incoming Plate to mega Thrust EarthQuake processes) wurden aktive und passive Quelldaten zweier seismischer Experimente verwendet, um die strukturellen und petrophysikalischen Eigenschaften (wie zum Beispiel P- und S-Geschwindigkeiten, Poissonsverhältnisse, Porendruck, Dichte und Flüssigkeitsmenge) in der chilenischen seismogenen Kopplungszone bei 38.25°S darzustellen und zu identifizieren, wo im Jahr 1960 das stärkste je gemessene Erdbeben (M_w 9.5) stattgefunden hat.

Zwei Modelle für S-Wellengeschwindigkeiten, basierend auf Techniken für Laufzeiten und Rausch-Tomographie, wurden mit einem existierenden Geschwindigkeitsmodell zu einem 2D-Modell für S-Wellengeschwindigkeiten verbunden, welches der Vorteile der einzelnen Modellkomponenten vereint. Im nächsten Schritt wurden verschiedene pre-stack und post-stack Techniken der Tiefenmigration verwendet, um Bilder der P- und S-Reflektivität zu erhalten. Von diesen Techniken hat das jüngste Schema der pre-stack Linienzug-Tiefenmigration die erkenntnisreichtsen Ergebnisse geliefert. Darauf aufbauend erlauben synthetische Seismogramme, welche die Reflektivitätsmethode verwenden, durch Eingabe der synthetischen 1-D P- und S-Geschwindigkeiten, auf die Komposition und auf Gesteine in der Subduktionszone rückzuschließen. Schließlich wird ein Bild der Subduktionszone gezeigt, welche die Ergebnisse dieser Arbeit im Zusammenhang mit weiteren Studien interpretiert.

Die chilenische seismogene Kopplungszone bei 38.25°S zeigt eine kontinentale Kruste mit sowohl hochgradig reflektierenden horizontalen als auch (steil) geneigten Strukturen. Unter diesen ist die Lanalhue-Bruchzone (LFZ), welche östlich abtaucht, auf sehr flache Tiefen abgebildet. Einige steile Reflektoren wurden zum ersten Mal beobachtet, zum Beispiel nahe der Küste verbunden mit hoher Seismizität, und nahe der LFZ. Steile oberflächliche Reflektivität hin zum vulkanischen Bogen konnten mit einem steilen westlich abtauchenden Reflektor verbunden werden. Dieser besteht wahrscheinlich aus Flüssigkeit oder geschmolzenem Material, welches sich durch Materialrecycling im kontinentalen Mantelkeil aufwärts bewegt. Die hohe Auflösung des S-Geschwindigkeitsmodells in den ersten Kilometern erlaubte es, mehrere sedimentäre Becken zu identifizieren, die sich durch sehr niedrige P- und S-Geschwindigkeiten, hohe Poissonsverhältinesse und mögliche steile reflektivität auszeichnen. Solch hohen Poissonverhältinesse wurden auch in der ozeanischen Kruste beobachtet, welche die seismogene Zone durch krümmungsverursachte Abbrüche hydriert erreicht. Das Wasser wird dabei an der Küste und unter dem kontinentalen Mantelkeil freigesetzt. Mit Hinsicht auf seismische Geschwindigkeiten stimmen die hergeleitete Komposition und Gesteinsverteilung in der kontinentalen Kruste mit geologischen Feldbeobachtungen an der Oberfläche des Profils überein. Des Weiteren zeigt sich keine Notwendigkeit für die Existenz von messbaren Mengen an gegenwärtigen Flüssigkeiten über der

Plattengrenze in der kontinentalen Kruste der küstennahen Kordilleren und dem Zentraltal in diesem Teil der chilenischen Konvergenzspanne.

Anhand der seismischen Geschwindigkeiten wird eine großskalige Anisotropie in der kontinentalen Kruste und im oberen Mantel vorgeschlagen, wie schon zuvor durch magnetotellurische Studien. Jedoch existieren bis heute keine Studien zu diesem Thema für die kontinentale Kruste der chilenische seismogenen Zone bei 38.25°S.

Contents

List of Figures

Chapter 1

Introduction

1.1 Overview

The largest earthquakes on Earth are known to be generated in subduction zones. The regions above subduction zones constitute one of Earth's most hazardous living environments due to the dangers posed by destructive earthquakes and volcanoes. Nevertheless, due to factors such as climate, resources and accessibility, such regions are often heavily populated. Thus, it becomes necessary to have a deep understanding of the structures and processes which shape the plate boundary region of a subduction zone. This is particularly true in the seismically coupled part of the subduction zone, where nearly all earthquakes with magnitude greater than 8 occur. One such area is the active continental margin of southern Chile, where on May 22, 1960 the largest earthquake ever recorded instrumentally (M_w 9.5) occurred (Kanamori, 1977).

With the aim of a better understanding of the structures, processes and petrophysical properties within the seismogenic coupling zone and with the possibility of improving the earthquake hazard assessment in southern Chile, several German and Chilean institutions have carried out collaborative projects in the region over the past 16 years, obtaining substantial knowledge with geophysical programs such as ISSA–2000 (Integrated Seismological experiment in the Southern Andes; Lüth et al., 2003; Bohm, 2004) or SPOC (Subduction Processes Off Chile; Krawczyk and the SPOC Team, 2003). The project SPOC, carried out in autumn 2001, was an amphibious seismic survey focused on the seismogenic coupling zone and the forearc in the southern central Chilean margin. It had a long-term vision, which was the quantitative understanding of mega-thrust earthquake seismicity in subduction zones and its relation to processes at depth and at the surface. At the same time, the experiments within the project, in particular an onshore seismic reflection profile served as a feasibility study for a subsequent project in the area called TIPTEQ.

The TIPTEQ project (from The Incoming Plate to mega-Thrust EarthQuake processes) was an integrated study carried out between the years 2004 and 2007 that aimed for the investigation of the structure and thermal state of the oceanic plate and the subduction zone, the composition and rheology of the subducting sediments, the seismicity, the nucleation of large subduction-related earthquakes, and the role of water in all of the above (Rietbrock et al., 2005; Scherwath et al., 2006). Project TIPTEQ comprised different multi-disciplinary subprojects, including active and passive source seismology onshore and offshore for structure and seismicity information, heat-flow measurements for thermal modelling, sediment probing

for compositional, chemical and mechanical properties, magnetotelluric soundings for subsurface resistivity and extensive multibeam bathymetric mapping throughout the entire survey area offshore (Scherwath et al., 2009, and references therein).

1.2 Tectonic setting

The study area is located at 38°15'S (Fig. 1.1). Here the Nazca plate subducts obliquely under the South American plate with a convergence rate of 6.65 cm a^{-1} at an angle of N82.4°E (Kendrick et al., 2003). The age of the oceanic crust that constitutes the Nazca plate at this part of the Chilean margin is ~25 Ma (Sdrolias and Müller, 2006). Perpendicular to the southern Chile margin, the western flank of the south-central Andes in the study area is subdivided from east to west in the Central Valley and the Coastal Cordillera. The Central Valley is a basin formed by Oligocene-Miocene sedimentary and volcanic rocks, covered by Pliocene-Quaternary sediments (Melnick and Echtler, 2006). In the Coastal Cordillera, composed mainly of metamorphic rocks, distinction is made between the western and eastern series, based on contrasting lithologies and tectono-metamorphic signatures. The western series, which is a Late-Carboniferous to Triassic basal-accretionary forearc wedge complex (Glodny et al., 2008), occurs southwest of 38.2°S. The main lithologies are meta-turbidites, chlorite schists and minor metabasites, with local occurrences of cherts, serpentinites and sulphide bodies (Hervé, 1988; Glodny et al., 2008). The eastern series, composed of Permian-Carboniferous magmatic arc granitoids and associated, frontally accreted metasediments (Hervé, 1988; Glodny et al., 2008), is located northeast of 38.2°S. The NNW–SSE striking, sinistral Lanalhue fault zone (LFZ) separates these two series. When subduction in this region initiated in the Late Carboniferous (around 300 Ma ago), the LFZ was a normal fault that separated the then exhuming western series from the frontally accreted eastern series. Later on, in the Early Permian, the segment of the western series-eastern series contact between 37°50'S and 39°45'S transformed into a sinistral, semi ductile to brittle strike–slip fault (Glodny et al., 2008). Seismicity along this fault indicates ongoing activity (Haberland et al., 2006).

1.3 TIPTEQ data

For this work, data from two experiments within TIPTEQ were used: TIPTEQ Seismic and TIPTEQ Seismology.

1.3.1 TIPTEQ Seismic

TIPTEQ Seismic was an active source experiment carried out in January 2005, consisting of a 95.5 km long west–east near–vertical incidence reflection (NVR) profile with explosive sources every 1.5 km at 38°15'S. It was the onshore extension of the northernmost of five marine corridors across the continental margin, that aimed to investigate the lateral variability of the processes active in the seismogenic coupling zone at the southern central Chile margin and related parameters and structures. This onshore transect crossed the hypocentre of the 1960 Valdivia earthquake. The experiment aimed at imaging and identifying the structural and petrophysical properties within the Chilean seismogenic coupling zone (e.g. compressional and shear wave velocities, density, pore pressure and friction) and identifying processes occurring in the vicinity of the

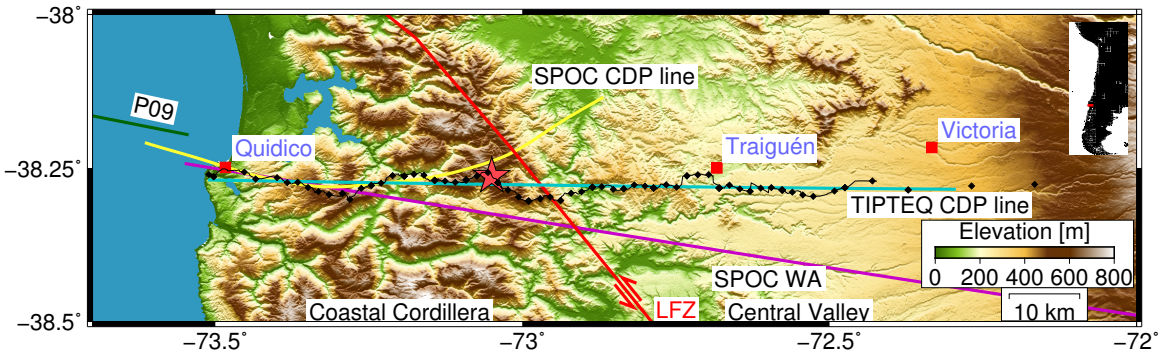

Figure 1.1: Location of the onshore active-source experiment of project TIPTEQ. Black line - receiver line; black diamonds - shot locations; cyan line - common depth-point (CDP) line of the TIPTEQ seismic reflection profile; red star - epicentral area of the 1960 Valdivia earthquake (Krawczyk and the SPOC Team, 2003). The yellow and magenta lines mark the CDP line of the SPOC onshore seismic reflection profile and the SPOC wide-angle refraction profile (SPOC WA), respectively (Krawczyk and the SPOC Team, 2003). The green line marks the easternmost part of the integrated TIPTEQ and SPOC near-vertical incidence reflection and refraction/ wide-angle reflection offshore profile (Contreras-Reyes et al., 2008a). The red line maps the surface trace of the Lanalhue fault zone (LFZ; after Melnick and Echtler, 2006).

subduction thrust such as compaction, lithification and dehydration. It provided high resolution reflection seismic images at this part of the margin for the first time (Groß et al., 2008; Micksch, 2008).

In this experiment, 104 shots (there were two misfires) were recorded by 180 3-component standalone instruments. The 104 shots comprised those from the near-vertical incidence reflection (NVR) and expanding spread profile (ESP) surveys and shots from a pilot study testing the generation of horizontally polarized shear (SH) waves using the Camouflet method (Dohr, 1985a). Fig. 1.1 shows the geographic location of the shots along the receiver line. See Micksch (2008) for further information about the experiment setup.

For the present work, the east-west and north-south components were used to pick shear wave traveltimes. These traveltime picks were then inverted using tomographic methods to obtain a detailed near-surface shear (S) wave velocity model. In a later stage, the NVR data were processed to obtain compressional (P) wave and S-wave reflectivity images along the profile. In the case of the P-waves, the data were reprocessed, starting with the results shown by Micksch (2008). The P-wave and S-wave reflectivity images obtained from the NVR data – more specifically the amplitudes and traveltimes of different reflectivity bands, in different parts of the TIPTEQ common depth point (CDP) line – were then used as parameters to model amplitude ratios utilizing synthetic seismograms calculated with the reflectivity method (Fuchs and Müller, 1971).

1.3.2 TIPTEQ Seismology

The second data set used in the present work belongs to a seismology experiment carried out between November 2004 and October 2005 between 37°S and 39°S, consisting of an exceptionally dense, temporary, amphibious seismic network at the south-central Chilean continental margin (Rietbrock et al., 2005; Haberland et al., 2006; see also Fig. 1.2). For this work in particular, the vertical component data from February to October 2005, recorded by 124 EDL data loggers were used to carry out a frequency-time analysis and

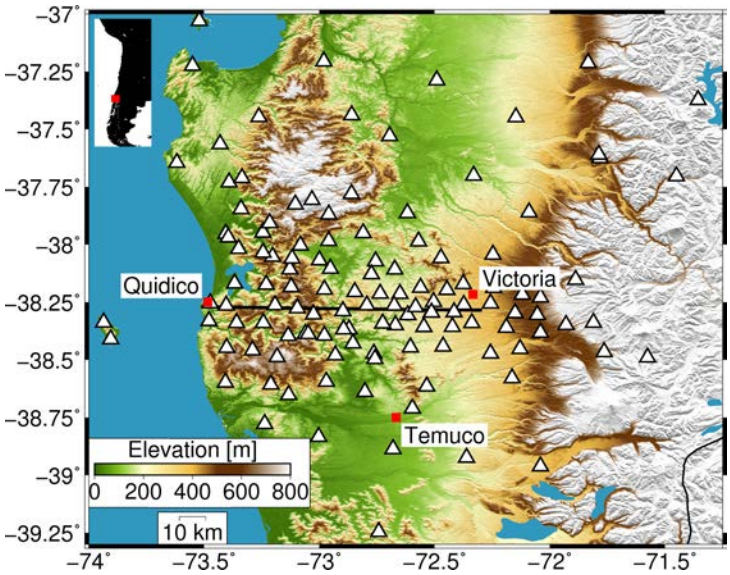

Figure 1.2: The 124 EDL stations from the TIPTEQ temporary array project distributed in southern Chile between 37°S and 39°S that collected the data used for the noise tomography. The black line is the CDP line of the TIPTEQ seismic reflection profile.

then a 3-D shear wave velocity tomographic inversion using the obtained dispersion curves. Average station spacing was around 7 km in the centre of the array and larger (40 km) in the outskirts of the region of interest. Further information about the TIPTEQ Seismology experiment can be found in Rietbrock et al. (2005), Haberland et al. (2006) and Haberland et al. (2009).

1.4 Description of this work

The overarching aim of this thesis is to have a detailed image and knowledge of petrophysical properties such as P- and S-wave velocities, Poisson's ratios, densities and amount of fluids, and to characterize the rock types within the Chilean subduction zone along an east-west profile that crosses the epicentre of the M_w 9.5 Valdivia earthquake at 38.25°S. For this purpose, active and passive source data from the project TIPTEQ were used. Tomographic techniques were implemented to obtain a shear-wave velocity model and a Poisson's ratio model along the study profile, S-wave and P-wave reflectivity images were obtained and the reflectivity method was used to obtain theoretical seismograms and to model amplitude ratios of different reflectivity bands along the profile. Finally, an integrative image of the study zone was obtained, correlating the results of this work with those obtained from other studies in this region and studies of other portions of the South-American convergent margin.

Chapter 2 describes the seismic tomography techniques used to obtain S-wave velocity models from the active and passive source TIPTEQ data, that is, traveltime tomography and noise tomography. The theory and principles of both tomographic techniques are briefly summarized. The data processing and the inversion procedure are discussed, as well as the different validation tests and the associated S-wave velocity uncertainties for each resulting velocity model. This chapter also presents the 2D S-wave velocity model constructed using three independently obtained S-wave velocity models that were merged together.

In Chapter 3 the processing of the NVR TIPTEQ data to obtain P- and S- reflectivity images is discussed. The three components of the NVR data are post-stack depth-migrated using the seismic processing software ProMAX. To process the vertical component, part of the processing done by Micksch (2008) is used, but to obtain a stack of phases instead of a stack of envelopes. This processing allows to present P- and S-stacked time sections and depth-migrated reflectivity sections. Additionally, a comparison of the obtained post-stack and pre-stack (after Bauer et al. 2013) reflectivity images is made, with a special focus in the imaging of steeper events.

Chapter 4 describes and applies the modelling of theoretical seismograms and amplitude ratios of pairs of reflections in two 1D profiles along the TIPTEQ CDP line, using the reflectivity method as described by Fuchs and Müller (1971). The chapter introduces the basic principles of the reflectivity method and discusses the numerical methods for the calculation of synthetic seismograms, the input synthetic 1D P- and S-wave velocity models as well as the different parameters, such as the number of ray parameters. It quantitatively discusses the differences in traveltimes and reflection amplitudes of seismograms when obtained using a flat layer model and a dipping layer model. The reflection amplitudes to be modelled are extracted from the P- and S-reflectivity images obtained in Chapter 3.

In Chapter 5, an integrative, updated image of the Chilean subduction zone along 38.25°S is obtained. The results obtained in the previous three chapters are correlated, interpreted and discussed with results from other studies in the region. Firstly, Poisson's ratio model along the TIPTEQ profile is obtained from the S-wave velocity model obtained in Chapter 2 and existent P-wave velocity models. The lithology, processes and presence of fluids in the subduction zone are discussed in terms of seismic velocities and Poisson's ratios. Furthermore, the results are correlated with data from studies such as local seismicity, reflectivity, magnetotellurics, gravity, water transport and field geology.

Chapter 6 summarizes the main results of this work and presents the final conclusions and implications of the results.

Three scientific publications from the results of this work were planned. Namely, Chapter 2 and part of Chapter 5 are included in Ramos et al. (2016). The reflectivity images using the post-stack migration technique (see Chapter 3), as well as Chapter 4 and the related final conclusions of this work in Chapters 5 and 6 were included in a manuscript recently submitted for publication. The P-reflectivity images from pre-stack migration (Chapter 3) are to be included in a manuscript to be submitted for publication.

Chapter 2

Seismic tomography techniques

Three independently obtained S-wave velocity models from different seismic tomography techniques were merged together to construct a final 2D S-wave velocity model along the east-west TIPTEQ profile. The resulting 2D S-wave velocity model was published in Ramos et al. (2016).

2.1 Traveltime tomography

The first velocity model was obtained using traveltime tomography, that is, through the inversion of S-wave traveltimes recorded on the horizontal components of the TIPTEQ active source data.

2.1.1 Theory

To obtain a S-wave velocity model using traveltime tomography, it is necessary to solve a forward problem (namely, to calculate synthetic traveltimes using an input subsurface S-wave velocity model, model parameters and source and receiver geometry) and an inverse problem (namely, to alter the input S-wave velocity model in order to minimize the differences between the obtained synthetic traveltimes and the measured traveltimes). Before the forward calculation, the initial S-velocity distribution of the study region is parametrised by rectangular blocks or grid nodes of constant size. In the method of Červený et al. (1977) irregular, rectangular blocks are used. In contrast, a more general parametrisation method is presented in Zelt and Smith (1992), where the velocity field is discretised into trapezoidal blocks (see Fig. 2.1). In the latter, the velocity within a trapezoid in the $x - z$ plane is

$$v(x, z) = \frac{c_1 x + c_2 x^2 + c_3 z + c_4 x z + c_5}{c_6 x + c_7} \tag{2.1}$$

where the coefficients c_i are linear combinations of the corner velocities (Zelt and Smith, 1992).

2.1.1.1 The forward problem

The forward part of the problem was solved by tracing rays through the medium using a finite differences approximation of the eikonal equation (Vidale, 1988; Podvin and Lecomte, 1991; Schneider et al., 1992).

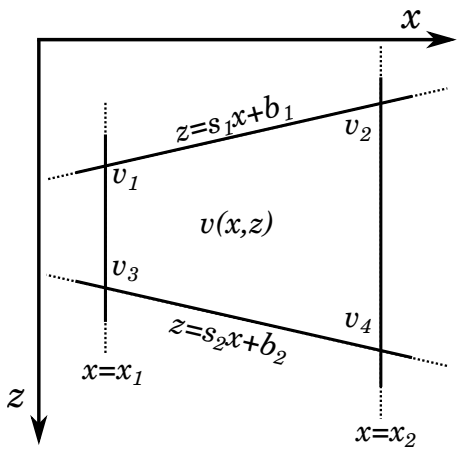

Figure 2.1: Velocity distribution $v(x, z)$ inside a model trapezoid, for a velocity field parametrisation after Zelt and Smith (1992). s_1 and s_2 are zero if a rectangle is used instead of a trapezoid.

The eikonal equation (Equation 2.2) is an approximation of the wave equation that describes the kinematic propagation of high-frequency waves.

$$|\nabla t(\mathbf{x})|^2 = s^2(\mathbf{x}) \tag{2.2}$$

Here $t(\mathbf{x})$ is the traveltime of the wavefront at point $\mathbf{x}$ and $s(\mathbf{x})$ is the slowness of the medium (inverse of wave velocity). One implication of Equation 2.2 is that if one knows s, there is a way to reconstruct the direction of the wave: this is the eikonal raytracing. Raytracing equations describe how energy continues in the same direction until it is refracted by velocity variations (Vidale, 1988). In the two-dimensional scheme described by Vidale (1988), a velocity structure is sampled at discrete points in two-dimensional space, with equal horizontal and vertical spacing and the source of seismic waves is assumed to be at a certain grid point (grid point A; see Fig. 2.2). The timing process is initiated by assigning point A a traveltime of zero. The four points adjacent to the point A, labeled B_1-B_4, are given the traveltimes

$$t_{B_i} = \frac{h}{2}(s_{B_i} + s_A) \tag{2.3}$$

where h is the mesh spacing, s_A is the slowness at the point A and s_{B_i} is the slowness at the grid point B_i being timed. Assuming nearly flat wavefronts, the traveltimes for the four corners $C_1 - C4$ in Fig. 2.2 are found through two formulas that extrapolate the traveltimes from three corners of a square to the fourth. For the upper-right corner in Fig. 2.2, the traveltimes between A, B_1, and B_2; t_0, t_{B_1} and t_{B_2}, respectively, and the origin are assumed to be known and t_{C_1} between C_1 and the origin is sought. For simplicity t_0 is zero since it is the traveltime of the source grid point (in general t_0 is not zero and A is not restricted to be the source point). For two-dimensional geometric rays in the $x - z$ plane, Equation 2.2 becomes

$$\left(\frac{\partial t}{\partial x}\right)^2 + \left(\frac{\partial t}{\partial z}\right)^2 = s(x, z)^2 \tag{2.4}$$

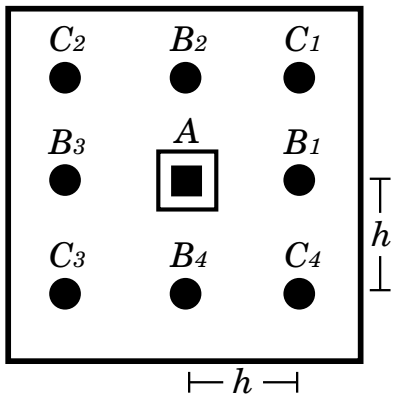

Figure 2.2: The source grid point A and the eight points in the ring surrounding it (Vidale, 1988).

The two differential terms in Equation 2.4 can be approximated with finite differences as

$$\frac{\partial t}{\partial x} = \frac{1}{2h}(t_0 + t_{B_2} - t_{B_1} - t_{C_1}) \tag{2.5}$$

and

$$\frac{\partial t}{\partial z} = \frac{1}{2h}(t_0 + t_{B_1} - t_{B_2} - t_{C_1}) \tag{2.6}$$

Substituting Equations 2.5 and 2.6 in Equation 2.4,

$$t_{C_1} = t_0 + \sqrt{2(hs)^2 - (t_{B_2} - t_{B_1})^2} \tag{2.7}$$

For a flat wavefront, this scheme gives a good and quick enough approximation of t_{C_1} (Vidale, 1988). After finding the times of the four corners ($C_1 - C_4$), the solution for this inductive scheme will progress by solving rings of increasing radius around the source point, proceeding first on the four sides sequentially, followed by the four corner points. The advantage of using finite differences to calculate traveltimes as in the scheme of Vidale (1988) is that it overcomes the difficulties with raytracing:

- For two points of interest, it finds the path with the minimum traveltime even for strongly varying velocity fields.
- It has a low computer cost.
- It finds the global minimum traveltime and corresponding raypath for pairs of points also in shadow zones.

This scheme gives the traveltime field for the whole model. As for the rays, needed to calculate the partial derivatives (see Equation 2.8), they can be determined by following the line of steepest gradient through the traveltime field from the receiver back to the source.

2.1.1.2 The inverse problem

For the inverse part of the problem, partial derivatives of the calculated traveltimes with respect to the velocity nodes were derived using the techniques described by Lutter et al. (1990) and Zelt and Smith

(1992). The inverse problem was solved by damped least-squares inversion (e.g. Zelt and Smith, 1992; Zelt and Barton, 1998).

The traveltime t of a seismic wave between a source and receiver along a raypath L for a continuous velocity field $v(x, z)$ is given by

$$t = \int_L \frac{1}{v(x,z)} dl \tag{2.8}$$

The discrete form, used in practical applications is

$$t = \sum_{i=1}^{n} \frac{l_i}{v_i} \tag{2.9}$$

where l_i and v_i are the path length and the velocity of the ith ray segment, respectively. Therefore, traveltime inversion is a non-linear problem (since the raypath is velocity dependent (Zelt and Smith, 1992)) which can be linearised using a Taylor series expansion about an initial model and dropping higher order terms, to obtain an iterative solution of the equation (Lutter et al., 1990; Zelt and Smith, 1992)

$$\mathbf{A}\Delta\mathbf{m} = \Delta\mathbf{t} \tag{2.10}$$

where $\mathbf{A}$ is the partial derivative matrix, $\Delta\mathbf{m}$ is the model parameter adjustment vector, and $\Delta\mathbf{t}$ is the traveltime residual vector. $\mathbf{A}$ contains the elements $\partial t_i/\partial m_j$, where t_i is the ith calculated traveltime and m_j is the jth model parameter selected for inversion (in this case it corresponds to velocity nodes).

The partial derivatives of traveltime with respect to velocity $\partial t_i/\partial v_j$ are calculated by velocity node perturbation using Fermat's principle (Lutter et al., 1990). From Equation 2.8

$$\frac{\partial t}{\partial v_j} = -\int_L \frac{1}{v^2}\frac{\partial v}{\partial v_j} dl \tag{2.11}$$

where v is the velocity of the unperturbed model along the ray, v_j is the jth velocity value selected for inversion and dl is the arc-length along the unperturbed ray. If using a velocity parametrization as the one in Zelt and Smith (1992), the partial derivative within the integral in Equation 2.11 can be evaluated using Equation 2.1.

The inverse problem is generally overdetermined, so Equation 2.10 is solved using the damped least-squares technique (Aki and Richards, 1980). The solution to Equation 2.10 is (Zelt and Smith, 1992)

$$\Delta\mathbf{m} = (\mathbf{A^T C_t^{-1} A} + D\mathbf{C_m^{-1}})^{-1}\mathbf{A^T C_t^{-1}}\Delta\mathbf{t} \tag{2.12}$$

where D is the overall damping parameter, and $\mathbf{C_t}$ and $\mathbf{C_m}$ are the estimated data and *a priori* model covariance matrices, respectively. They are given by

$$\mathbf{C_t} = diag\{\sigma_i^2\}, \qquad \mathbf{C_m} = diag\{\sigma_j^2\} \tag{2.13}$$

The standard deviation σ_i, is the estimated uncertainty of the ith traveltime measurement. σ_j is an *a priori* estimate of the uncertainty of the jth model parameter.

After ray tracing, the parameter adjustment vector $\Delta\mathbf{m}$, solved for in Equation 2.10 is applied to the current model. Afterwards, rays are traced through the updated model. This procedure is repeated until a satisfactory fit to the observed data is achieved or a prescribed stopping criterion is satisfied.

2.1.1.3 Damping factor and uncertainties

The overall damping parameter D in Equation 2.12 must be chosen to minimize the trade-off between spread of resolution and uncertainty of model parameters as well as the size of parameter adjustments (Lutter et al., 1990; Zelt and Smith, 1992)

The *a posteriori* model covariance matrix is given by

$$\mathbf{C} = (\mathbf{I} - \mathbf{R})\mathbf{C_m} \tag{2.14}$$

where $\mathbf{I}$ is the identity matrix (Tarantola, 1987). $\mathbf{R}$ is the model resolution matrix, given by (Zelt and Smith, 1992)

$$\mathbf{R} = (\mathbf{A^T C_t^{-1} A} + D\mathbf{C_m^{-1}})^{-1}\mathbf{A^T C_t^{-1} A} \tag{2.15}$$

By taking the square root of the diagonal elements of $\mathbf{C}$, the calculated standard error or uncertainties of the model parameters (velocities in this case) are obtained. The calculated errors represent a lower bound of the true parameter errors since they are due only to the uncertainties of traveltime picks and fail to account for the trade-off between model parameters as well as for other possible sources of error (e.g. phase misidentification, assuming a straight line for the receiver geometry, using an inappropriate model parametrization of the true earth). Therefore, the calculated error estimates are best used in a relative rather than absolute sense (Zelt and Smith, 1992).

2.1.1.4 Quantifying errors

To quantify velocity model errors for each iteration during the traveltime inversion, the root mean square (RMS) traveltime residual and the traveltime misfit χ^2 are calculated. χ^2 is a direct measure of the traveltime data misfit, in which misfits are inversely weighted with their standard errors (Nolet, 2008). It is given by (Stein and Wysession, 2009)

$$\chi^2 = \sum_{i=1}^{N} \frac{(t_i - t_i^m)^2}{\sigma_i^2} \tag{2.16}$$

where t_i^m are the traveltime data predicted by the model, t_i are the observed data, σ_i is the standard deviation (uncertainty) in observation i and N is the number of observations.

The reduced χ^2 (χ^2_{red}) is frequently used:

$$\chi^2_{red} = \frac{\chi^2}{N-1} \tag{2.17}$$

where $N-1$ is the number of degrees of freedom. If the model is a good fit of the data and the estimates of the uncertainties are reasonable, χ^2_{red} is expected to be around 1. Statistically, this means that there is a

reasonable possibility that the observed data are samples from a parent distribution described by the model, given the random uncertainties of measurement (Stein and Wysession, 2009). If χ^2_{red} is much larger than 1, it is unlikely that the data are samples of this distribution. On the other hand, a value of χ^2_{red} that is too small is also undesirable, since the data are unlikely to be fit that well. It means that the data are too well fit (overfit), with the given errors of measurement. This case is more likely to imply that the uncertainties in the data have been overestimated.

2.1.2 Data processing and inversion

The aim of the traveltime tomography using the TIPTEQ controlled source experiment data is to construct an image of the subsurface S-wave velocity structure. The resolution and depth extent of the obtained tomographic images are limited by the source-receiver geometry and the appropriate wavelength bandwidth. The software used for the tomographic calculations in this work has been developed in-house at the Deutsches GeoforschungsZentrum Potsdam over the past 20 years (e.g. EUROBRIDGE Seismic Working Group, 1999; Zhao et al., 2001; Weber et al., 2004; Mechie et al., 2009; Karplus et al., 2011; Mechie et al., 2012a,b; Ramos et al., 2016). The basic inputs needed to execute the software are the observed S-wave traveltimes, the geometry of sources and receivers and an initial S-wave velocity model.

2.1.2.1 Data acquisition and preparation

This is a brief summary about the TIPTEQ active source data acquisition and pre-processing. For a detailed description of the active source seismic experiment of project TIPTEQ see Micksch (2008), chapters 2 and 3.

The active source seismic experiment in TIPTEQ was conducted between the 13^{th} and 31^{st} January, 2005. The east-west trending profile line was at 38.25°S, between 73.5°W and 72°W, starting approximately in Victoria in the east to Quidico at the Pacific Ocean (see Fig. 1.1). Thus the profile was approximately 105 km long, along a so-called common depth point (CDP) line calculated with linear regression using GPS data along selected roads.

The source type in the experiment was explosive shots in boreholes of about 20 - 30 m depth and the experiment had three types of shot. The core experiment component was the near-vertical incidence reflection seismic profile (NVR), with 76 shots fired for this component, including three shots off the line in the east. The highest fold achieved was 8-fold. The second experiment component was designated the SH and aimed to generate horizontally polarized shear-waves in a pilot study using the Camouflet method (Dohr, 1985a). 13 additional shots were needed. The third experiment component consisted of an expanding spread profile (ESP), with 15 additional shots fired at certain offsets to the spread. In total, 104 shots were planned to be fired for all three experiment components. In the end, two misfires occurred.

955 receiver stations were used, each 100 m apart (projected on the CDP line). 180 stations, all with one 3-component geophone buried 20 - 40 cm deep, were deployed at once to form the active spread, giving a spread length of 18 km, which moved from east to west towards the ocean. The deployed receiver stations consisted of an earth data logger recording (EDL) unit, which recorded in miniSEED continuous data format (IRIS, 2008), with a sampling rate of 5 ms.

The raw data were converted into SEG-Y format (SEG, 2002) for further processing in the software ProMAX. Scripts and visual inspection helped to clear the data from faults. Shot gathers from the single traces were created with the help of lists of the sources and receivers. Inside ProMAX, trace header values were assigned for each data file for all three components. The geometry database was created loading the real field geometry. Traces with GPS timing errors were searched by hand and shifted about a mean value according to the neighbouring traces.

The sonic waves produced by the detonated blasting agent travelled along the active spread and were recorded by all the geophones. The airblast is removed from the data with the help of a surgical mute. The noise generated by cars passing by a receiver station was cut out (again using surgical mutes) when its amplitude exceeded the normal noise level. The elimination of high amplitudes at the beginning of the seismic signal (using a top mute), such as the first arrivals or guided waves was especially important for the processing necessary to carry out the stack and migration of the seismic data.

The ProMAX database was populated with values derived from geometry calculations and stored in parameters (e.g. parameter for source, trace, CDP, etc). The values in the database were used to check for plausibility and errors and afterwards, the geometry was matched to the corresponding data files.

2.1.2.2 Observed S-wave traveltimes

S-wave traveltimes were manually picked in the horizontal components (north-south and east-west) of 102 TIPTEQ shots using ProMAX. The two misfires were not used. There were a maximum of 180 traveltimes per horizontal component per shot to pick. However, this is in general not possible. Some difficulties in picking traveltimes are the existence of stations with no data because of disconnected geophones or stolen hard-disks (Micksch, 2008), noisy traces, small amplitudes and channels that are too close to the explosive source. Particularly for S-waves there are also interactions with earlier arrivals, such as converted waves and interactions with the P-coda.

The S-wave arrivals of the shots along the profile were in general of good quality. Applying a Butterworth bandpass filter (2 - 9 Hz) was enough to identify and pick most of the traveltimes. Unlike the filter used by Micksch (2008) to pick P-wave traveltimes (an Ormsby bandpass filter with corner frequencies 6 - 10 - 35 - 50 Hz), it was necessary to include lower frequencies to help attenuate earlier arrivals (see, for example, Fig. 2.3). Note that the filter does not completely eliminate earlier arrivals, especially in the ESP shot.

A total of 12,435 S-wave traveltimes were picked on the north-south component and 12,044 on the east-west component. They represent nearly 70% of the 18,360 possible picks. When there was a traveltime picked on both horizontal channels, the fastest was chosen for the tomographic inversion.

Fig. 2.4 shows all the picked S-wave traveltimes plotted with respect to the profile km (top) and the absolute offset (bottom). Traveltimes picked between 0 and 5 seconds correspond to those picked on NVR and SH shots. Traveltimes larger than 5 seconds correspond to ESP shots. As expected, the traveltimes, when plotted against absolute offset, lie more or less along a straight line. Increased traveltimes (above the line) may indicate the presence of sediments. Larger traveltime differences between both components may be the product of mispicked arrivals, especially for ESP shots. For example, for greater offsets the attenuation of higher frequencies becomes more important and it made the identification of the S-wave arrivals more difficult, especially if the signal-to-noise ratio was not very good for certain channels. Another

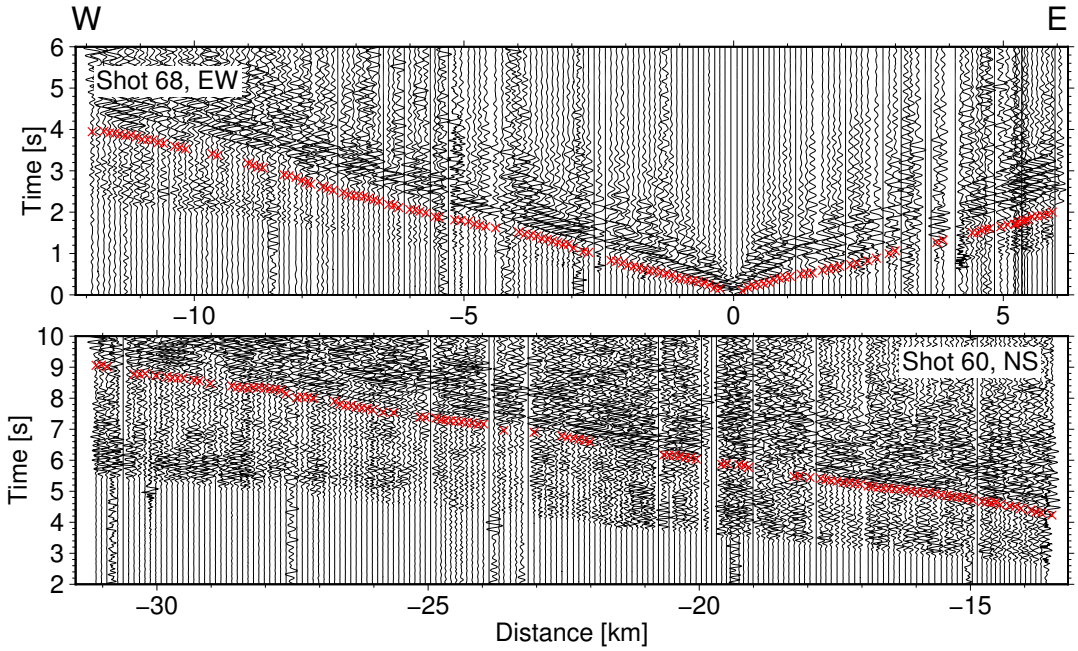

Figure 2.3: Two shots from TIPTEQ Seismic recorded by the 180 geophones. Top: Shot 68 (NVR, east-west component, location: 73.109°W, 38.274°S). Bottom: Shot 60 (ESP, north-south component, location: 72.787°W, 38.282°S). A bandpass filter (2 - 9 Hz) was applied to the data. Red dots: manually picked S-wave traveltimes.

explanation could be the presence of anisotropy, a point that is briefly discussed in Ramos et al. (2016). There is one study by Hicks et al. (2012) about mantle anisotropy for the TIPTEQ profile, but no such study exists for upper-crust anisotropy.

The traveltimes as well as the traveltimes uncertainties are exported out of ProMAX for the tomographic inversion. The latter were calculated from the ratio of the energy of the first arrival to the energy of the noise just before the first arrival.

2.1.2.3 Model setup and parameters

The seismic experiment done by Bräuer et al. (2007) with a geometry comparable to the TIPTEQ NVR setup resulted in tomographic images down to a depth of 1.5 km. The TIPTEQ ESP shots have a greater offset and thus a deeper ray penetration is achieved (maximum offset over 90 km, see Fig. 2.4, bottom).

The model size covers from -1 km above sea level to 25 km depth (positive direction downwards) and covers 130 km in the east-west direction. The origin is 10 km west from receiver 955 at the Pacific coast. The end is 120 km from the coast, in the Central Valley. The horizontal (east-west) spacing of the inversion nodes in the velocity model was 2 km and the vertical spacing was 1 km. An overall damping factor of 10 was chosen, allowing a rapid convergence between the theoretical and observed data without introducing significantly large model roughness. The *a priori* velocity uncertainty used was 0.2 km s^{-1}. The number of iterations used was eight, with very little improvement in the obtained RMS traveltime residual in further iterations.

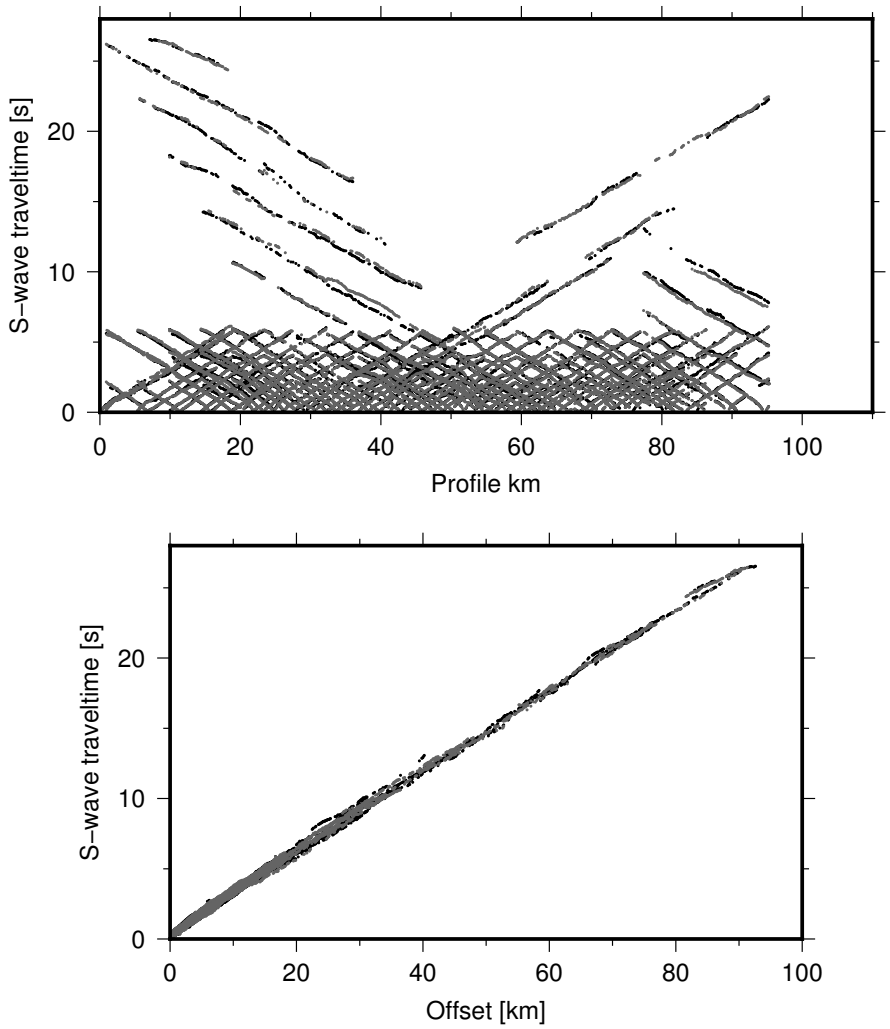

Figure 2.4: All picked S-wave traveltimes for the north-south component (black) and the east-west component (grey). Top: traveltimes versus profile km. Bottom: traveltimes versus absolute offset.

2.1.2.4 Initial velocity models

Different initial velocity models and damping parameters were tested for the tomographic inversion. The first initial model (a in Fig. 2.5) was a laterally homogeneous velocity model obtained by fitting a traveltime curve to the observed S-wave traveltimes. The damping factor was 40. Secondly (b), a lower damping factor of 10 was used for the same starting velocity model. Next (c), the initial model used by Micksch (2008) was used, divided by $\sqrt{3}$. This was a 1D P-wave velocity model based on the SPOC wide-angle model (Krawczyk and the SPOC Team, 2003) and extended into 2D. The damping factor was again 10. Lastly (d), the P-wave velocity model obtained by Micksch (2008) divided by $\sqrt{3}$ was tested. The damping factor was 10. Fig. 2.6 shows the RMS traveltime residual between observed and theoretical traveltimes and the traveltime misfit χ^2 for each obtained velocity model. Fig. 2.5 shows that the different starting velocity models produce similar structures along the east-west direction in the first kilometres depth. This was also observed by Micksch (2008) when testing different starting models. The effect of varying the

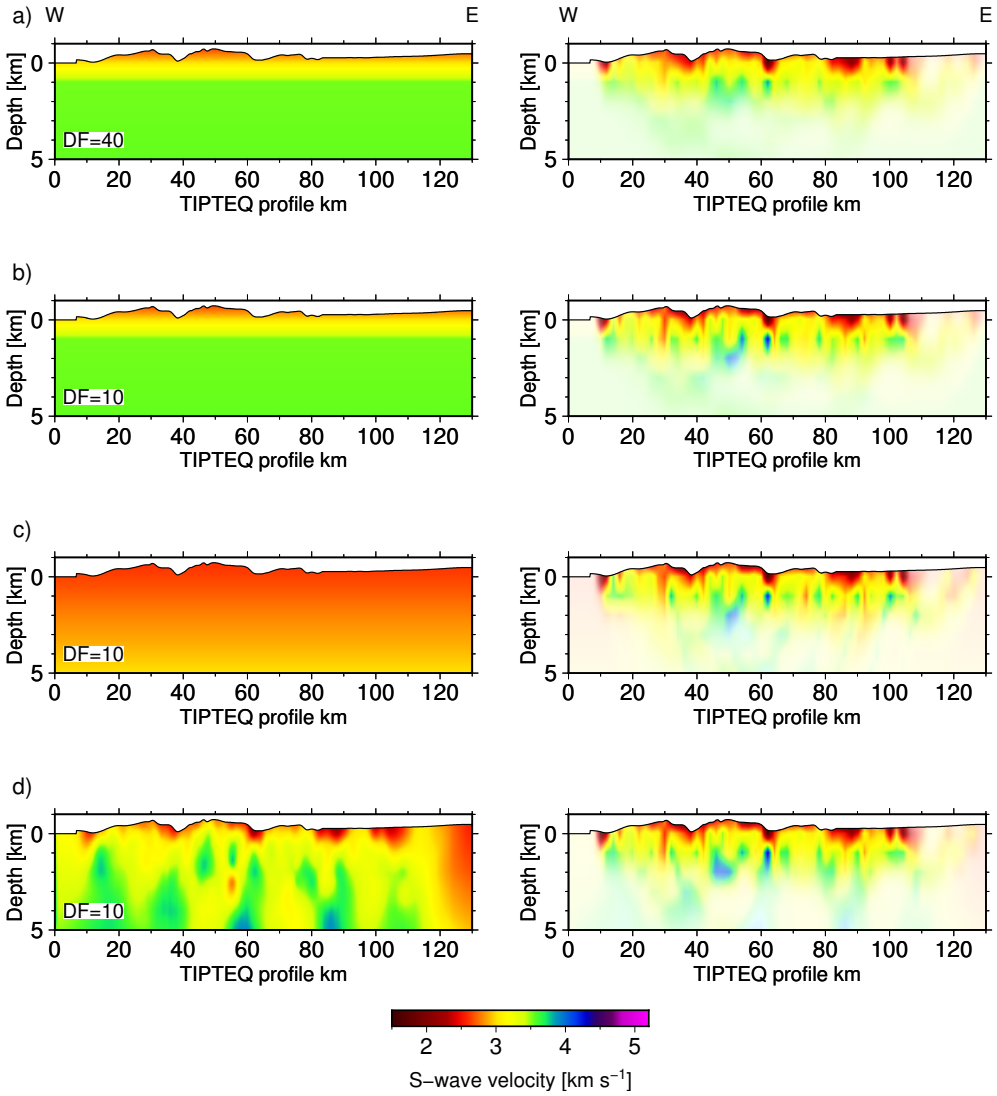

Figure 2.5: Left column: different initial models for the tomographic inversion. Right column: the corresponding S-wave velocity model obtained after eight iterations. Only the first 5 km depth are shown. Brighter regions have good ray coverage and are well resolved whereas fainter regions have poor ray coverage and are poorly resolved. DF: damping factor. The vertical exaggeration is 6:1. See text for more details.

damping factor (from 40 to 10) can be observed in the models obtained from the first and second starting models. Although both models produce similar velocity structures as mentioned above, the first results in a smoother model while the second produces more structural details.

The fourth initial model produces the lowest of all RMS residual values and thus it is the final chosen initial model. The χ^2 value of 0.72 is close enough to 1 to indicate that the data are adequately but not overfitted, especially if the *a priori* error estimates for the picked traveltime data have been a little overestimated.

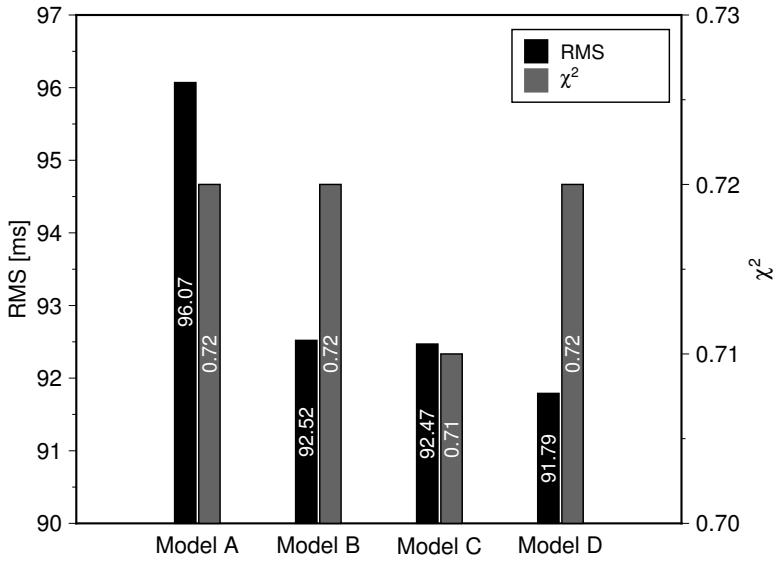

Figure 2.6: RMS traveltime residual and χ^2 for each starting model. The name of each model corresponds to the order shown in Fig. 2.5.

2.1.2.5 Results

Fig. 2.7 (middle) shows the final S-wave tomographic image. The figure shows a dense ray coverage (bottom) down to about 2 km below sea level (b.s.l.) between 20 and 110 km. As depth increases, the ray coverage becomes less dense, but there are some rays penetrating down to 7 km.

The resulting model shows many small-scale structures. Low S-wave velocity structures can be observed along the entire profile, just beneath the Coastal Cordillera and the Central Valley. Most of the velocity anomalies, especially in the upper 2 km can be recognized in the P-wave velocity tomography of Micksch (2008). Another feature that can be observed in the S-wave tomography (less prominent in the P-wave tomography) is the presence of vertical velocity anomalies. One such anomaly occurs at ∼30 km. To date, however, no reflected waves due to a vertical reflector have been observed in the TIPTEQ Seismic data.

2.1.3 Validation tests

2.1.3.1 Checkerboard tests

Checkerboard tests are commonly used to assess the ability of a tomographic inversion to resolve structural details in the earth (e.g. Zelt, 1998; Zelt and Barton, 1998; Van Wagoner et al., 2002). This approach consists of superimposing a small perturbation (e.g. a checkerboard pattern) over a simple initial velocity model, computing synthetic traveltime data using the same geometry of sources and receivers (a random number equal to less than the pick-error can be added to the traveltimes to simulate random errors in the actual observations), and then inverting the synthetic traveltime data in the same manner as the actual data. Finally, the initial model is subtracted from the inversion and the perturbations should be recovered if the ray coverage is sufficient to resolve the local structure (the perturbations, in this test).

Fig. 2.8 shows the results of the checkerboard resolution test using the TIPTEQ source-receiver geometry.

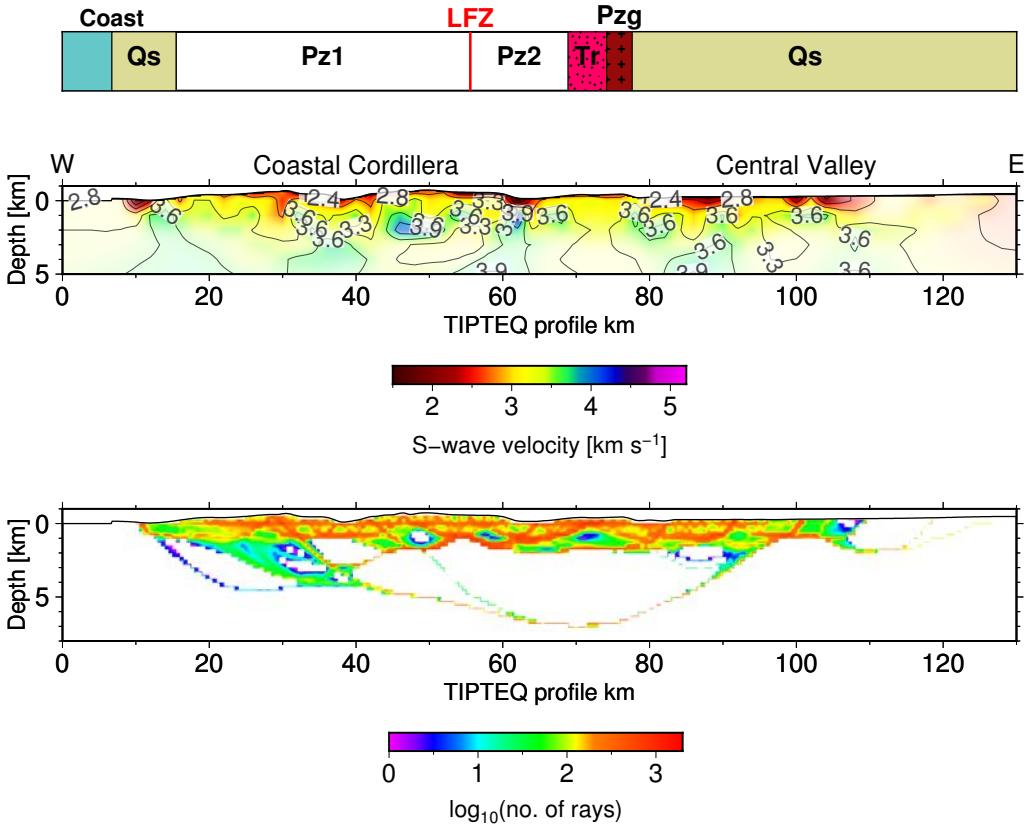

Figure 2.7: Top: geological strip map of the area after Melnick and Echtler (2006). Qs, undifferentiated sediments (Quaternary); Pz1, western series high-pressure meta-sediments and ultramafics (Permian-Triassic); Pz2, eastern series high-temperature meta-sediments (Carboniferous-Triassic); Tr, rift basin marine, continental and volcanic sequences (Triassic); Pzg, coastal batholith and undifferentiated intrusions (Paleozoic-early Triassic); LFZ, Lanalhue Fault zone. Middle: final S-wave velocity model, regions that have good ray coverage and are well resolved are shown. Vertical exaggeration is 2:1. Bottom: ray diagram.

It was mentioned that Fig. 2.7 (bottom) shows some rays penetrating down to 7 km depth. However, the checkerboard test with anomalies of 4 km by 2 km shows that such anomalies are only resolvable beneath the central part to almost 2 km depth and to almost 3 km depth between ∼20 and ∼45 km. Perturbations of 2 km by 1 km are also recovered in the first kilometre depth almost along the entire profile.

2.1.3.2 Model recovery test

This test is similar to the checkerboard tests. In this case, the input traveltime data for the inversion are derived by ray-tracing through the final velocity model (Fig. 2.7, middle). Random noise is again added to the traveltimes, similar to the checkerboard tests.

The model recovery test in Fig. 2.9, as well as the resolution tests with checkerboards, shows that the main characteristics in the final velocity model are recovered quite well. Although the resolution tests with checkerboards suggest that small-scale anomalies, such as the high-velocity anomaly at ∼62 km between 1 and 2 km depth are probably difficult to resolve, it is quite faithfully recovered by the model recovery test. The previously mentioned vertical velocity anomaly in Fig. 2.7 (middle) at ∼30 km is not completely

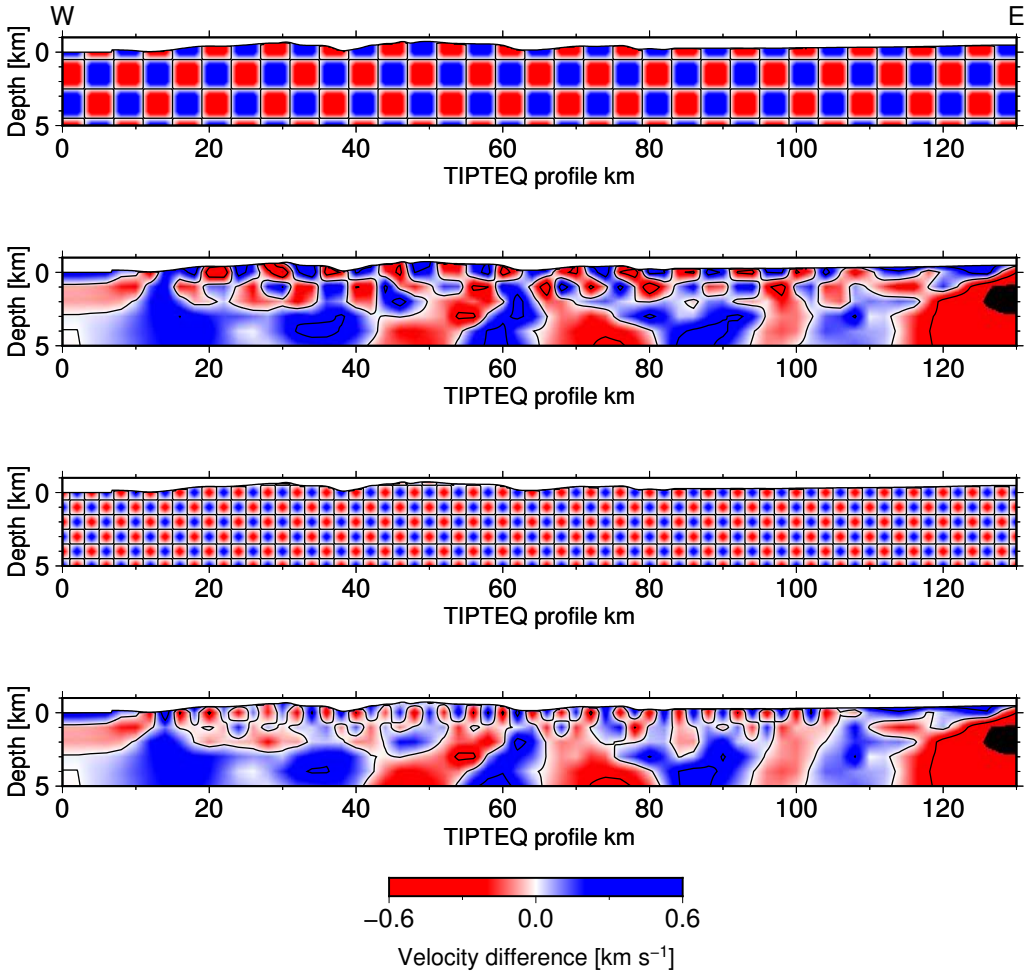

Figure 2.8: Top: original checkerboard anomalies of 4 km by 2 km and retrieved checkerboard anomalies. Bottom: original checkerboard anomalies of 2 km by 1 km and retrieved checkerboard anomalies. Amplitude of input anomalies: ± 0.3 km s^{-1} relative to reference velocity model. Contours drawn for 0 and ± 0.3 km s^{-1}. Vertical exaggeration is 2:1.

recovered.

2.1.4 Velocity uncertainties

During the inversion step a full matrix inversion was performed to determine the resolution matrix. This resolution matrix enables the assessment of the velocity model uncertainty (see Equations 2.14 and 2.15). An *a priori* estimate of the uncertainties in the velocities of 0.2 km s^{-1} was used (e.g. Harmon et al., 2013; Yang et al., 2015; Ramos et al., 2016). By taking the square root of the diagonal elements of the *a posteriori* covariance matrix (Equation 2.14), the calculated standard errors or uncertainties of the model parameters are obtained (Zelt and Smith, 1992).

Fig. 2.10 shows the velocity uncertainties for the final velocity model. Uncertainties range between 0.08 and 0.2 km s^{-1}, with the lowest values in the topmost part of the velocity model and coinciding with the well resolved area from the checkerboard tests (see Fig. 2.8). The factor that primarily contributes to larger

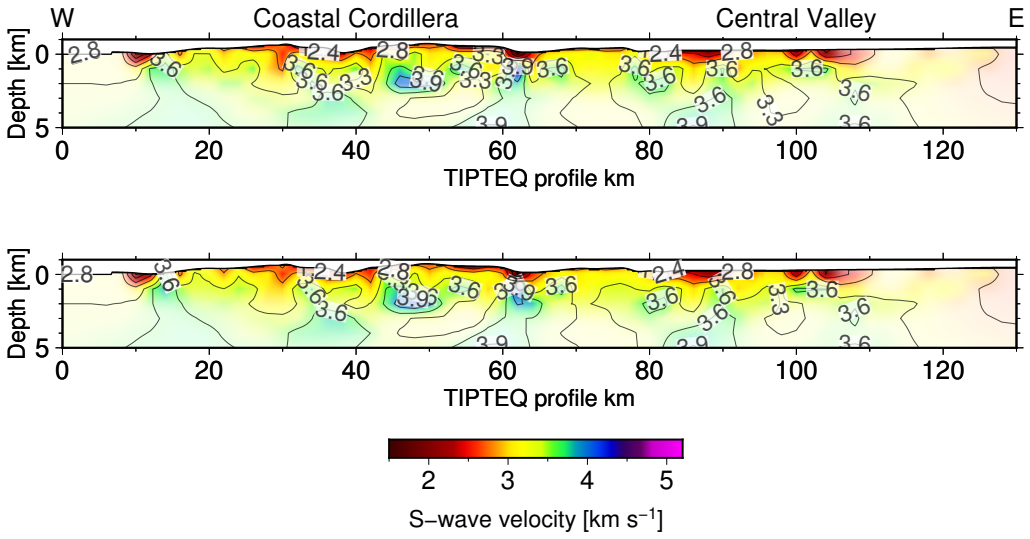

Figure 2.9: Top: Final S-wave velocity model. Bottom: Model recovery test. Vertical exaggeration is 2:1.

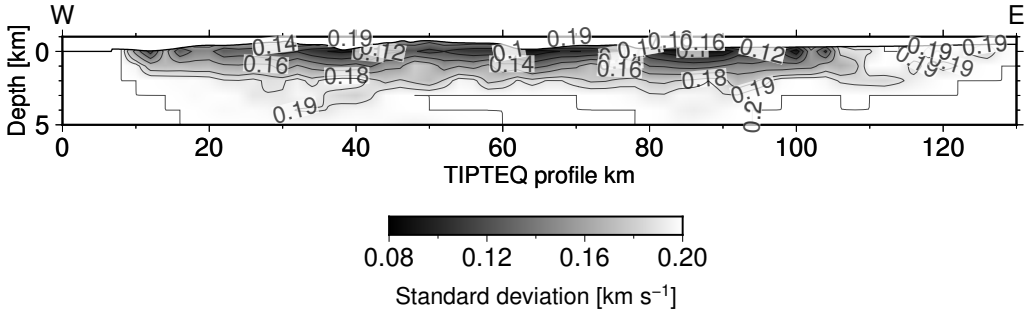

Figure 2.10: S-wave velocity uncertainties of the final model shown in Fig. 2.7. Vertical exaggeration is 2:1.

uncertainties is the small spacing of the inversion nodes in the velocity model.

2.2 Noise tomography

The second S-wave velocity model along the east-west TIPTEQ profile was obtained from data recorded by the temporary TIPTEQ seismology array. In this case, the data (recorded on the vertical component) are used to carry-out a dispersion analysis and then an inversion of dispersion curves to obtain a 3D S-wave velocity model.

2.2.1 Theory

Since the beginning of the 21^{st} century, the use of ambient seismic noise to characterize the subsurface velocity structure has been an extensively considered approach. Developments in acoustics and seismology (e.g. Weaver and Lobkis, 2001; Wapenaar, 2004; Snieder, 2004; Campillo and Paul, 2003; Shapiro and Campillo, 2004) demonstrated that, under the assumption that the sources of ambient noise are evenly distributed, the Green's functions (the response of earth to a perfectly known point source) can be measured

from the correlation of diffuse fields (in seismology, ambient noise and scattered coda waves). When computing cross-correlations of vertical component records of several days of seismic ambient noise at different pairs of stations, coherent broadband dispersive wavetrains emerge, with group velocities similar to those predicted for Rayleigh waves (Shapiro and Campillo, 2004). Using diffuse seismic wavefields has advantages relative to traditional surface wave measurements, as it is source independent, samples all directions, has localized sensitivity zones and measurements can be extended to shorter periods (Shapiro and Campillo, 2004). Surface waves of different periods are sensitive to seismic S-wave velocities at different depths, with the longer period waves exhibiting sensitivity to greater depths. Constraints can be determined on S-wave velocity structures of the crust and upper mantle by measuring the dispersive character of surface waves (Lin et al., 2007).

2.2.1.1 Dispersive nature of surface waves, phase and group velocity

Surface waves can be understood as a superposition of free oscillations, with their energy concentrated near the earth's surface. With a few exceptions (e.g. very deep earthquakes), fundamental-mode surface waves are the signal that dominates seismograms. Two types of surface waves propagate near the earth's surface: Love waves (resulting from SH waves trapped near the surface) and Rayleigh waves (a combination of P and SV motions that can exist at the top of a halfspace).

Surface waves are dispersive. This means that waves of different periods travel at different velocities. Dispersion is caused by the fact that higher frequencies are sensitive to shallow structures and lower frequencies to deeper structure such that different frequencies travel with different velocities.

To explore the dispersion concept, consider the simple example given by Stein and Wysession (2009): the sum of two harmonic waves with slightly different frequencies (ω_1 and ω_2) and wavenumbers (k_1 and k_2)

$$u(x,t) = \cos(\omega_1 t - k_1 x) + \cos(\omega_2 t - k_2 x) \tag{2.18}$$

The frequencies and wavenumbers can be written in terms of the differences from their average values ω and k:

$$\omega_1 = \omega + \delta\omega, \quad \omega_2 = \omega - \delta\omega, \quad \omega \gg \delta\omega \tag{2.19}$$

$$k_1 = k + \delta k, \quad k_2 = k - \delta k, \quad k \gg \delta k \tag{2.20}$$

Using this substitution in Equation 2.18, the two cosines are added, yielding

$$u(x,t) = 2\cos(\omega t - kx)\cos(\delta\omega t - \delta k x) \tag{2.21}$$

Both terms in Equation 2.21 correspond to propagating harmonic waves. Because $\delta\omega$ and δk are less than ω and k, respectively, the second term varies more slowly with time and space than the first. Thus there is a "carrier" wave with frequency ω and wavenumber k, on which a slower varying "envelope" with

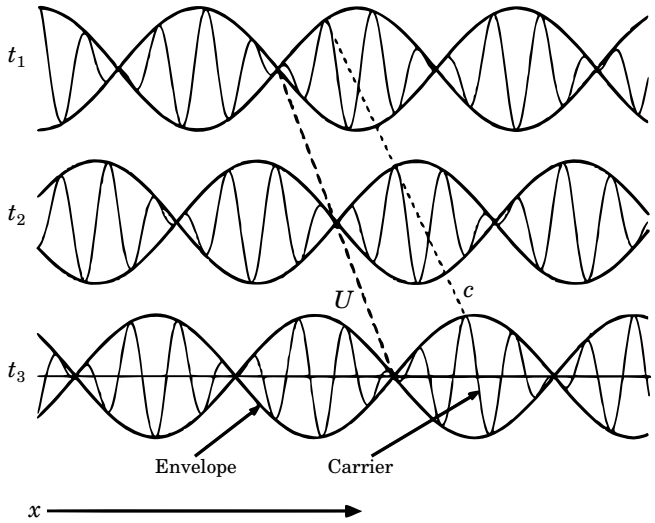

Figure 2.11: Comparison of group and phase velocities of the sum of two sinusoidal waves with slightly different frequencies and wavenumbers. Image from Stein and Wysession (2009).

frequency $\delta\omega$ and wavenumber δk is superimposed. The envelope propagates at the group velocity

$$U = \frac{\delta\omega}{\delta k}, \tag{2.22}$$

whereas the carrier moves at the phase velocity

$$c = \frac{\omega}{k}, \tag{2.23}$$

Phase velocity represents the speed at which a certain point in the waveform travels, while group velocity is the speed at which wave energy or a point on the envelope of the waveform travels. Comparison of the signal at different times (see Fig. 2.11) shows that the envelope propagates at a different speed from the carrier.

2.2.1.2 Correlation analysis

The correlation analysis is often used to measure the similarity between two signals. The cross-correlation of ambient seismic noise (or diffusive fields in general) recorded at two receiver locations results in the Green's function that describes the wave propagation between the two receivers that recorded the signals (Snieder, 2004).

The cross-correlation C of waves recorded at the receivers ψ and ξ over a time window of length T is given by

$$C(\tau) = \int_0^T \psi(t+\tau)\xi(t)dt \tag{2.24}$$

C measures the similarity between ψ and ξ by shifting ψ by different lag times, τ, and evaluating the integral of the product as a function of τ. The peak in C will be given for the time lag (or shift) τ that makes ψ and ξ more similar.

The real Green's function (G) however, can never be recovered completely, since the data recorded at the receivers are band-limited, which means that the highest and lowest frequency components of G are lost. Nevertheless, the derived cross-correlation will still be a good approximation of G (Wapenaar, 2004). Due to the nature of ambient seismic noise sources, Rayleigh waves tend to dominate the retrieved Green's function (Saygin and Kennett, 2010).

2.2.1.3 The multiple-filter method

The multiple-filter technique (Dziewonski et al., 1969) is a fast and efficient method to study variations of energy of a signal as a function of time (velocity) or period (frequency). Amplitudes and phases, as functions of period and velocity can be determined from a set of narrow-band digital filters. If ω_n denotes the centre frequency for the nth filter, the window function in the frequency domain with a truncated Gaussian function is

$$H_n(\omega) = \begin{cases} 0 & ;\text{for } \omega < (1 - BAND) \cdot \omega_n \\ e^{-\alpha\left(\frac{\omega-\omega_n}{\omega_n}\right)^2} & ;\text{for } (1 - BAND) \cdot \omega_n \leq \omega \leq (1 + BAND) \cdot \omega_n \\ 0 & ;\text{for } \omega > (1 + BAND) \cdot \omega_n \end{cases} \tag{2.25}$$

Here $BAND$ is the relative frequency bandwidth and $\alpha = \beta/BAND$, where β describes the decay of the window function and is determined by the desired value of the function at the band limits.

To study the dispersion characteristics of the surface waves emerging from the cross-correlation of ambient seismic noise, a frequency-time analysis with multiple filtering was carried-out to extract fundamental-mode group-velocity dispersion curves: a set of Gaussian filters as described in Dziewonski et al. (1969) (see Equation 2.25) is applied to the time series containing the surface waves. Next, the envelope function is calculated for the filtered signals. Each filtered envelope is tabulated in a time-frequency matrix (often called Gabor matrix), composing a whole column. The arrival of the fundamental-mode group velocities for each central period is calculated as the point of maximum envelope amplitude.

2.2.1.4 3D S-wave velocity model from fundamental-mode group-velocity dispersion curves

Surface-wave dispersion is non-linearly related to S-wave velocities beneath the raypath of the surface waves. The equations of the linearised approximation (e.g. Herrmann, 1978) have been widely used in surface-wave dispersion inversion from large-scale seismic lithospheric studies to local-scale studies (Feng and An, 2010 and references therein).

Unlike traditional schemes of inversion of dispersion for a 3D S-wave velocity model, which consist in two steps (period-by-period 2D tomographic inversions for regionalised dispersions and cell-by-cell inversions of regionalised dispersions for 1D S-wave velocity profiles), the scheme of Feng and An (2010), used in this work, combines the two-step inversion equations into one formulation to directly invert dispersion curves to 3D S-wave velocities. The method requires the pre-definition of 3D grids formed by 2D cells in the horizontal directions and 1D homogeneous layers in the vertical direction. This surface-wave tomography scheme is based on ray theory.

The traveltime t_m for the mth raypath can be expresed as the path length L_m divided by the group

velocity U_m of a certain period:

$$t_m = \frac{L_m}{U_m} = \sum_{i=1}^{nh} l_i(s_0 + \Delta s_i) \tag{2.26}$$

where l_i is the ray segment in the ith horizontal cell and nh is the total number of cells. The surface-wave group slowness (reciprocate of group velocity) of the ith cell can be considered as the sum of the slowness of the reference model s_0 and a slowness perturbation Δs_i. The latter is related to the S-wave velocity of the reference model (β) in the following linearised approximation:

$$\Delta s_i = \sum_{j=1}^{nz} \left(\frac{\partial s_0}{\partial \beta_{ij}} \Delta \beta_{ij} \right) \tag{2.27}$$

where $\partial s_0 / \partial \beta_{ij}$ is the partial derivative of the group slowness to the reference S-wave velocity, $\Delta \beta_{ij}$ is the S-wave velocity perturbation relative to the reference model for the grid-point located in the jth layer beneath the ith cell and nz is the total number of vertical layers in each cell. Substituting Equation 2.27 in 2.26:

$$t_m = \sum_{i=1}^{nh} l_i \left(s_0 + \sum_{j=1}^{nz} \frac{\partial s_0}{\partial \beta_{ij}} \Delta \beta_{ij} \right) \tag{2.28}$$

and subsequently

$$\sum_{i=1}^{nh} \sum_{j=1}^{nz} \left(l_i \frac{\partial s_0}{\partial \beta_{ij}} \Delta \beta_{ij} \right) = t_m - \sum_{i=1}^{nh} l_i s_0 \tag{2.29}$$

where, except for $\Delta \beta_{ij}$, all other parameters are known. Equation 2.29 only represents a linear constraint for one period in one surface-wave dispersion. By collecting many dispersions over more periods, a large number of linear equations similar to Equation 2.29 can be obtained. This can be expressed in matrix form as

$$\mathbf{G}\mathbf{x} = \mathbf{t} \tag{2.30}$$

where $\mathbf{G}$ is the large, sparse coefficient matrix, $\mathbf{x}$ is the vector of unknowns ($\Delta \beta_{ij}$) to be determined, and $\mathbf{t}$ is the vector of constants from group-velocity measurements.

In a linearised inversion, multiple iterations are normally required to approximate the real solution. However, synthetic tests run by Feng and An (2010), performed to assess the validity of this method show that only one run of inversion is enough to retrieve the first-order major structures of the true model, with only some minor improvement in subsequent iterations. A possible explanation to understand why the 3D inversion almost converges after only one run is that the sensitivity matrix $\mathbf{G}$ occurs in three dimensions consisting of not only a vertical component of linearised partial derivatives, but also a lateral component of linear ray-propagation constraints (Feng and An, 2010).

The scheme of Feng and An (2010) has advantages with respect to the traditional two-step dispersion inversion, namely:

- it reduces dramatically the computation time and the number of intermediate inputs and outputs (in both inversion and forward procedures) through the combination of many period-by-period 2D tomographic inversions into a single formulation. This facilitates synthetic tests and *a posteriori*

model appraisals.

- it enables the use of the first-order gradient of the parameters in the lateral and vertical directions as 3D smoothing constraints to construct a more physically reasonable model. This is because the parametrized model ($\Delta\beta_{ij}$) in Equation 2.29 (or $\mathbf{x}$ in 2.30) is defined in three dimensions.

This method has been used with regional and teleseismic data (Feng and An, 2010). It was applied for the first time in a small, local scale by Ramos et al. (2016).

2.2.2 Data processing

The high-resolution data of the TIPTEQ seismic array is an excellent resource to study the dispersion of surface waves using noise tomography (among other applications), and ultimately to obtain a S-wave velocity model. The software used for the dispersion analysis includes scripts to obtain the Green's functions from cross-correlations, and frequency-time analysis using the multiple-filtering method of Dziewonski et al. (1969). The chosen programming language to write the two scripts was Python, which has been used to create several seismology tools, such as ObsPy (Beyreuther et al., 2010) and MIIC (Monitoring and Imaging Based on Interferometric Concepts; Sens-Schönfelder et al., 2014), both used in this work. For this study, both the one-step and two-step methods to invert dispersion data to S-wave velocities use the software surf96 (Herrmann, 2013).

2.2.2.1 The seismic array

The TIPTEQ seismology array was a large-scale amphibious experiment deployed from November 2004 until October 2005, aiming to study the fine-scale structure ($<$2 km) of the seismogenic coupling zone around the nucleation area of the 1960 Valdivia earthquake (Rietbrock et al., 2005). The array was designed for high-resolution analysis of local seismicity.

It had a dense station spacing (less than 7 km in the centre), less dense in the outskirts of the region of interest (40 km) and accurate time basis (from GPS), collecting a unique dataset of local seismicity of the Wadati-Benioff zone, as well as regional and teleseismic events (Rietbrock et al., 2005; Haberland et al., 2009). The array covered an area of 250 $\times$ 250 km onshore and extended offshore to the trench. In latitude, it covered the entire forearc between 37°S and 39°S (see Fig. 1.2).

The data were recorded continuously. Between October 2004 and January 2005 the array consisted of 70 PDAS and REFTEK data loggers, being replaced by EDL data loggers between February and June 2005. An additional 50 EDL stations were deployed to increase the station density. Between February and October 2005 10 wide-band ocean bottom seismometers (OBS) and hydrophones (OBH) complemented the network on the offshore forearc (Haberland et al., 2009). All stations were equipped with short-period Mark L4C-3D 1-Hz three-component sensors.

The data used for this work were recorded by 124 EDL data loggers and were kindly provided by Dr. C. Haberland (GFZ, Section 2.2).

2.2.2.2 Cross-correlation of ambient seismic noise from the TIPTEQ array

The vertical components of the 100 Hz data from the 124 EDL stations were cross-correlated following Bensen et al. (2007). Fig. 2.12 summarizes the scheme to process the data. The instrument response was

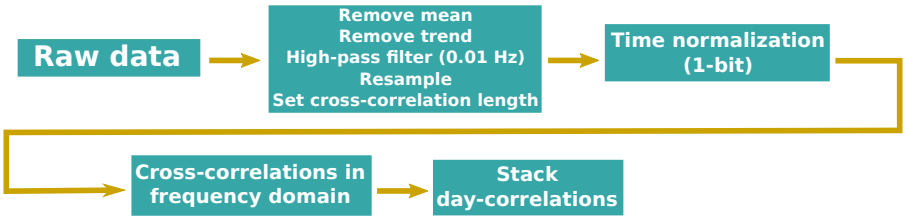

Figure 2.12: Scheme used to compute cross-correlations using ambient seismic noise recorded by the 124 EDL stations.

not removed, as the 124 stations were all EDL data loggers with Mark 1-Hz seismometers and thus all had the same response function. A high-pass filter removed possible very low frequency signals. The sampling frequency of the data was decreased to save computation time. For a small inter-station distance it does not take long to observe the Rayleigh waves in the daily stacked cross-correlation function and thus a small number of lags is enough to observe them. For this reason, the length of the cross-correlation was set as a function of the inter-station distance. The cross-correlations for both positive and negative time lags were computed using the convolution theorem, which calculates the cross-correlation function using the Fourier transform as (Bracewell, 1999)

$$\psi \star \xi = \mathcal{F}^{-1}(\mathcal{F}(\psi) \cdot [\mathcal{F}(\xi)]^*) \tag{2.31}$$

where the star symbol denotes the cross-correlation operation and the asterisk denotes the complex conjugate of $\mathcal{F}(\xi)$. The fast Fourier transform (FFT; Cooley and Tukey, 1965), saved computer time since the execution of the FFT algorithm is usually several times faster than the corresponding convolution in the time domain, for the same precision. A cluster of computers at GFZ, Section 2.2 was used to simultaneously calculate groups of cross-correlations in an automated way, thus saving several days of calculation time.

From the 124 EDL stations, 7542 daily stacked correlations were obtained (see examples in Fig. 2.13). For some pairs of stations there were no data in the same time period, thus making it impossible to correlate data for such station pairs. In Fig. 2.13, it is possible to observe the dispersion of the Rayleigh waves, as well as the attenuation of higher frequencies as the inter-station distance increases. The source of ambient noise in this case lies primarily in the Pacific ocean.

2.2.2.3 Frequency-time analysis with multiple filters

The multiple-filtering method of Dziewonski et al. (1969) was applied to obtain 50 different filters with different bandwidths between 1 and 50 s. The envelopes of the filtered Green's functions were calculated and for each of them, the arrival time of the Rayleigh wave at the relevant period was calculated as the point of maximum envelope amplitude (see an example in Fig. 2.14). The frequency-time analysis usually showed surface-wave signals up to a period between 13 and 15 s (depending on the signal-to-noise ratio), losing seismic energy for longer periods. From the sensitivity of surface waves to S-wave velocities, a good

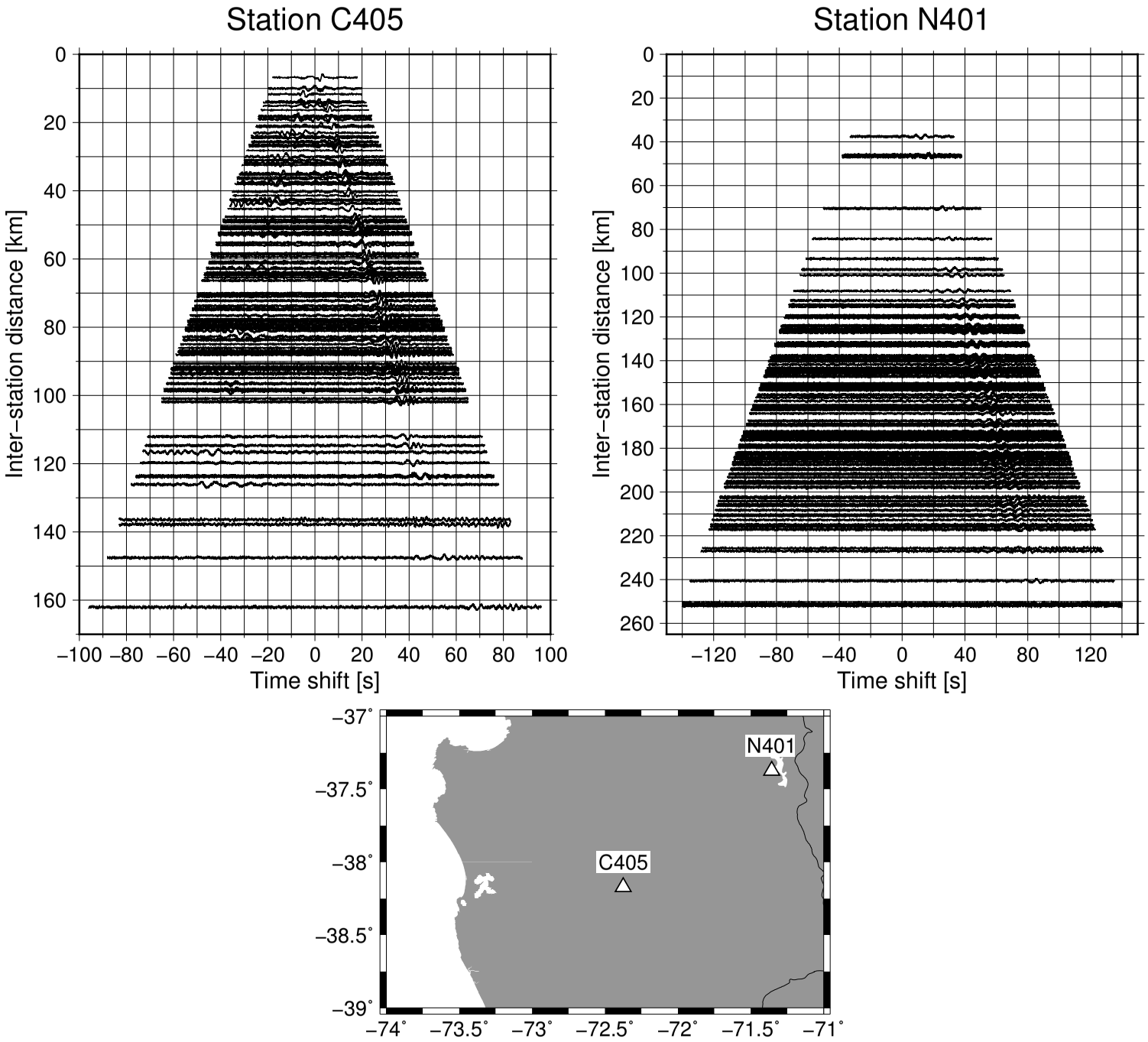

Figure 2.13: Unfiltered Rayleigh waves from the cross-correlation of ambient seismic noise for stations C405 and N401 with the other stations of the array. The map shows the locations of the stations.

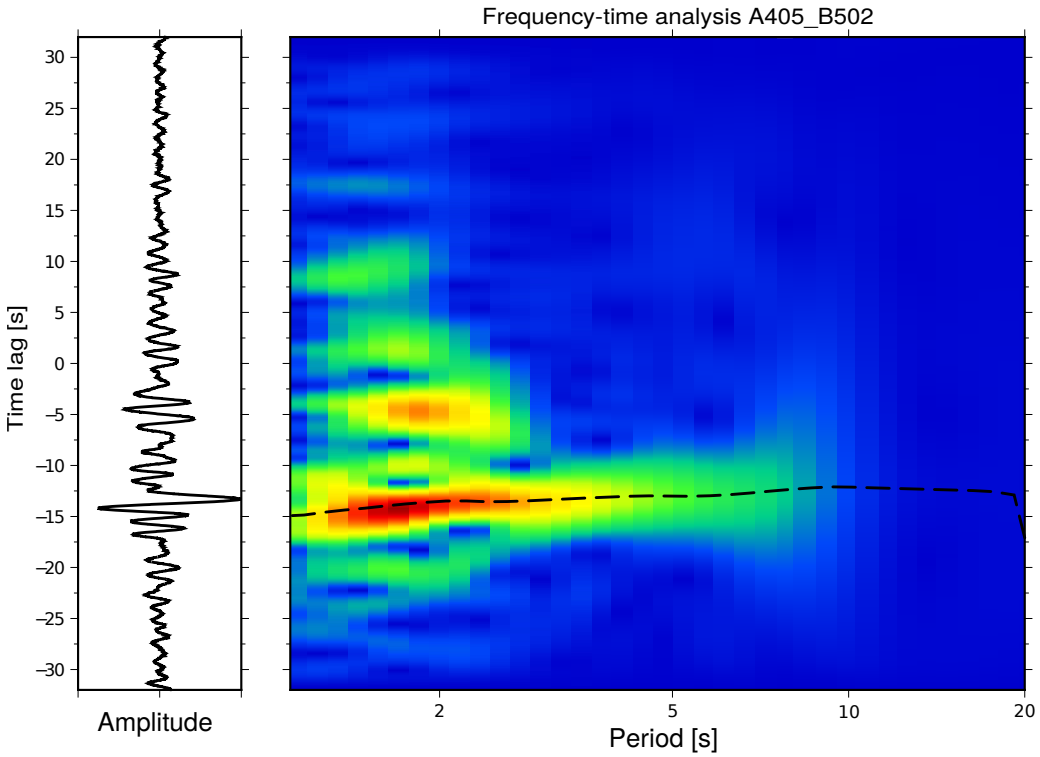

Figure 2.14: Left: day-stacked cross-correlation for stations A405 and B502 (interstation distance: 34.11 km). Right: frequency-time analysis with multiple filters. The black dashed line represents the measured fundamental-mode group speed curve.

resolution in depth goes down to about one third of the wavelength (e.g. Forsyth et al., 1998; Yang and Forsyth, 2006). Thus, assuming a surface-wave group velocity of ~ 3.5km s^{-1} (Ramos et al., 2016) there should then be a good resolution down to a depth of approximately 17.5 km in the tomographic inversion. For the 50 picked traveltimes per cross-correlation, the traveltimes shorter than the central period of the applied filter were automatically discarded. When the signal-to-noise ratio was less than 1, the traveltime was also discarded. For the tomographic inversion 19 periods in the range between 2.41 and 15.1 s were used, which is large enough so that the dispersion curve is adequately defined.

2.2.2.4 Two-step inversion of dispersion curves to 1D S-wave velocity profiles

A first attempt to obtain S-wave velocities from dispersion measurements was made with the traditional two-step method. Firstly, the dispersion data are inverted to obtain 2D surface-wave velocity models for each period and afterwards, the surface-wave velocities are used to obtain 1D S-wave velocity models. The processing of dispersion measurements for surface-wave tomography is the same as for S-wave traveltimes (Section 2.1.1), with the difference that in this case the inversion gives surface-wave velocities and in the horizontal space, for each of the 19 inverted periods.

The inversion region was defined so that it covered all the stations of the array: 260 km in the north-south direction, approximately between 37 and 39.3°S, and 240 km in the east-west direction, approximately between 71 and 74°W. The spacing of the inversion nodes in the velocity model was 10 km in both horizontal

directions. An overall damping factor of 40 was chosen and eight iterations, with very little improvement in the RMS in subsequent iterations, were tested.

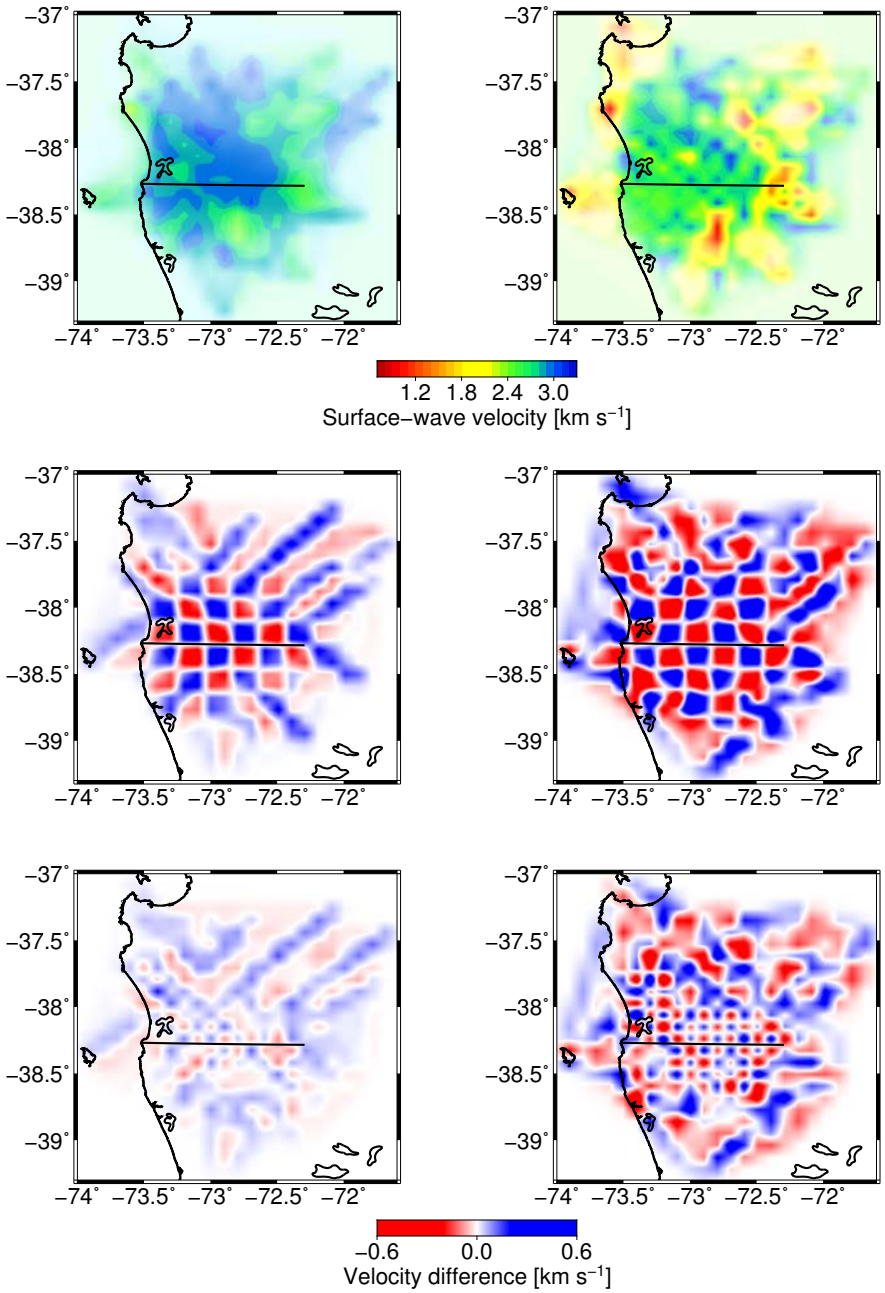

Figure 2.15: Surface-wave tomographic images obtained from the dispersion measurements, and their respective resolution tests for the periods 6.8 s (left) and 2.82 s (right). The upper resolution tests use checkerboards of 20 x 20 km. The lower use checkerboards of 10 x 10 km. Black line: TIPTEQ CDP line.

The reference velocity models used in the inversion were always of constant value. These constant velocity values were calculated from the inverse of the slope of a linear least-squares regression, calculated through the traveltime versus distance data for each period. A traveltime residual was calculated between the observed data and the regression line. Additionally to the previously discarded traveltimes, those with a

traveltime residual larger than the RMS of all the residuals were discarded.

Fig. 2.15 shows an example of inverted surface-wave velocity models for the periods 6.80 s and 2.82 s. It is possible to observe the dispersive character of the surface waves, as the lower period has higher velocities. Appendix A shows the constant reference velocities and number of dispersion measurements used for the inversions, as well as the RMS and χ^2 values for the best model, for each period.

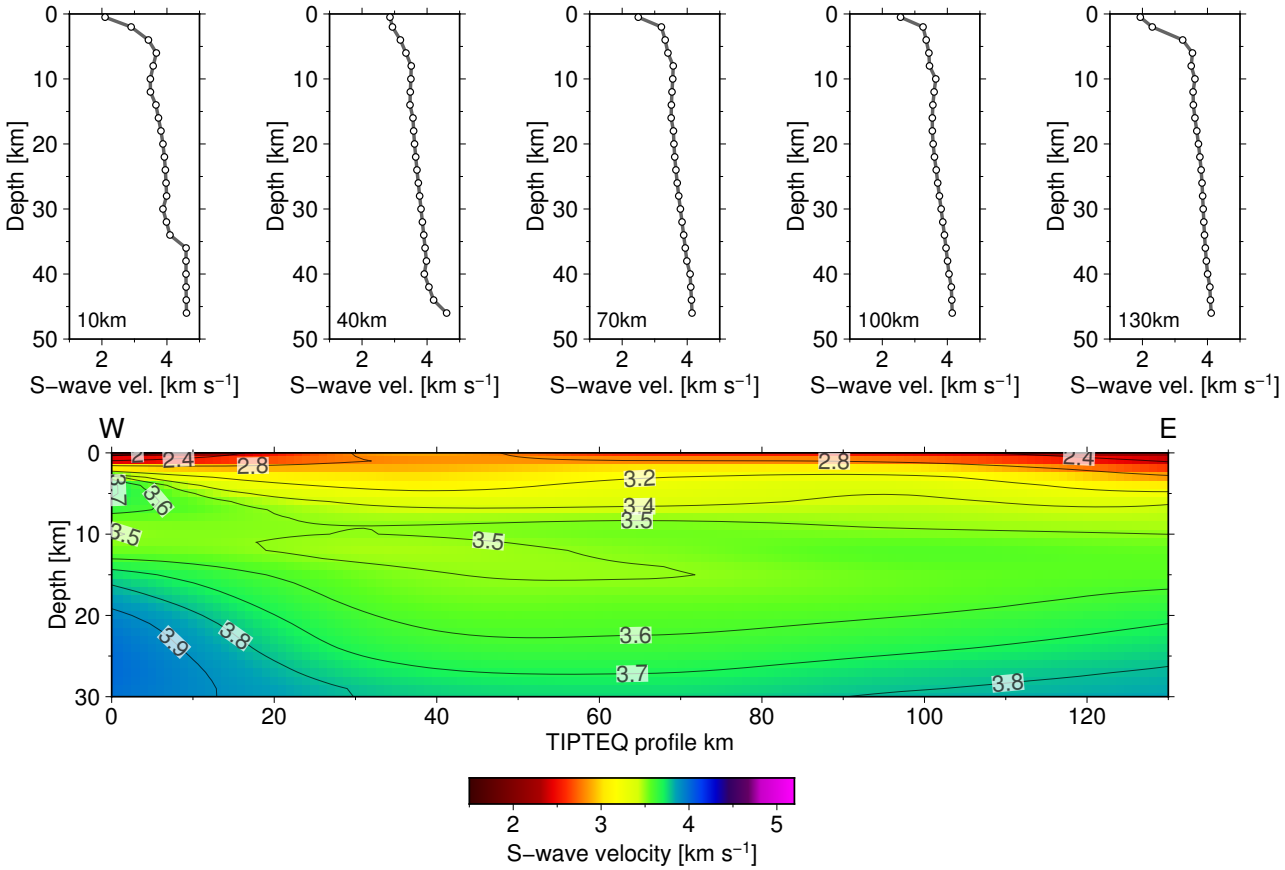

Figure 2.16: Top: 1D S-wave velocity models at 10, 40, 70, 100 and 130 km along the TIPTEQ profile, obtained from the two-step dispersion data inversion method. Bottom: 2D S-wave velocity model obtained from the interpolation of the 1D velocity models. Vertical exaggeration: 1:1.

To invert the surface-wave velocities to 1D S-wave velocities the inputs are a reference S-wave velocity model, which in this case is the P-wave velocity model from the SPOC wide-angle data (Krawczyk and the SPOC Team, 2003) divided by $\sqrt{3}$, and the surface-wave velocities along the TIPTEQ profile for the 19 periods. The surface-wave velocities are extracted from the 19 velocity models every 10 km along the profile. The output 1D S-wave velocity models reaches the same depth and has the same spacing of the inversion nodes as the input reference velocity model (in this case eight iterations were used). In this case, this is a depth of 50 km and 2 km nodal spacing. Finally, the 1D S-wave velocities are interpolated along the TIPTEQ profile to obtain a 2D S-wave velocity model (Fig. 2.16).

2.2.2.5 One-step inversion of dispersion curves to 3D S-wave velocity model

A direct dispersion data inversion for 3D S-wave velocity structure after Feng and An (2010) was kindly provided by Dr. M. Feng (Institute of Geomechanics, Chinese Academy of Geological Sciences), applying the method to such a small-scale study area for the first time (Fig. 2.17). Additionally to the previously

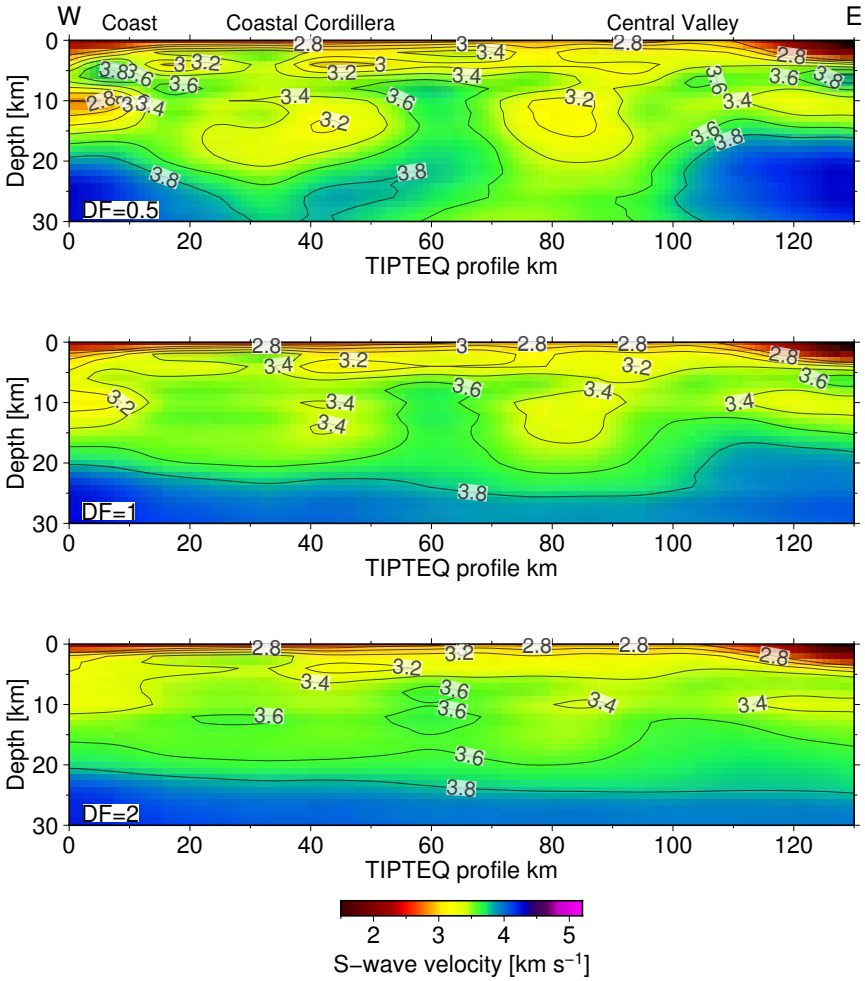

Figure 2.17: 2D S-wave velocity slices from 3D S-wave velocity model along the TIPTEQ profile, for different damping factors (DF). Vertical exaggeration: 1:1.

discarded traveltimes, if the traveltime error divided by the traveltime was larger than 15%, such data were excluded. Finally, data with an interstation distance shorter than twice the wavelength (λ) of the signal being considered were also removed, leaving a total of 91,276 dispersion measurements for the inversion. The study region was defined between 74°W and 71°W longitude, 37°S and 39.4°S latitude and 0 - 60 km depth, with a cell size of 0.1° in longitude and latitude and 2 km in depth. The reference model is interpolated from CRUST1.0 (http://igppweb.ucsd.edu/~gabi/rem.html). Different damping factors were tested, namely, 0.5, 1 and 2. The slice corresponding to the profile along the CDP line of TIPTEQ, taken from the resulting 3-D S-wave velocity model can be seen in Fig. 2.17.

Both, the one-step and two-step inversions to S-wave velocities yield similar results. Either of the

resulting velocity models can be chosen to be merged with the other models. In this case, the model from the one-step inversion method was chosen because the selection of the dispersion data used in the inversion was more restrictive.

2.2.3 Validation tests

Resolution tests using checkerboards were carried out (see Fig. 2.18). A comparison of the RMS misfit of group velocities for the inverted velocity models with each damping factor (Fig. 2.19) shows no significant differences in the RMS misfit for the different damping factors. Thus, finally, the damping factor of 2 was selected, as this produced the smoothest velocity model.

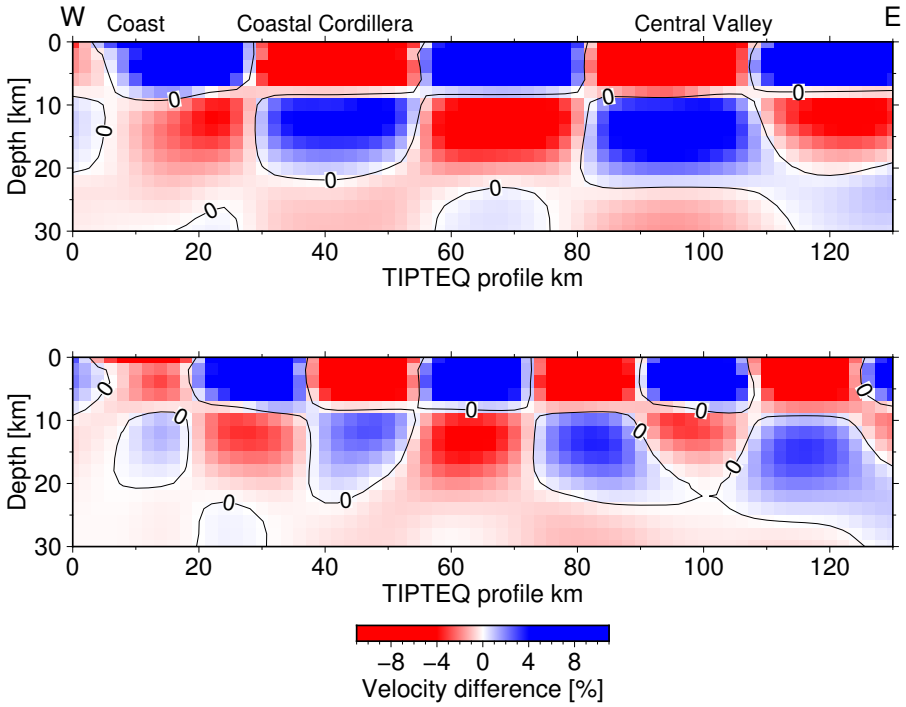

Figure 2.18: Resolution tests using checkerboards for the S-wave velocity model along the TIPTEQ CDP profile. Top: Checkerboards of 30 x 10 km. Bottom: Checkerboards of 20 x 10 km. Amplitude of input anomalies: ±7% relative to the reference velocity model. Vertical exaggeration: 1:1.

The selected velocity model (Fig. 2.17, bottom) shows a relatively smooth transition from velocities of 3.2 km s $^{-1}$ near the surface to 3.6 km s $^{-1}$ at ∼17 km depth beneath the Coastal Cordillera. At both ends of the profile, beneath the Central Valley and the coastal plain, lower velocities occur near the surface where larger accumulations of sediments and / or volcanics occur.

The shortest period used in the surface wave tomographic inversions (2.40 s) gives an indication from where to consider the S-wave velocity model from noise tomography valid (approximately 2 km depth, considering a group velocity of 2.3 km s $^{-1}$, see Appendix A). On the other hand, the longest period used in the inversion, 15.15 s together with the resolution tests using checkerboards (see Fig. 2.18) allow to take 20 km depth as the lower limit of validity for such anomalies for the velocity model derived from the noise tomography.

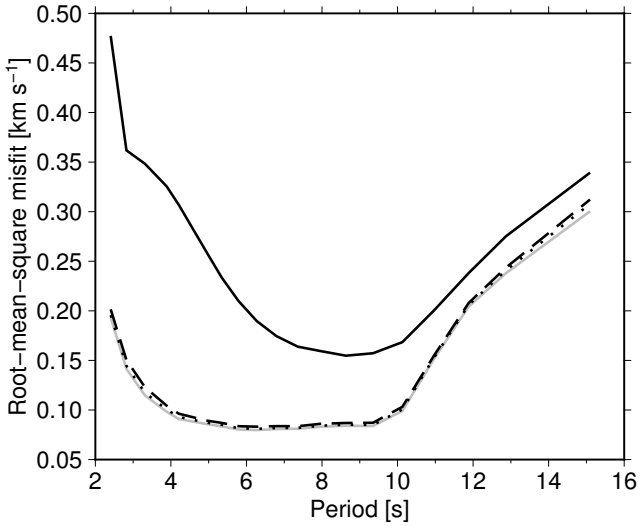

Figure 2.19: RMS misfit of group velocities for each damping factor (DF). Black solid line: RMS misfit for the reference velocity model CRUST1.0. Grey line: RMS misfit for the inverted velocity model with DF=0.5. Dotted line: RMS misfit for the inverted velocity model with DF=1. Dashed line: RMS misfit for the inverted velocity model with DF=2.

2.2.4 Velocity uncertainties

In the case of the noise tomography, the uncertainties in the observed data (i.e. dispersion data) are difficult to determine. However, it is possible to statistically estimate S-wave velocity uncertainties using pre-defined observational uncertainties and applying the Monte Carlo method (Korenaga et al., 2000). It is thus assumed that group-wave traveltime uncertainties have the same probability, are random and smaller than half a period. Taking the random data uncertainties as synthetic observations, it is possible to invert for a model of 3D S-wave velocity uncertainties using the following linearised equation (once again, kindly provided by Dr. M. Feng):

$$\mathbf{G}\boldsymbol{\Delta} = \boldsymbol{\delta} \tag{2.32}$$

where $\mathbf{G}$ is the sensitivity matrix, $\boldsymbol{\Delta}$ is the model uncertainty vector and $\boldsymbol{\delta}$ is the data uncertainty vector. The velocity model under these assumptions does not include true S-wave velocities, but results purely from the supposed data uncertainties and therefore, it can be considered as a S-wave velocity uncertainty model. Using 100 groups of random data uncertainties, 100 velocity uncertainty models were obtained. For each spatial position, the average S-wave velocity uncertainty over the 100 models is close to 0 km s^{-1}, and the maximum standard deviation throughout the whole 3D S-wave velocity model is 0.033 km s^{-1}, which can be considered as the general uncertainty in the inverted S-wave velocities.

2.3 Final S-wave velocity model

The tomography using the high-resolution TIPTEQ active source data can resolve well the upper few kilometres beneath the profile (see Sections 2.1.3 and 2.1.4). It can also resolve much smaller structures and thus, these results are preferred over the results from the noise tomography down to 2 km depth. On

the other hand, the S-wave velocity model from noise tomography has a good resolution down to 20 km depth. From noise tomography, two velocity models were obtained. A brief comparison of both velocity models is shown below. As mentioned before, the velocity model from the one-step dispersion inversion was chosen to be used in the final S-wave velocity model between 2 and 20 km depth.

2.3.1 Traveltime comparison for rays propagating through S-wave velocity models from dispersion data

Aside from a direct comparison of velocity values for both S-wave velocity models from noise tomography, one can compare traveltimes for rays that propagate through both models. For this purpose, both velocity models are merged with the 2D S-wave velocity model from Haberland et al. (2009), so that the former is used from 0 to 20 km depth and the latter from 20 to 75 km depth (see Section 2.3.2 for further detail about the merging procedure). Three synthetic sources were placed in each merged velocity model (see

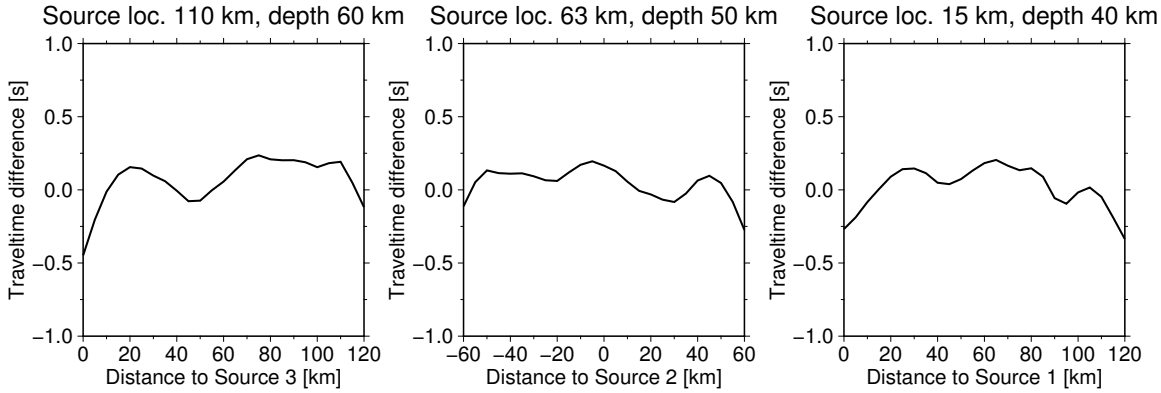

Figure 2.20: Traveltime comparison for rays propagating through each velocity model from noise tomography, using synthetic sources (see their location in Fig. 2.21). Comparison done through subtraction of traveltimes for the velocity model from the two-step inversion minus those for the velocity model from the one-step inversion.

their location in Fig. 2.21) and traveltimes from the sources to a line of recorders at the top surface of the model were calculated as in Section 2.1.1. Fig. 2.20 shows the comparison of the traveltimes for the three synthetic sources, as well as direct grid-point comparison of velocity values between the two models. It can be observed that for the three sources, the traveltime differences oscillate between -0.45 and 0.21 s (which represents a maximum percentage of $\sim$2.88% of the traveltimes with such difference peaks), showing the largest differences in the easternmost part of the profile. Excluding these peaks, the differences oscillate between $\pm$0.2 s. Points along the profile with positive traveltime differences show that the S-wave velocity from the one-step inversion is faster there. Negative traveltime differences mean that the S-wave velocity model from the two-step inversion is faster.

2.3.2 Velocity model from local-earthquake tomography and merging of S-wave velocity models

For the lower part of the final 2D S-wave velocity model (>20 km depth), the model obtained by Haberland et al. (2009) was used. They picked P-wave and S-wave traveltimes from local earthquake data and P-wave

traveltimes from the active source data recorded by the TIPTEQ Seismology array to obtain a 2D P-wave velocity model and a 2D v_p/v_s ratio model. These two models were used to make a grid point division of the P-wave velocity values by the v_p/v_s ratio values to obtain a S-wave velocity model. Maximum uncertainties are 0.15 km s^{-1} and 0.04 in the P-wave velocity model and in the v_p/v_s ratio model respectively (Haberland et al., 2009). Thus, the uncertainties in the S-wave velocity model from local earthquake tomography can be determined to be smaller than 0.15 km s^{-1} (Topping, 1972).

Since the velocity model uses local earthquake data it defines very well the area where the Nazca and South American plates interact. Thus, the final 2D S-wave velocity model will consist of three different velocity models merged together, each having a better resolution in a certain depth range.

For the final 2D S-wave velocity model, the three S-wave velocity models are merged such that from 0 to 2 km depth the results of the traveltime tomography from the active source data are used, from 2 to 20 km depth the 2D slice along 38.25°S from the 3D shear wave model from the dispersion analysis is used, and from 20 km to a maximum of 75 km depth, depending on the longitude, the S-wave velocity model from local earthquake tomography is used. In general, the models merged well with each other at the boundaries between the individual models at 2 and 20 km depth. However, to get rid of larger velocity contrasts at

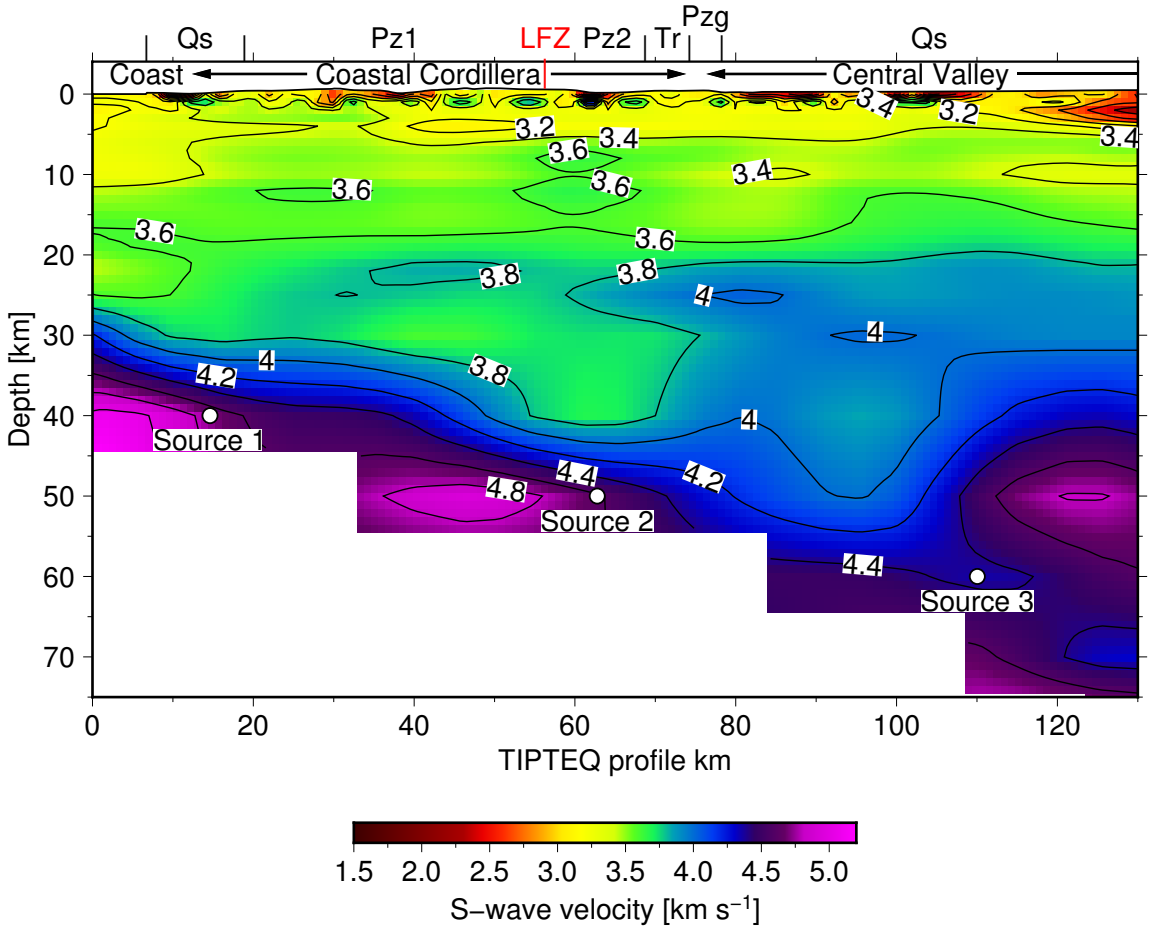

Figure 2.21: Final S-wave velocity model along 38.25°S, obtained by merging three different S-wave velocity models. The location of the LFZ and the geological units are as in Fig. 2.7. White dots: synthetic sources used for the calculation of traveltimes. No vertical exaggeration.

the boundaries where these do exist (e.g. at the centre of the profile, between the S-wave velocity model from noise-tomography and the model from local earthquake tomography, where the latter shows higher velocity values), the velocity values along the profile at 2, 19, 20 and 21 km depth were replaced by the simple average of the velocity at the respective depth and the velocities 1 km above and below (e.g. the new value at 2 km depth was obtained by taking the mean of the values at 1, 2 and 3 km depth). The final S-wave velocity model can be observed in Fig. 2.21. The model has been derived from seismic waves ranging in frequency from 0.06-10 Hz. However, the model from the noise tomography based on the lower frequency waves from 0.06-0.4 Hz does not stick out as either a prominent high or low velocity zone, with respect to either the models from the active source or local earthquake tomography which used waves with higher frequencies from about 1-10 Hz. Indeed, the fact that the different velocity models do seem to blend so well despite the relatively small amount of interpolation between them at around 2 and 20 km depths lends credence to the merging procedure.

2.3.3 Comparison between final merged S-wave velocity model and S-wave velocity model from local earthquake tomography

2.3.3.1 Grid-point comparison of S-wave velocity models

Fig. 2.22 shows the S-wave velocity difference between the velocity model from local earthquake tomography and the final 2D S-wave velocity model. Since from 20 km depth the final model uses the local earthquake tomography, only differences down to 25 km depth are shown. Velocity differences between 20 and 25

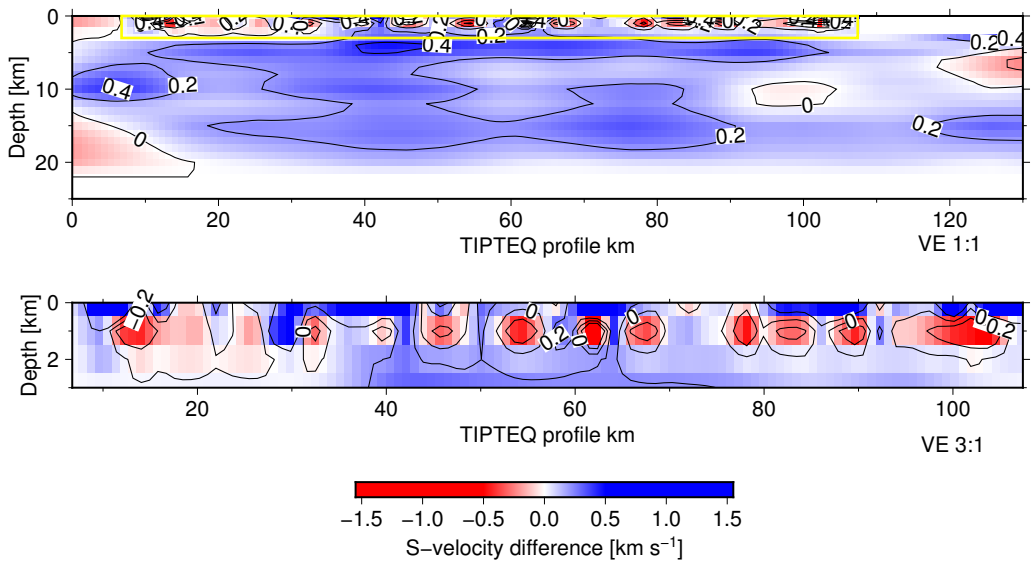

Figure 2.22: S-wave velocity differences (S-wave velocities from local earthquake tomography minus final S-wave velocities) along the TIPTEQ profile. There is no information in the local earthquake velocity model down to 1 km depth east of ∼107 km. The lower image shows a close-up of the area inside the yellow rectangle.

km depth are the product of the interpolation at 20 km depth in the final velocity model. Most of the region between 3 and 20 km depth shows positive differences that do not vary greatly in the model (usually less than 0.3 km s^{-1}). However, the largest velocity differences are observed in the first 2 km depth as

small clusters not only with positive differences, but also with some negative differences (see Fig. 2.22, close-up). These clusters show the largest velocity differences in terms of absolute value. This region is where the S-wave velocities from local earthquake tomography are compared to the velocities from the controlled source data. Thus, it can be expected to observe such velocity differences because in this region the well resolved, small-scale anomalies from the high-resolution active source data are incorporated in the final S-velocity model. A technical explanation for the velocity differences between the two models between 3 and 20 km depth (where the S-wave velocities from noise tomography are used in the final S-velocity model), could be the different damping factors used in the inverse part of the tomographic problem for the different models. Another explanation is related to the different sources used to obtain each velocity model. The noise tomography uses ambient seismic noise, mainly from the Pacific Ocean, recorded on the vertical component of the stations of the TIPTEQ array. Thus one would expect to obtain v_{SV} velocities from the surface wave (Rayleigh wave) inversion and not v_{SH} velocities. In the case of the local earthquake tomography, S-waves of both polarities could have been used for the tomographic inversion. This could imply, as already suggested in Section 2.1.2, the presence of anisotropy in the continental margin that might explain the S-wave velocity differences.

2.3.3.2 Traveltime comparison

Another way to compare the two S-wave velocity models is through the calculation of synthetic traveltimes for both models, as in Section 2.3.1. For this purpose, the same three synthetic sources are used (Fig. 2.21). Fig. 2.23 shows the differences between the traveltimes for rays propagating through the S-wave velocity model from local earthquake tomography and for rays propagating through the final merged velocity model. As expected, they are always positive. The rays associated with the smallest traveltime differences (between 0.13 and 0.2 s) are those that propagate through the red areas in Fig. 2.22, that compensate the generally positive velocity differences. On the other hand, the largest traveltime differences, between 0.5 and 0.7 s, are those for rays that avoid the negative velocity differences zones in Fig. 2.22 and go through the positive velocity differences in the first 2 km depth.

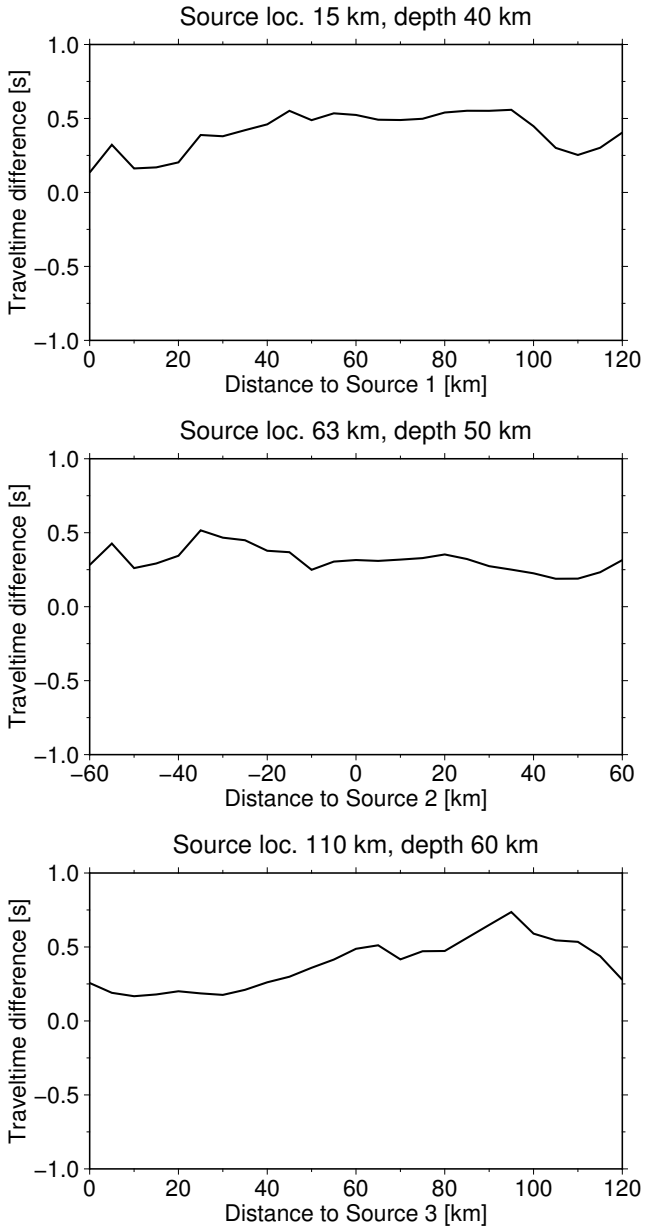

Figure 2.23: Traveltime comparison through the subtraction of synthetic S-wave traveltimes for the final 2D S-wave velocity model minus traveltimes through the velocity model from local earthquake tomography.

Chapter 3

Reflectivity images

The processing of the TIPTEQ NVR data using reflection seismics aims to produce P- and S-wave reflectivity images along the study profile. In the work of Micksch (2008), the raw TIPTEQ data were pre-processed (e.g. data format conversion, creation of a parameter and field geometry database, surgical and top mutes) as described in Section 2.1.2. Further processing led to stacked and depth migrated P-wave envelope reflectivity images.

In this work, the existing processing jobs in ProMAX for P-waves (i.e. on the vertical component) are revised to obtain phase stacked and depth migrated reflectivity images. Additionally, the horizontal components are processed to obtain S-wave reflectivity images.

3.1 Overview of the theory of reflection seismics processing

There are three primary stages in seismic data processing. Firstly, the deconvolution, removes the source time function – modified by various effects of the earth and recording system – from the recorded seismic traces, thereby increasing temporal resolution. After applying a normal moveout (NMO) correction to the traces of each common midpoint (CMP) gather, stacking sums them along the offset. Finally, the migration, which is commonly applied to stacked data, collapses diffractions and dipping events to their true subsurface locations (Yilmaz, 2001). All other processing techniques may be considered secondary in that they help improve the effectiveness of the primary stages. The secondary techniques used in this work to process P- and S-wave reflection data are listed and briefly described in Section 3.2.

3.1.1 Deconvolution

Although some tests were made using a deconvolution operator (see Sections 3.3.1 and 3.3.3), this was not part of the preferred processing jobs that produced the P- and S-wave reflectivity images (see Sections 3.2.1 and 3.2.2).

The recorded data may be considered as the convolution of the source signal with the instruments, the geophones and the response of the earth, which includes some undesirable effects, such as reverberation and attenuation. Ideally, each reflection would be a sharp pulse approximating a delta function, so the arrival time of the reflection and the depth of the reflector would be determined precisely (see Fig. 3.1).

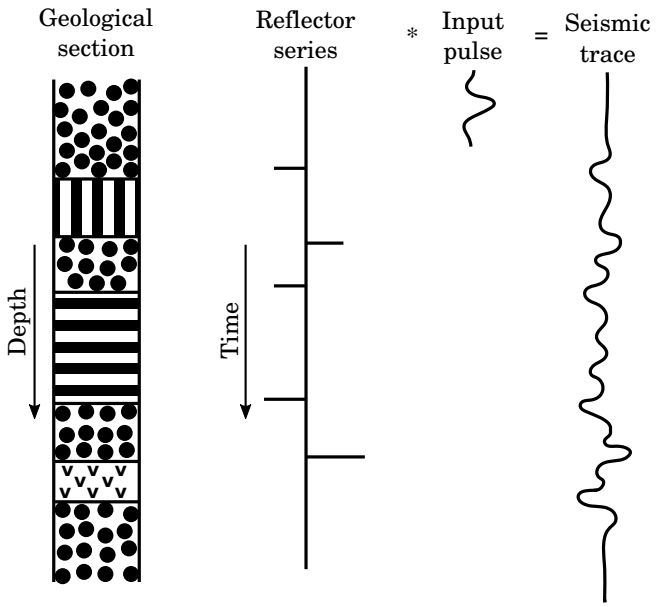

Figure 3.1: A reflection seismogram can be viewed as the convolution of a source wavelet with a reflection series, with impulses at times corresponding to the arrival times of reflections. Figure modified after Kearey et al. (2013).

Deconvolution, also known as inverse filtering, is the analytical process of removing the effect of some previous filtering operation or convolution (Kearey et al., 2013). In general, such convolutions lengthen the seismic pulse, degrading the temporal resolution. In addition, reflected waveforms from closely-spaced reflectors will overlap in time on the seismic trace and will interfere. In appearance, deconvolved seismic sections are crisper and more detailed as opposed to blurrier, ringy convolved images (Yilmaz, 2001).

For a seismogram $s(t)$, resulting from a source pulse or wavelet $w(t)$ and $r(t)$, which describes the effect of the structure – a reflector series in this case – and neglecting the effects of attenuation and absorption

$$s(t) = w(t) * r(t) \tag{3.1}$$

Deconvolution has the general aim, not fully realizable, of compressing every occurrence of a waveform $w(t)$ on a seismic trace into a spike output, in order to reproduce the reflectivity function $r(t)$. The required deconvolution operator is an inverse filter $i(t)$, such that

$$i(t) * s(t) = r(t) \tag{3.2}$$

Practically achievable inverse filters are always approximations to the ideal filter that would produce a reflectivity function from a seismic trace. Deconvolution may be carried out on individual seismic traces before stacking or on CDP stacked traces, and is commonly employed at both these stages of data processing (Kearey et al., 2013).

3.1.2 Common depth point sorting and normal moveout correction

Seismic data acquisition with multifold coverage is done in shot-receiver coordinates. On the other hand, seismic data processing conventionally is done in CMP-offset coordinates by sorting the data into CMP gathers based on the coordinate transformation

$$\begin{aligned} m &= (x_s + x_r)/2 \\ h &= (x_s - x_r)/2 \end{aligned} \tag{3.3}$$

where m is the average position of the source and receiver, and h is the half-offset, which measures the source and receiver distance away from the midpoint.

This sorting requires field geometry information. Each trace is assigned to the midpoint between the source and receiver locations associated with that trace. The traces with the same CMP are grouped together, making up a CMP gather. A common depth point (CDP) gather – which is often used instead of CMP (Yilmaz, 2001) – is equivalent to a CMP gather only when reflectors are horizontal and velocities do not vary horizontally (see Fig. 3.2). Under these assumptions, the CDP term is used throughout this work.

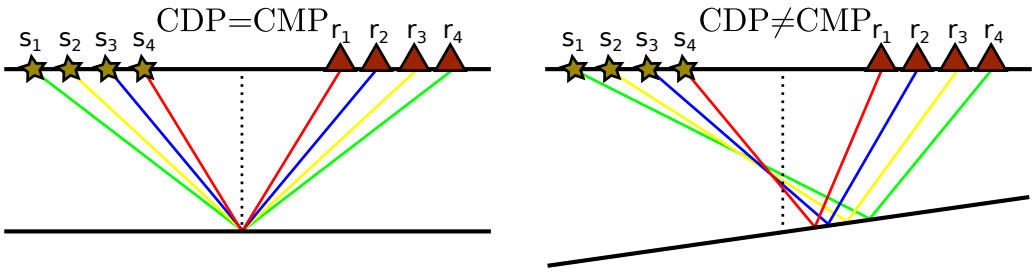

Figure 3.2: Geometry of CDP and CMP gathers for horizontal (left) and dipping reflectors (right).

The properties of the CDP-offset coordinate system are that (1) the traveltimes curves are symmetric in offset about $h = 0$; (2) for a horizontal reflector lying at a depth z beneath a homogeneous top layer of velocity v, the traveltime curve is a hyperbola expressed in offset and the two-way zero-offset traveltime $t_0 = 2z/v$; and (3) many types of multiple reflections are strongly attenuated relative to primary reflections (Levander et al., 2007).

The most convenient form of the traveltime-distance equation for reflected rays, which is used extensively in the processing and interpretation of reflection data, is (Kearey et al., 2013)

$$t \approx t_0 + \frac{x^2}{2v^2 t_0} \tag{3.4}$$

Moveout is defined as the difference between the traveltimes t_1 and t_2 of reflected-ray arrivals recorded at two offset distances x_1 and x_2. Substituting these terms in Equation 3.4, and subtracting the resulting equations gives

$$t_2 - t_1 \approx \frac{x_2^2 - x_1^2}{2v^2 t_0} \tag{3.5}$$

A normal moveout at an offset distance x is the difference in traveltime ΔT_{NMO} between reflected arrivals

at x and at zero offset

$$\Delta T_{NMO} = \frac{x^2}{2v^2 t_0} \tag{3.6}$$

For a horizontally stratified earth, the traveltime curves are still essentially hyperbolic. This is valid at offset distances that are small compared to reflector depths (Yilmaz, 2001; Kearey et al., 2013). In this case however, the top-layer velocity v in Equations 3.4 and 3.6 is replaced by the RMS velocity $\tilde{v}$ of the layers overlying the reflector (Kearey et al., 2013)

$$\tilde{v} = \sqrt{\frac{\sum_i v_i^2 \tau_i}{\sum_i \tau_i}} \tag{3.7}$$

where v_i is the interval velocity of the ith layer and τ_i is the one-way traveltime of the reflected ray through the ith layer. The RMS velocity is interpreted as the velocity that gives the set of straight ray, approximate, traveltimes closest to the actual curved raypath traveltimes for a given depth (Levander et al., 2007).

For dipping reflectors, the traveltime equation still has the form of a hyperbola, with the dip of the reflector as an additional unknown. In this case the axis of symmetry of the hyperbola is no longer the time axis. A dip moveout (DMO) correction is defined as the difference in traveltimes t_x and t_{-x} of rays reflected from the dipping interface to receivers at equal and opposite offsets x and $-x$ (Kearey et al., 2013).

3.1.3 Stacking

Ideally, traces on a certain CDP gather sample the same subsurface point with different offsets. The data, as a function of offset and time, contain primary reflections from interfaces that are used to determine velocity structures with depth. They also contain arrivals of lesser interest (e.g. direct waves, head waves, air waves, groundroll, multiples). To enhance primary reflections and suppress everything else, the fact is exploited that, unlike the arrivals of lesser interest, primary reflections have hyperbolic traveltimes curves. If each trace is shifted in time by the appropriate NMO, a reflection appears at the same time for all the offsets. The sum of the traces after the NMO, in theory, is the single trace that would have been recorded at zero offset, with coincident source and receiver (Stein and Wysession, 2009). The reflections, in phase on all traces, sum constructively and give a strong arrival. By contrast, incoherent noise and other arrivals sum destructively, yielding weaker arrivals and increasing the signal-to-noise ratio. For the TIPTEQ NVR data, an 8-fold CDP stack results in $\sim$3 times improvement in data quality (Micksch, 2008).

3.1.4 Depth migration

Migration moves dipping reflectors into their true subsurface position and collapses diffractions, delineating detailed subsurface features, such as fault planes. For this purpose, the conversion requires as accurate a velocity model as possible. This process can be understood as a spatial deconvolution, since it increases spatial resolution (Yilmaz, 2001). The goal of the depth migration is to make the stacked section appear similar to the geologic cross section along the seismic line. When a stacked section is migrated, migration theory is applicable to data recorded with a coincident source and receiver (zero-offset). From a geometric point of view, migration steepens reflectors and shortens and moves them in the updip direction (Yilmaz,

2001).

The TIPTEQ NVR reflectivity data were depth migrated using two migration methods: Kirchhoff post-stack depth migration and pre-stack migration. In particular, it was of interest to study the possibility that the pre-stack migration approach of Bauer et al. (2013) could better image steep reflectors along the TIPTEQ profile, compared to the Kirchhoff post-stack migration. Steep reflectors in the TIPTEQ seismic images include those such as the west-dipping reflector in the eastern part of the profile (Groß et al., 2008; Micksch, 2008) and the reflector related to the LFZ, especially closer to the surface.

3.1.4.1 Kirchhoff depth migration

Also known as diffraction sum migration, Kirchhoff depth migration consists of searching the input data in (x, t) space for energy that would have resulted if a diffraction source (Huygens' secondary source) were located at a particular point in the output (x, z) space (Yilmaz, 2001). The approach assumes that any continuous reflector is composed of a series of closely-spaced point reflectors, each of which is a source of diffractions, and that the continuity of any reflection event results from the constructive or destructive interference of these individual diffraction events (Kearey et al., 2013). This search of the input data is carried-out by summing the amplitudes in (x, t) space along the diffraction curve that corresponds to Huygens's secondary source at each point in the (x, z) space. The result of this summation is then mapped onto the corresponding point in the (x, z) space.

Diffraction summation is a straightforward summation of amplitudes along the hyperbolic trajectory whose curvature is governed by the velocity function. Assuming a horizontally layered velocity model, the equation for the hyperbolic traveltime trajectory is (Yilmaz, 2001)

$$t^2(x) = t^2(0) + 4\frac{x^2}{\tilde{v}^2} \tag{3.8}$$

The velocity function used to compute the traveltime trajectory is the RMS velocity at the apex of the hyperbola at time $t(0)$.

3.1.4.2 Pre-stack migration

Bauer et al. (2013) developed a modified Fresnel volume migration (FVM) technique. Their method can be considered as an infinite frequency approximation of the FVM. This method provides depth sections by migrating line segments (which represent reflective structures derived directly from the data) instead of waveforms, losing wavefield information, but using less computation time, which is useful for testing optimal data processing parameters, evaluating migration velocity models and designing pre- and post-migration filters. The reader is referred to Bauer et al. (2013) for further details about this pre-stack migration method.

3.1.5 Resolution of seismic data

Resolution relates to how close two points can be, yet still be distinguished as two unique events (Yilmaz, 2001). Two types of resolution are considered: vertical and lateral. Both are controlled by spectral

bandwidth, therefore also on the used source and energy. For the TIPTEQ data (in particular for P-wave seismic processing), Micksch (2008) used the interactive spectral analysis tool to examine the frequencies contained at different times and offsets. This procedure was repeated in this work for the S-wave seismic processing (see Section 3.2.2). In general, the frequency ranges given by the bandpass filters applied in the data processing are enough for resolution calculations.

3.1.5.1 Vertical resolution

Neglecting the effects of noisy recording, the vertical resolution can be calculated as a quarter of the main wavelength λ (Yilmaz, 2001), where

$$\lambda = \frac{v}{f} \tag{3.9}$$

From the spectral analyses done by Micksch (2008) and also in this work (on both the vertical and horizontal components), the range of frequencies (f) to estimate the resolution was set to be 10 - 20 Hz for the P-wave seismic data and 5 - 15 Hz for the S-wave data. The seismic velocities (v) were taken from the SPOC P-wave velocity model to range between 5.8 and 7.2 km s^{-1} close to the plate interface (Krawczyk et al., 2006). For the S-wave seismic data the velocities to estimate the resolution were taken from the synthetic velocity model used to stack the S-wave seismic data (see Section 3.2.2) and ranged between 3.5 and 4.3 km s^{-1}.

Thus the vertical resolution for the P-wave seismic data is estimated to range between 72.5 and 180 m. This is more conservative than the estimations done by Micksch (2008). For the S-wave seismic data, the vertical resolution was estimated to range between 58.3 and 215 m.

3.1.5.2 Lateral resolution

Before calculating the lateral resolution, it is useful to introduce the concept of the Fresnel zone. A seismic wavefront is not reflected instantaneously from one single point, but instead from an area over a short time interval. Thus, signals that arrive at the receiver in that time frame cannot be distinguished from each other and they interfere. The area where reflections originate, such that for a given frequency the energy arriving at the receiver inside the time window resembling half of the wavelength (or $\lambda/4$ for one-way-traveltime) interferes constructively, is called the Fresnel zone (Yilmaz, 2001). Since the Fresnel zone depends on wavelength, it also depends on frequency. It increases with increasing depth and wavelength.

The radius of the Fresnel zone (r_f) is (Yilmaz, 2001)

$$r_f \approx \sqrt{\frac{1}{2}\frac{zv}{f}} \tag{3.10}$$

Equation 3.10 shows that the lateral resolution depends, aside from the velocity and frequency, on the depth. The resolution is then estimated in the depth range from 13 km (depth of the top reflectivity band in the west) to 60 km depth (depth of the bottom reflectivity band in the east (Micksch, 2008; Groß et al., 2008)). With these considerations, the lateral resolution of the P-wave TIPTEQ data is calculated to range approximately between 1.37 (at 13 km depth) and 4.65 km (at 60 km depth). Similarly for the S-wave

TIPTEQ data, the lateral resolution – or the Fresnel radius – is calculated to range approximately between 1.23 km (at 13 km depth) and 5.1 km (at 60 km depth).

3.2 Data processing

The processing sequences prepare the TIPTEQ near-vertical reflection (NVR) data for the main steps in reflection seismics: stack and depth migration. The software ProMAX was used for the post-stack depth migration. The pre-stack depth migration was carried-out with the software developed by Bauer et al. (2013).

3.2.1 P-wave reflectivity data processing

The processing flows in ProMAX that produced the P-wave reflectivity images obtained by Micksch (2008) were revised to obtain P-wave phase stack and migration images, instead of the previously obtained envelope reflectivity images.

3.2.1.1 Processing sequence for post-stack depth migration

The Z-component processing, carried-out in ProMAX, applied different trace mutes, static corrections, a bandpass filter and amplitude corrections (such as true amplitude recovery and automatic gain control) to remove effects such as attenuation and geometrical spreading. Afterwards, a normal moveout correction (NMO) was applied, followed by the stack and depth migration of the processed data. The P-wave velocity model used for the NMO and depth migration was the SPOC P-wave velocity model (Krawczyk et al., 2006). The preferred Z-component processing sequence using ProMAX was:

- **Disk Data Input:** pre-processed vertical component NVR data sorted by the field file identification number (FFID) are loaded.
- **Trace Length:** shortens trace length to the first 50 s.
- **Trace dc Removal:** the mean of each input trace is removed.
- **Trace Kill/Reverse:** useless traces are removed from the processing.
- **Trace Muting:** mutes the airblast and car noise on the input data.
- **Hand Statics:** specifies and applies hand input static corrections. Accounts for time shift errors produced by malfunctioning GPS cards.
- **Header Statics:** bulk static shift to remove the first 2 s.
- **Trace Muting:** top mute to remove direct and refracted arrivals.
- **Database/Header Transfer:** transfers values between the database and trace headers.
- **Header Statics:** applies static corrections to move the traces to a floating datum.

- **Bandpass Filter:** Ormsby filter: 6 - 10 - 35 - 50 Hz (0% - 100% - 100% -0%, with cosine tapers between 0 and 100%).
- **Trace muting:** mutes the groundroll (surface waves).
- **True Amplitude Recovery (TAR):** compensates for loss of amplitude in the traces due to wavefront spreading and inelastic attenuation. The module treats geometrical spreading as a function of traveltime and velocity $(1/(t \cdot v)^2)$. Two offset-dependent velocity-time function were used, changing them at an absolute offset of 1500 m.
- **Automatic Gain Control (AGC):** automatically varies the gain applied to trace samples as a function of sample amplitude within an AGC time window. The AGC scalar is based on the RMS of the sample amplitudes and the window length is 4 s.
- **Trace Equalization:** computes and applies a trace-to-trace amplitude balance function.
- **Infill Data:** uses a limited aperture Tau-P forward and inverse transform to fill-in missing data.
- **2nd Trace Equalization.**
- **Blend:** takes output from another processing tool (in this case, the following Dip Scan Stack process) and combines it with the input data at a specified ratio. Ratio of processed/original 3:5. It reduces the effect of the following Dip Scan Stack process.
- **Dip Scan Stack:** uses a limited aperture Tau-P transform to enhance coherent seismic events.
- **3rd Trace Equalization.**
- **Disk Data Output and Input:** processed data are exported, then imported and sorted to CDP gathers.
- **Trace Length:** data are shortened to the first 35 s.
- **Normal Moveout (NMO) Correction:** as in Micksch (2008), the P-wave velocity model used for the NMO and depth migration was the SPOC model (Krawczyk and the SPOC Team, 2003). See Section 3.1.2 for further details.
- **CDP/Ensemble Stack:** see Section 3.1.3 for details.
- **Header Statics:** after the stack, the CDP static corrections are removed to take the reflections to their real arrival time (depth).
- **Blend:** ratio of processed/original 1:1.
- **Dip Scan Stack:** an enhancement of coherent seismic events after stacking improved greatly the seismic image.
- **Pad Traces:** at the beginning and at the end of the stack image, additional CDP traces were added. Originally the CDPs ranged from 1775 to 3906. After padding traces, they ranged from 1 to 5600.

- **Kirchhoff Depth Migration:** see Section 3.1.4 for details.

3.2.1.2 Processing sequence for pre-stack depth migration

The Z-component processing was initially carried-out in ProMAX, to then apply the pre-stack line-drawing migration (Bauer et al., 2013). Firstly, P-wave first arrivals were picked, excluding the channels without data. Such traveltime picks were used as a top-mute to lose as few reflection data as possible, especially when reflections are close to the first arrivals. This P-wave picking was quick, with non-tomographic purposes and was carried out without a linear moveout correction.

Afterwards, the Z-component data were processed following steps similar to those that produced the post-stack image. In this case, the missing data were not in-filled but simply ignored. Also, no Tau-P transform to enhance coherent events was used.

Tests were carried out modifying the window length of the Automatic Gain Control (AGC, e.g. 1 s and 2 s length instead of 4 s) and the corner frequencies of the bandpass filter. The length of the AGC did not seem to matter, in terms of introducing relevant new information. A filter using lower frequencies helps to depict the plate interface better, however the difference is minimal.

The processing to produce the image shown in this work (Section 3.3.2) included the same bandpass filter used for the post-stack migration (6 - 10 - 35 - 50 Hz), and the true amplitude recovery, automatic gain control and groundroll muting were the same as previously described.

Next, the steps described in Bauer et al. (2013) are followed. A semblance analysis is performed on the shot-gathered data to detect coherent events and determine the local slowness of the wavefield. Afterwards, ray-tracing is performed from the receiver back to the subsurface, for each selected line-drawing segment to find the isochrone (the trajectory of potential reflection points) using the emergent angle based on the previously found local slowness and a velocity model, which in this case was the 2D velocity model of Haberland et al. (2009). This provides the image point for the migrated line-drawing segment. In this step the reflector dip is also calculated.

3.2.2 S-wave reflectivity data processing

S-wave reflectivity data (the horizontal NS and EW components) were processed for post-stack depth migration in ProMAX. The processing flow that produced the P-wave reflectivity images was used as a reference for the S-wave processing. The preferred processing sequence used in ProMAX to produce the S-reflectivity images was:

- **Disk Data Input:** pre-processed NVR-data of the horizontal components (NS or EW) sorted by the FFID are loaded, to be processed separately.
- **Trace Length:** shortens trace length to the first 50 s.
- **Trace dc Removal:** the mean of each input trace is removed.
- **Trace Kill/Reverse:** useless traces (bad traces, dead channels) are removed.
- **Trace Muting:** mutes the airblast and car noise on input data.

- **Hand Statics:** accounts for GPS time shift errors.
- **Header Statics:** removes the first 2 s.
- **Trace Muting:** top mute to remove direct and refracted S-wave arrivals.
- **Database/Header Transfer:** transfers values between the database and trace headers.
- **Header Statics:** applies static corrections to move the traces to a floating datum.
- **Trace Kill/Reverse:** reverses the polarity of traces with negative offset.
- **Bandpass Filter:** Ormsby filter: 4 - 8 - 20 - 40 Hz (0% - 100% - 100% - 0%, with cosine tapers between 0 and 100%).
- **Trace Muting:** mutes the groundroll (surface waves).
- **True Amplitude Recovery (TAR):** the velocity-time functions depended on the absolute offset of the traces. The functions were changed at an offset of 1500 m. See Section 3.2.1.1 for details.
- **Automatic Gain Control (AGC):** window length: 7 s. See Section 3.2.1.1 for details.
- **Trace Equalization:** trace-to-trace amplitude balance function.
- **Infill Data:** uses a limited aperture Tau-P forward and inverse transform to fill-in missing data.
- **2^{nd} Trace Equalization.**
- **F-X Decon:** applies a complex Wiener unit prediction filter in distance for each frequency in a specified range, and then inverse transforms each resulting frequency trace back to the time domain. It produces output with less random noise than the input data.
- **Blend:** ratio of processed (in this case, the following Dip Scan Stack process) /original 3:5.
- **Dip Scan Stack:** uses a limited aperture Tau-P transform to enhance coherent seismic events.
- **Disk Data Output and Input:** processed data are exported, then imported and sorted to CDP gathers.
- **Normal Moveout Correction:** for the S-wave seismic processing, a synthetic velocity model was used for the NMO and depth migration. See Section 3.3.3 and Appendix B.1 for further details. See Section 3.1.2 for details about the NMO.
- **CDP/Ensemble Stack:** see Section 3.1.3 for details.
- **Header Statics:** after the stack, the CDP static corrections are removed to take the reflections to their real time/depth.
- **Bandpass Filter:** a post-stack time and space-variant Ormsby filter was applied. Details about the filter are given in Appendix B.2.

- **Pad Traces:** as for P-wave seismic processing, after padding the CDPs ranged from 1 to 5600.
- **Kirchhoff Depth Migration:** see Section 3.1.4 for details.

The first change in the processing for reflected S-waves with respect to the flow that produces the P-reflectivity images corresponds to static corrections. Knowing the elevation along the profile and assuming a certain velocity value (for P-wave seismic processing it was a constant value of 5500 m s^{-1}), the static corrections move the locations of sources and receivers to a fixed datum to compensate for velocity variations due to the topography. Initially, those same times, multiplied by $\sqrt{3}$ were used for the S-wave processing, but such times obtained from a constant velocity might not represent the best static correction for S-waves (e.g. for unconsolidated sediments, such as those in the first km depth, where S-velocities are close to zero). To compare the correction differences induced by the use of a constant velocity, a new set of static corrections was created using the topography and the S-wave velocity model from the TIPTEQ seismic data obtained in Section 2.1 (Dohr, 1985b). The comparison between both sets of static corrections for sources and receivers can be observed in Fig. 3.3. The static corrections were originally calculated for the 104

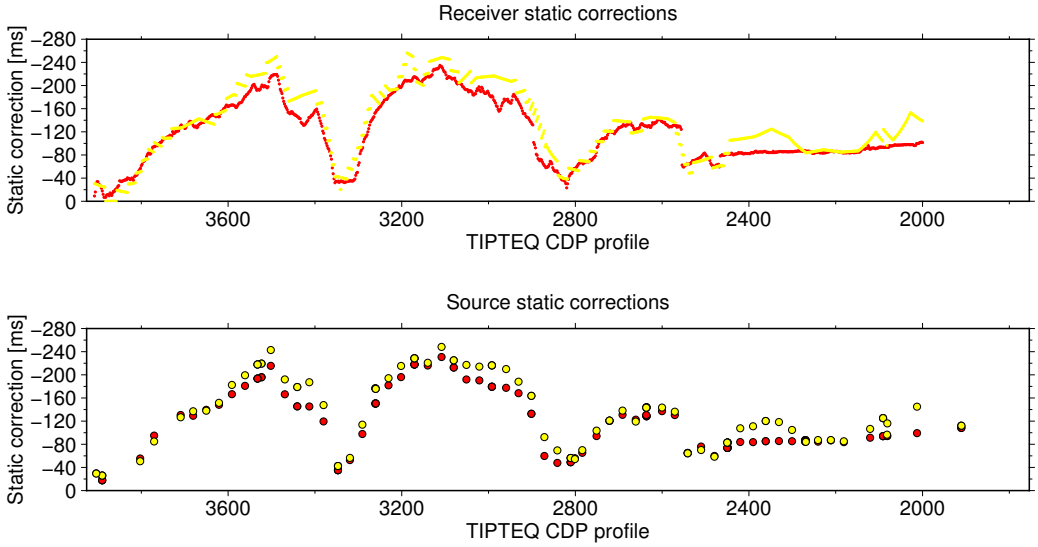

Figure 3.3: Comparison between static corrections using a constant velocity value to calculate the times (red dots) and using the S-wave velocity model obtained in Section 2.1 (yellow dots).

sources (not only for NVR shots) and this was also done for this set of corrections. Although for some parts of the profile the static corrections are similar, some of them are underestimated, e.g. near CDP 2400 and CDP 2000, which correspond to low S-wave velocity structures in the S-wave velocity model (see Fig. 2.7). Mean differences of $\sim$ 17 ms were found between both sets of static corrections. The obtained set of static corrections was imported into ProMAX and used for the S-wave seismic processing.

The applied bandpass filter of 4 - 8 - 20 - 40 Hz was chosen following similar criteria as Micksch (2008). Removing frequencies under 8 Hz removed most of the groundroll. The remaining surface-wave data were removed using a surgical mute. 8 Hz was chosen instead of the 10 Hz used by Micksch (2008) because inspection of the data showed that S-wave reflectivity signals are present at lower frequencies. The filter was also more restrictive with higher frequencies, since the observed S-wave reflectivity was in general of poorer

quality than the P-wave reflectivity and higher frequencies added unwanted noise. Additionally, a post-stack time and space variant Ormsby filter was applied, removing low-frequency noise in the first seconds and improving the signal-to-noise ratio in general. Further details about the time and space variant filter are given in Appendix B.2.

In the P-wave seismic processing flow (see Section 3.2.1.1), a Dip Scan Stack was applied before and after stacking. This limited-aperture Tau-P transform enhanced coherent seismic events, thus enhancing the resulting images, but this was not the case for the S-wave seismic processing. In this case, the tool also acted on random noise, not contributing to improve the contrast between real seismic reflections and noise. For this reason, the F-X Decon tool was used to reduce random noise before applying the Dip Scan Stack tool. Unlike in the previous processing flow, this tool was not applied after stacking.

The S-wave velocity model used for stacking and migration was a synthetic model. The rational for this is that, on the one hand, it is desirable to use a velocity model that was obtained from the same data as were used for the seismic processing. On the other hand, S-waves are more sensitive to velocity variations than P-waves and thus, synthetic velocities that better stack the seismic data can be used and then compared to those obtained from seismic tomography (R. Ghose, private communication). Further details about the synthetic velocity model are given in Appendix B.1.

3.3 Stacked and migrated images

This section shows the obtained P- and S-wave reflectivity images along the TIPTEQ CDP profile. The integrative interpretation of the images, along with other results or studies is made in Chapter 5.

3.3.1 P-wave post-stack images

3.3.1.1 CDP stacked time section

Fig. 3.4 shows the CDP phase-stack section.

Features similar to those in the P-wave envelope stack obtained by Micksch (2008) are observed, with coherent, horizontal and east- and west-dipping reflections that are structurally continuous for tens of kilometres. In particular, three prominent east-dipping bands of reflectivity are observed beneath the western portion of the profile, with the lowermost band at such depths that it corresponds to the plate interface. East of the LFZ these three bands are joined by an uppermost fourth band under the eastern part of the profile. No reflector related to the continental Moho was found, but the west-dipping steep reflector at the eastern part of the profile, between 19 s and 27 s, which apparently crosses through the plate interface (Groß et al., 2008; Micksch, 2008) can be clearly observed. The stacked image has a higher noise level around 60 km at all times, thus making the identification of the different reflectivity bands here more difficult than in the rest of the profile.

The preferred processing sequence for P-wave reflectivity did not include a deconvolution. However, this option was tested in a set of tests (before the bandpass filter in the processing flow). The overall quality of the time-stacked section when comparing to Fig. 3.4 was deteriorated when applying a deconvolution operator (e.g. the plate interface was less evident), probably due to the effect of non-optimal deconvolution

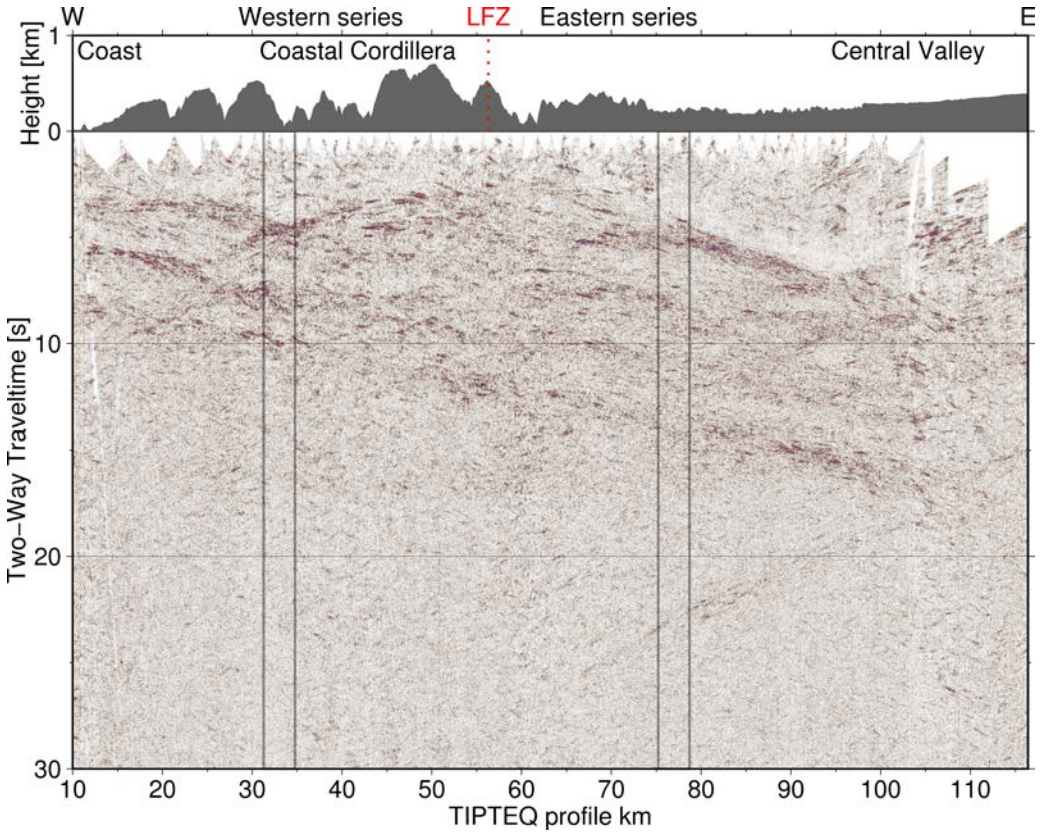

Figure 3.4: P-wave phase stack reflectivity image along the TIPTEQ profile, obtained from the preferred processing sequence (Section 3.2.1). In Chapter 4 synthetic seismograms using the reflectivity method were calculated for the two portions inside the rectangles. LFZ: Lanalhue Fault Zone.

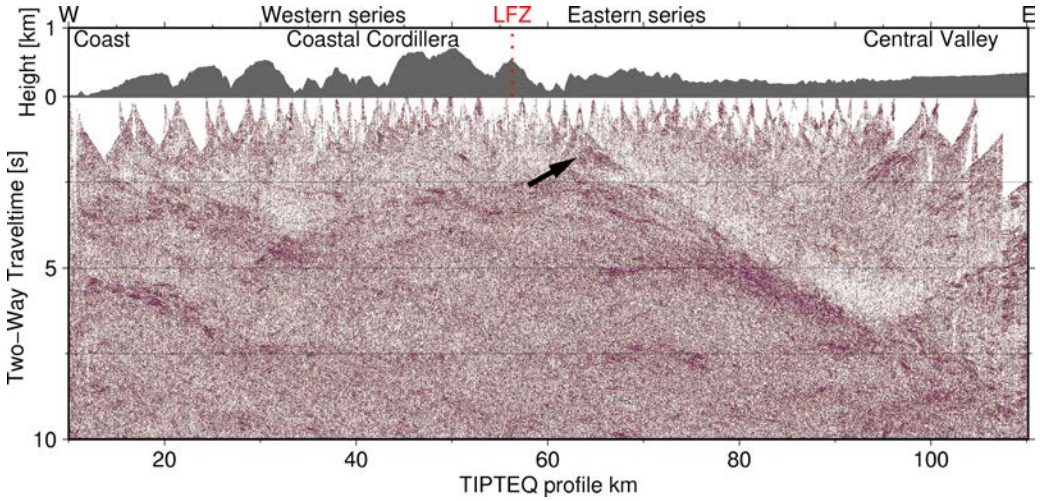

Figure 3.5: First 10 s of the P-wave phase stack with deconvolution. The black arrow points to what could be the LFZ in the first seconds. LFZ: Lanalhue Fault Zone.

gates. However, an event visible in the first 3 seconds near 60 km (see black arrow in Fig. 3.5) could be an indication of the geometry of the Lanalhue fault zone (LFZ) at shallower depths, which had not been

imaged previously (Groß et al., 2008; Micksch, 2008) and was not identified without the deconvolution (see Fig. 3.4). The use of different deconvolution gates could be tested in greater detail in the future to study if they improve the quality of deeper reflectors.

3.3.1.2 Post-stack depth migrated image

The post-stack depth migrated image for P-wave reflectivity can be observed in Fig. 3.6. In general, similar

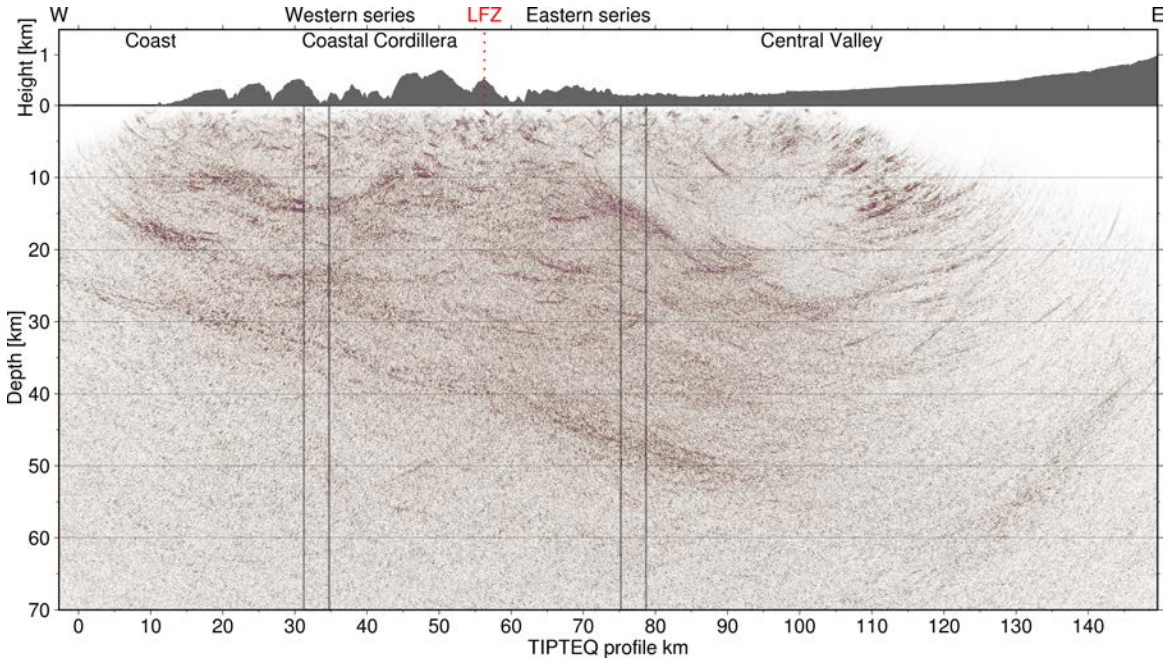

Figure 3.6: Post-stack depth migrated P-wave reflectivity image. Vertical exaggeration ≈ 1. In Chapter 4 synthetic seismograms using the reflectivity method were calculated for the two portions inside the rectangles. LFZ: Lanalhue Fault Zone.

characteristics as in the P-stack image are observed, with several bent, dipping and horizontal reflectors. The strength of the reflections varies along the different reflectors (e.g. along the plate interface). Further, whereas the three prominent east-dipping bands of reflectivity beneath the western portion of the profile maintain their separate character beneath this part of the profile, the middle two of the four reflectivity bands below the eastern part of the profile seem to lose clarity as separate bands the further east one goes. The steep west-dipping reflector is migrated to a position that is almost perpendicular to the east-dipping plate interface, crossing it beyond the eastern end of the profile (which consisted of zero-padded traces). The image does not give information about this reflector at shallower depths. Typical smiles can be seen at both ends of the image due to a coarser CDP fold. No coherent reflectivity events are observed above $\sim$7 km depth. Micksch (2008) emphasizes that the recordable dip of a certain reflective feature at a certain position depends on the geometry and the length of the spread, a point to keep in mind when interpreting and discussing e.g. steep reflections at both ends of the profile.

Fig. 3.7 shows the post-stack depth migrated reflectivity image using a deconvolution operator. Less noise in the first kilometres depth than in Fig. 3.6 seems to allow to follow the reflectivity event corresponding

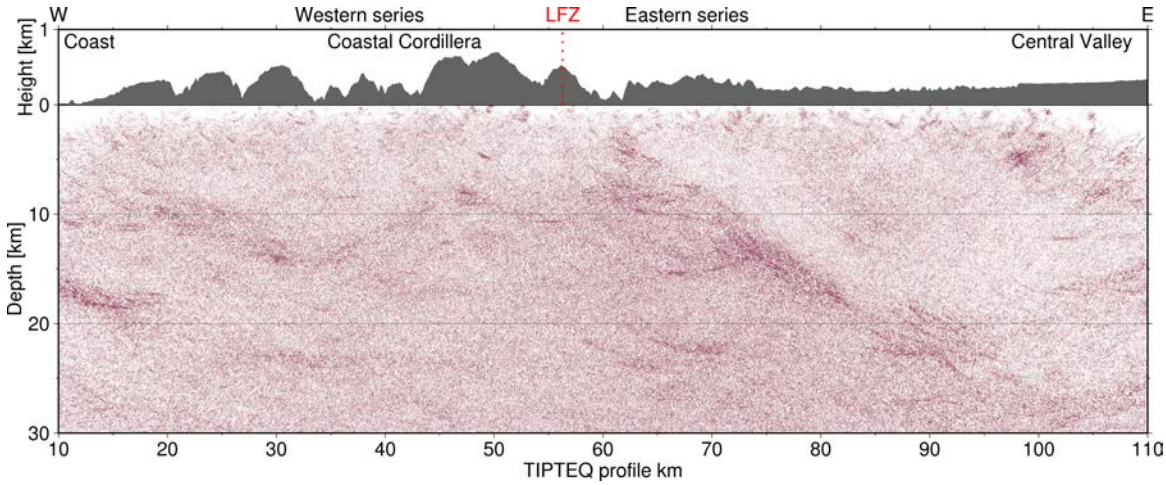

Figure 3.7: Close-up of post-stack depth migrated P-wave reflectivity image with deconvolution. There are reflectivity candidates for the LFZ at shallower depths. Vertical exaggeration ≈ 1. LFZ: Lanalhue Fault Zone.

to the LFZ to shallower depths.

3.3.2 P-wave pre-stack depth migration

Fig. 3.8 (kindly provided by Dr. K. Bauer) shows the P-wave reflectivity along the TIPTEQ profile from pre-stack line-drawing depth migration. Target-oriented filters are applied separately to the data, so that (a) shows the horizontal and shallow to moderately dipping reflectors, obtained from a hyperbolic moveout filter and (b) shows the steep reflectors, which are characterised by retrograde phases with a reverse moveout in the shot gathers (Bauer et al., 2013). (c) Shows the superposition of the obtained steep features and the horizontal and shallow to moderately dipping reflectors.

Most of the horizontal and shallow to moderately dipping reflectors are similar to those observed in the post-stack migrated image. Both the pre-stack and post-stack migration images show a plate interface that is highly reflective east of ∼70 km and less reflective elsewhere. This is not the case in the images shown by Micksch (2008) and Groß et al. (2008). In the first, the plate interface shows a uniform reflectivity from ∼30 to almost 100 km along the profile and the second shows a reduced reflectivity between ∼35 and ∼65 km. A subhorizontal reflector can be seen at profile km 20 to 40, between 4 and 7 km depth. It can be detected in the image of Krawczyk and the SPOC Team (2003), although not so clearly.

The steep west-dipping reflection observed previously in the eastern part of the profile is recovered by the reverse moveout filter. The post-stack migrated image shown in this work (Fig. 3.6), as well as the images of Groß et al. (2008) and Micksch (2008) imaged this event up to 35 km depth. The pre-stack line-drawing migration seems to image it even at shallower depths. It is crucial to keep in mind the low data fold in this part of the profile when interpreting this event.

Another interesting reflector recovered by the reverse moveout (and not observed previously) lies offshore, in the western part of the profile. It is a steep reflector that extends down to 20 km depth. Although the same considerations are necessary as for the eastern west-dipping reflector due to the low data fold offshore, this reflector could correspond to intraplate faulting as depicted by Melnick and Echtler (2006). In particular,

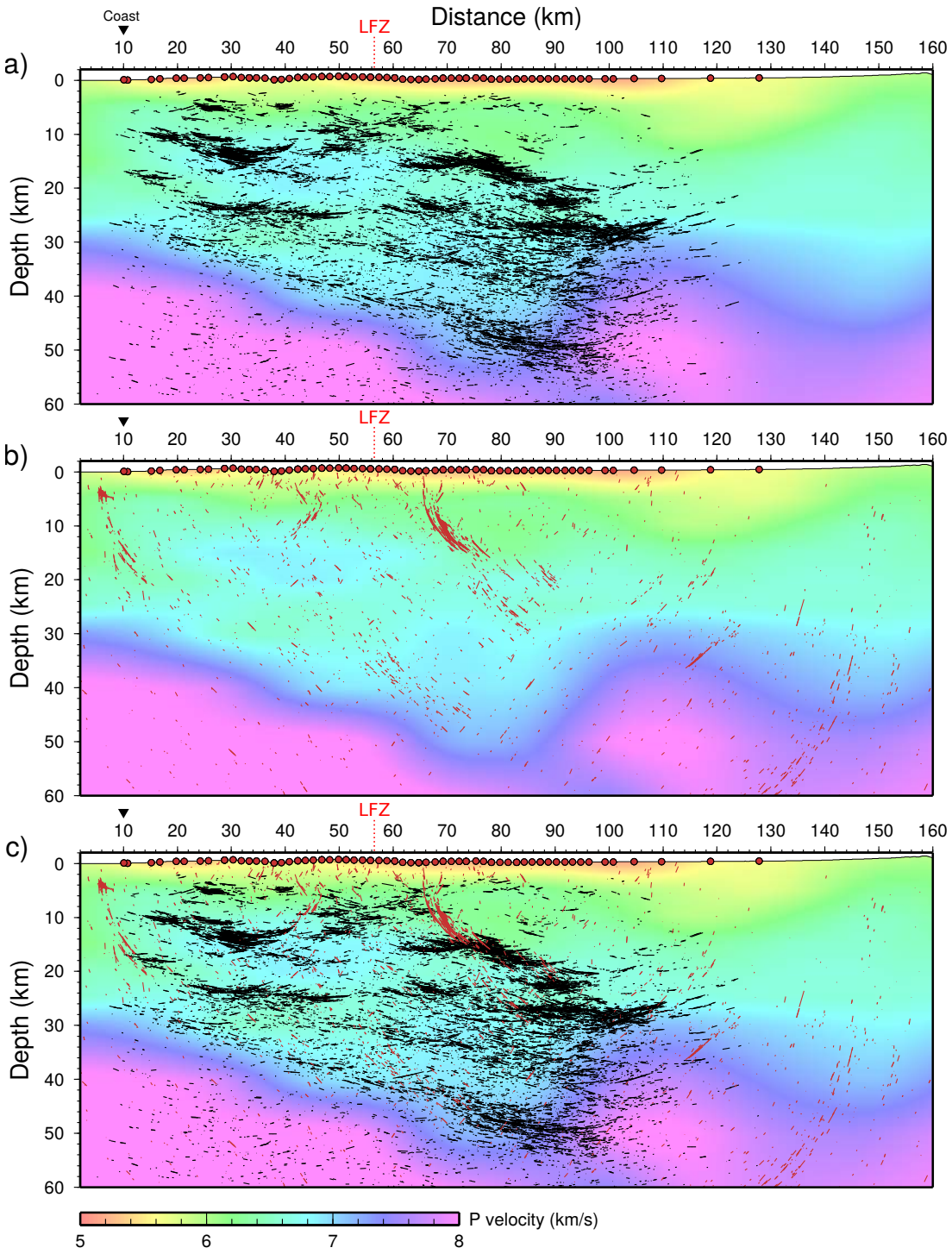

Figure 3.8: Depth migrated pre-stack P-wave reflectivity image. a) Horizontal and shallow to moderately dipping reflectors from hyperbolic moveout filter (black). b) Steep reflectors from reverse moveout filter (red). c) Superposition of reflectors shown in a) and b). Red circles: shot locations. No vertical exaggeration. LFZ: Lanalhue Fault Zone.

it could be the southern end of a seismically active fault (Haberland et al., 2006).

Lastly, a strong reflection is recovered by the reverse moveout filter at ∼65 km down to almost 20 km

depth. As in Fig. 3.7, it is possible to extrapolate this event to the location of the LFZ at the surface. This reflector however, might not necessarily represent the true geometry of the LFZ, as there could be 3D effects that are not considered during the processing (e.g. the LFZ is not completely perpendicular to the profile). For example, Glodny et al. (2008) and Haberland et al. (2006) consider that the dip component of the LFZ is very small. It might also be possible that this event does not represent a fault, but just a velocity contrast (a boundary between different materials).

3.3.3 S-wave post-stack images

Fig. 3.9 shows four processed shot gathers, from both horizontal components and the locations where the shots were executed. In comparison to the shot gathers for P-reflectivity (a similar figure can be observed in Micksch 2008), the S-wave shot gathers show reflections of poorer quality, with reflectivity bands more spread out over time. Yet the events observed in the P-wave post-stack images are identified in the horizontal components with variable intensity.

3.3.3.1 CDP stacked time sections

Fig. 3.10 shows for the S-waves the CDP phase-stacked time sections of the EW and NS components, corresponding respectively to the radial and transverse components. As in the P-wave stacks (Fig. 3.4), horizontal and dipping reflections that are structurally continuous for tens of kilometres are observed. The appearance of the reflections is, however, more spread out over time and the signal-to-noise ratio is lower than the reflectivity bands observed in the P-stacks. Nevertheless, for most of the S-wave reflections, an equivalent P-wave reflection can be found.

Again, three prominent east-dipping reflection bands are observed beneath the western portion of the profile. The fourth (uppermost) band joining the other three east of the LFZ was not as constructively stacked in this case, but it can still be identified in the EW component (A, see Fig. 3.10a). One explanation for its low amplitudes could be that the S-velocity contrast giving rise to this reflection band is not as high as the P-velocity contrast giving rise to the equivalent reflection band in the P-wave stack. The figure shows the amplitudes of this reflection band with the highest possible enhancement, with the different velocity models tested for the S-reflectivity stacking. It is possible that an appropriate deconvolution operator could improve the imaging of this reflector. However, this was not observed in this work, as tests with deconvolution operators did not improve the S-wave image to any degree, unlike for the P-reflectivity processing (see e.g. Fig. 3.5).

Similar to the P-reflectivity stacks, no reflector related to the continental Moho was found. Additionally, no west-dipping steep reflector in the eastern part of the profile between ~33 - 47 s (S-wave times) was observed in either of the two components. It could be that the signal-to-noise ratio did not allow the stacking process to be constructive enough to identify this reflection band above the noise.

In general, Fig 3.10 shows that the quality of the stacking is higher on the EW component than on the NS component. The fact that the utilized velocities favor the stack on one component over the other might be an indication of crustal anisotropy. Evidence for possible crustal anisotropy was also observed in the Chilean subduction zone in tomographic studies (Ramos et al., 2016) and in studies of electrical resistivity

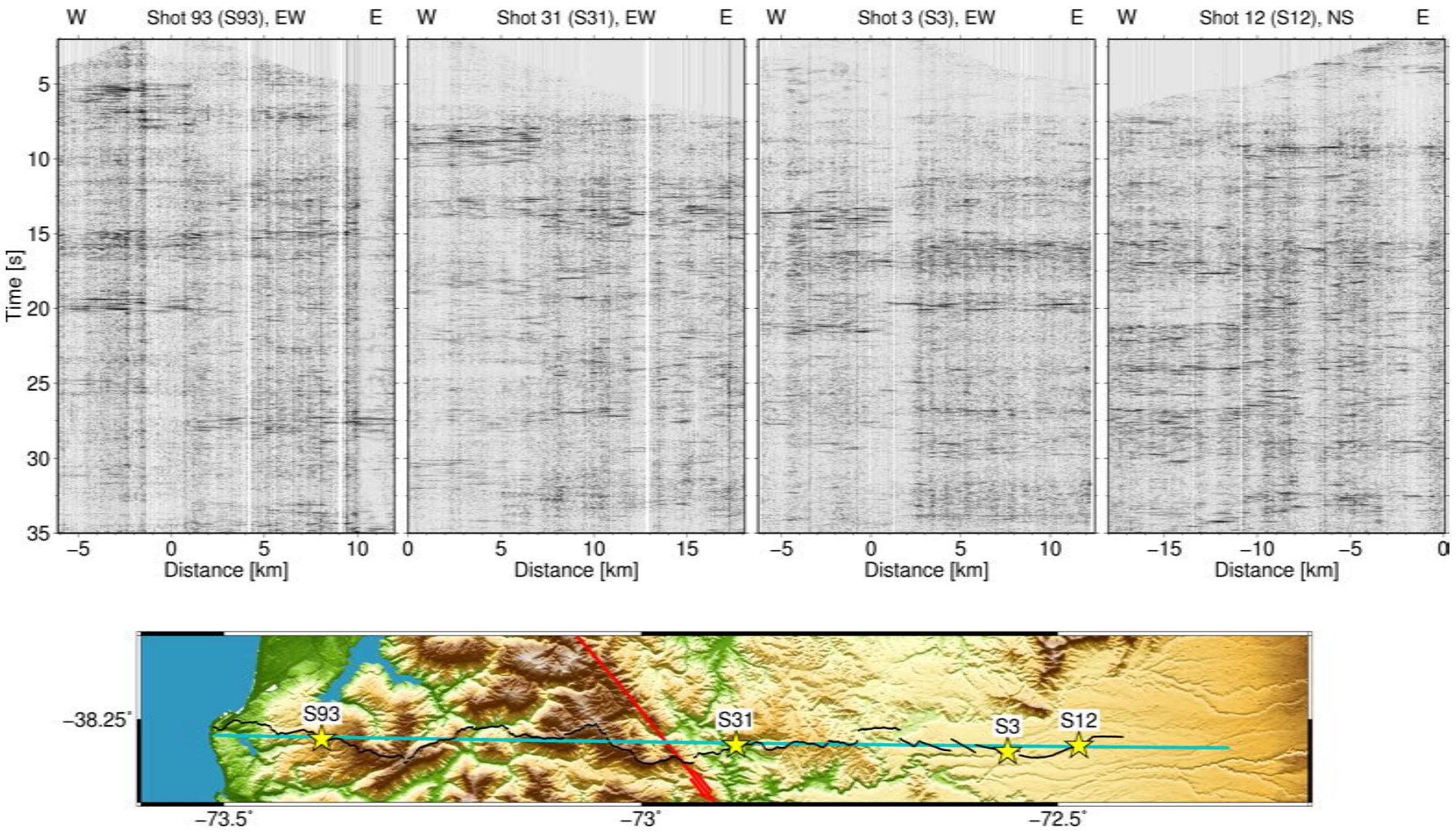

Figure 3.9: Four processed shot gathers (filtered, scaled and infilled. No NMO applied). Cyan line: TIPTEQ CDP line, red line: Lanalhue Fault Zone, black dots: TIPTEQ receiver line, yellow stars: the locations of the four shots. EW: east-west component, NS: north-south component.

(Brasse et al., 2009; Kapinos et al., 2016).

Although in general the reflectivity bands are better imaged in the EW component than in the NS component, in the latter the reflector at ∼5 - 9 s (S-wave times) and between 10 - 40 km (B), interpreted to be a Permo-Triassic (∼200 - 300 million years ago) accretionary wedge by Krawczyk et al. (2006), is better imaged in the NS component. Moreover, the lowermost band corresponding to the plate interface is better imaged in the NS component (C, better even than in the P-stacked reflectivity image) at the eastern end of the profile. Additionally, a new reflector, not observed either on the EW or the vertical component, can be observed above the accretionary wedge, at ∼4 s, between 25 - 30 km (D), coinciding with a similar observation in the pre-stack depth migrated reflectivity image (see Fig. 3.8). Another reflector that is better imaged in the horizontal components than in the vertical component is the west-dipping reflector between 85 - 105 km, at ∼15 - 18 s (E). Moreover, there is an east-dipping reflector that had not been previously imaged in the P-stacks, which can be clearly observed in the EW component, starting at 105 km, between 9 - 15 s (F). Although these reflectors in the easternmost part of the profile seem to be very clearly stacked, their interpretation must be taken with caution, as they lie in a portion of the profile where the CDP fold is very low.

Post-stack depth migrated images derived from the S-reflectivity stacks were not included in this work. The P-reflectivity pre- and post-stack depth migration images already have a good quality and the reflectors observed in the S-wave stacks migrate to about the same depths as the P-reflections, but the images are of inferior quality.

3.3.4 S-wave post-stack depth migration

Figs. 3.11a and 3.11b show the depth-migrated post-stack S-reflectivity images for both horizontal components. In this case, an envelope stacking was carried out, as it shows the reflections more clearly. The letters in this figure show the depth-migrated events marked with the same letters as in Fig. 3.10. Again, the synthetic velocity model used for the Kirchhoff depth migration seems to favor more the east-west component than the north-south component, which can be attributed to crustal anisotropy. In general, the reflections are migrated to the same depths as in the P-reflectivity image (e.g. Fig. 3.6), which validates the synthetic velocities used for the depth migration. The only exception is a portion of the oceanic crust, which looks slightly shallower and steeper than the oceanic crust in the P-reflectivity image, ∼32 versus ∼36 km depth between 30 - 60 km along the TIPTEQ profile. Aside from wrong stacking velocities, the more spread out oceanic crust reflections in the S-reflectivity images than in the P-reflectivity images could explain that they extend over a wider depth range after the migration process. The reflector D (Figs. 3.10 and 3.11), above the Permo-Triassic accretionary wedge was migrated deeper than the possible equivalent reflection in the pre-stack migrated image. However, a reflector that migrated to similar depths is observed in Krawczyk et al. (2006).

The oceanic crust in the western part of the profile is better imaged in the EW component, whereas the NS component shows a clear oceanic crust in the eastern part (C), where the reflection in the EW component loses intensity. The steep west-dipping reflector in the eastern part of the profile, between ∼30 - 70 km depth (G in Fig. 3.11a), seems to be slightly above the noise level in the envelope-stacked EW component image, in contrast with the phase-stacked images. It seems also slightly steeper than in the

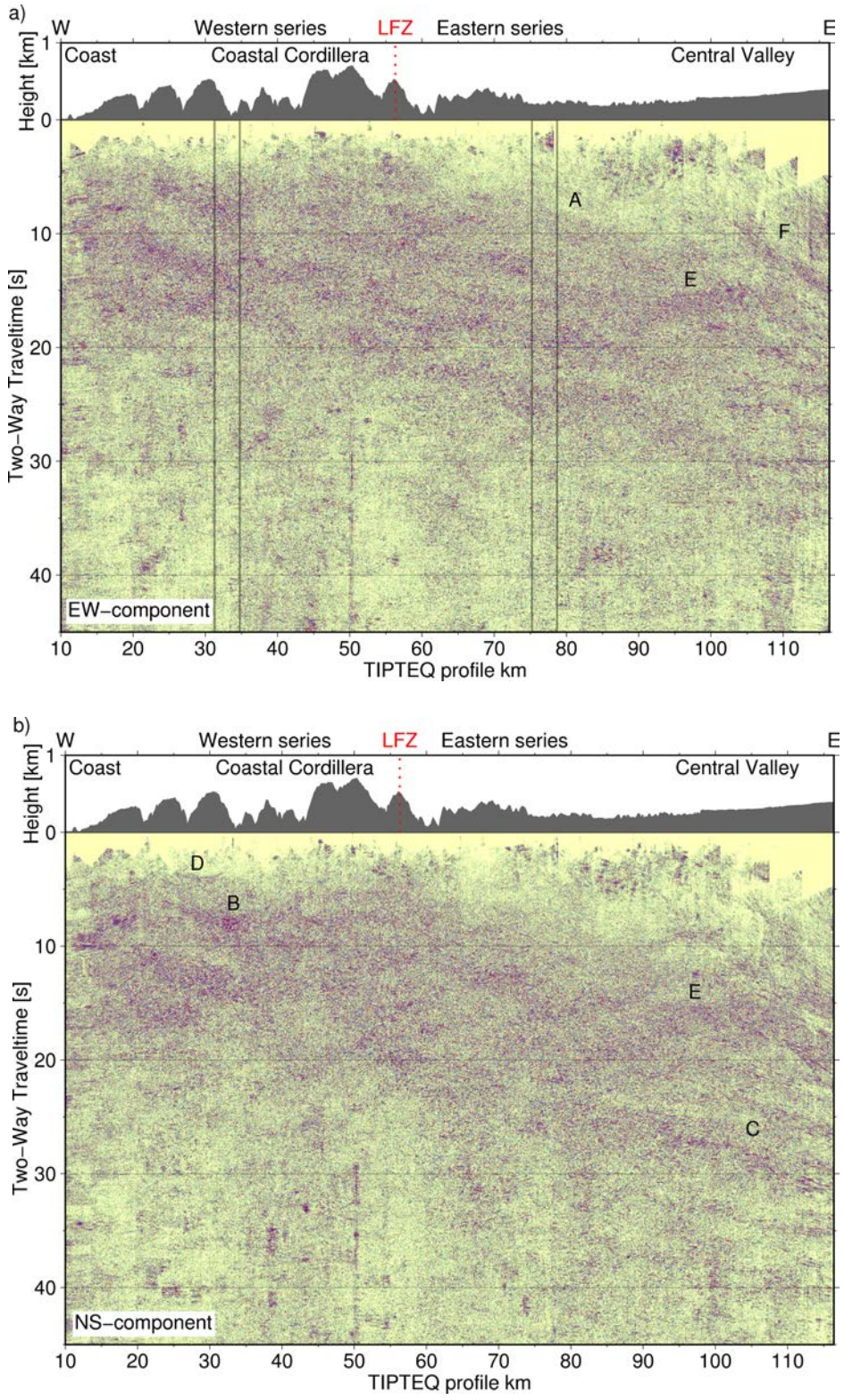

Figure 3.10: S-wave phase stack reflectivity images of the horizontal components along the TIPTEQ profile. a) East-west component, b) north-south component. In a) the rectangles mark the regions for which synthetic seismograms using the reflectivity method were calculated in Chapter 4. LFZ: Lanalhue Fault Zone.

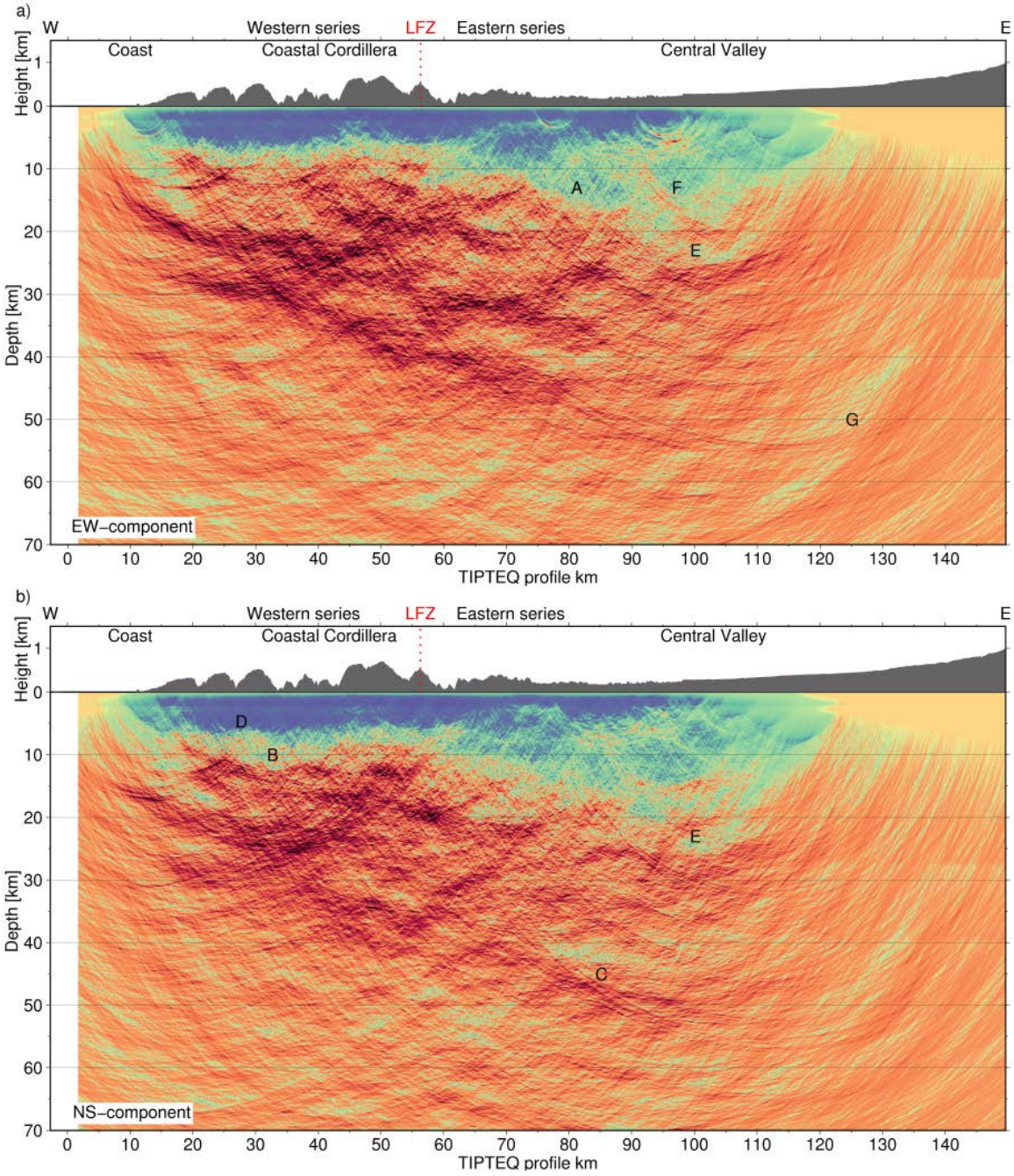

Figure 3.11: Post-stack depth migrated S-wave reflectivity images. Vertical exaggeration ≈ 1. a) east-west component, b) north-south component. Letters marking features in the images are discussed in the text LFZ: Lanalhue Fault Zone.

P-reflectivity image. The different velocities used for the depth migration process at such depths have a greater impact on the migrated reflectors, as shown by Micksch (2008). This reflector looks steeper in the pre-stack migration reflectivity image as well (Fig. 3.8; see also Section 5.3.3). Although not as clear as in the P-reflectivity image, the reflection associated with the LFZ (A) can be recognized in the EW component. Steep east-dipping reflectors in the eastern part of the profile, such as F, must be interpreted with caution

due to the coarse CDP fold in that region.

3.3.5 Seismic images and resolution

Fig. 3.12a shows the vertical and lateral resolution for the P- and S-reflectivity images at every 10 km depth intervals for two different frequencies, as calculated in Section 3.1.5. Fig. 3.12b shows the calculated resolutions in a direct 1:1 comparison with the depth migrated P-reflectivity image. It can be observed how the resolution deteriorates with depth. It is thus concluded that the vertical and lateral resolution is good enough to resolve or detect the obtained reflectivity bands in both the P- and S-reflectivity data.

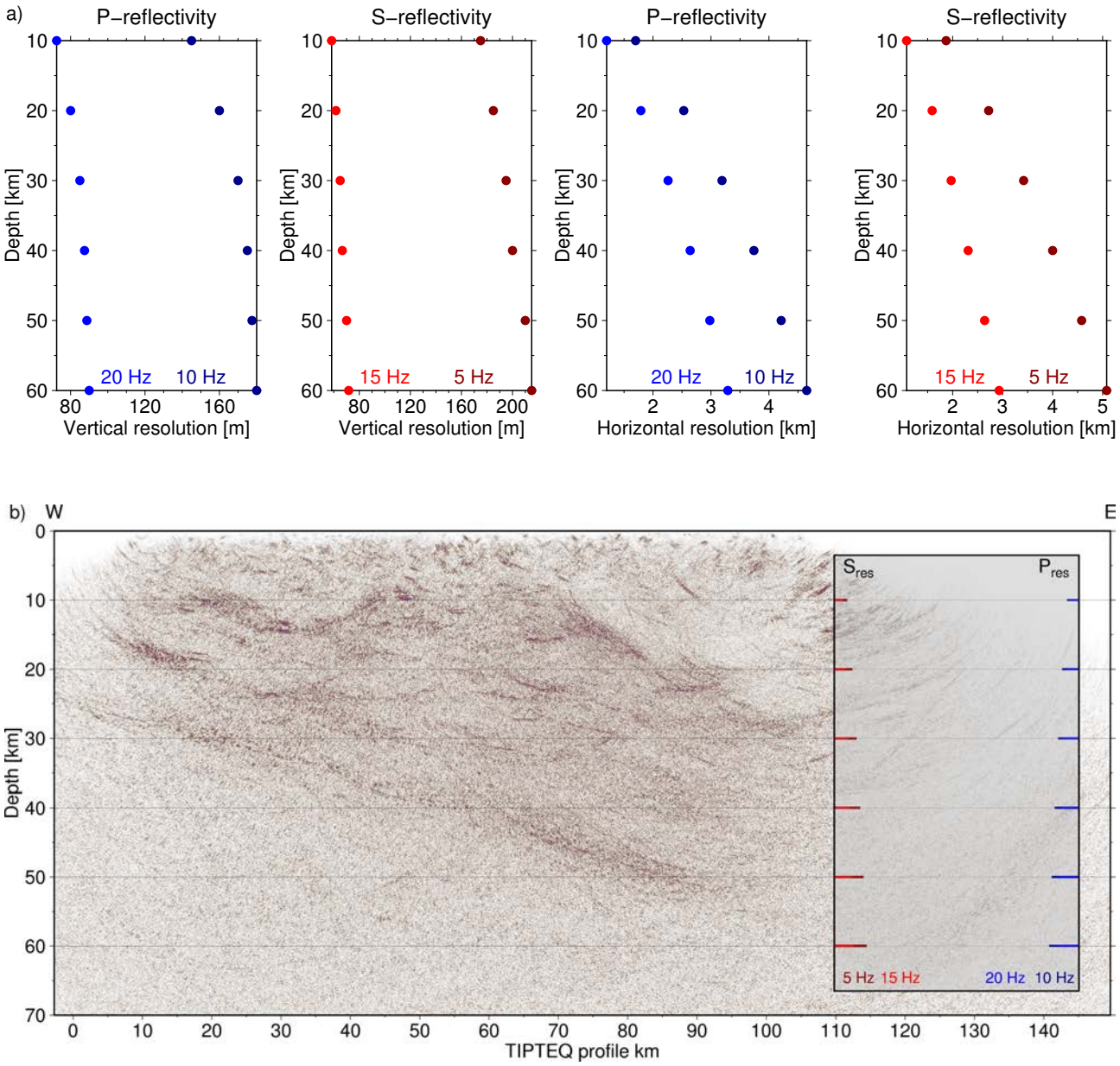

Figure 3.12: a) Vertical and horizontal resolution for P- and S-wave reflectivity, as calculated in Section 3.1.5. b) Comparison of depth migrated P-reflectivity image with the lateral and vertical resolution for P-(blue and dark blue bars) and S-reflectivity (red and dark red bars) in the same scale as the P-reflectivity image. Vertical exaggeration ≈ 1.

Chapter 4

Amplitude ratios and synthetic seismograms modelling

Velocity contrasts that would give rise to the prominent reflectivity bands observed in two different portions of the seismic images obtained in Chapter 3 were modelled. This was done by matching the mean observed amplitude ratios of the reflections in the two portions to synthetic amplitude ratios derived from theoretical seismograms. The theoretical seismograms were calculated using the reflectivity method as described in Fuchs and Müller (1971), which uses 1D P- and S-wave velocity models as input. A comparison of synthetic amplitudes using a flat (1D) velocity model and a dipping model showed that there is no significant difference between the obtained amplitude ratios (see Section 4.3). P- and S-wave velocity models with velocity contrasts across reflectors that produce amplitude ratios that fit the observed ones (plus e.g. Poisson's ratios) are used to characterize the rock types within the subduction zone (Chapter 5). The characterization of the rock types using the results obtained in this chapter is part of a scientific manuscript in preparation.

4.1 The reflectivity method: theory

4.1.1 Introduction

The reflectivity method is a powerful tool in stratified earth models. It can model almost all kinds of waves propagating in elastic or anelastic media with numerical stability and accuracy and for a low computation cost (Ma et al., 2004). Although in previous years, the computation time that reflectivity codes usually required was normally a major practical disadvantage of this method (Fuchs and Müller, 1971; Mallick and Frazer, 1987), nowadays the use of supercomputers reduces that time significantly.

The reflectivity method represents wave propagation in the $f-k$ domain, and it mainly deals with coefficient matrix computation in the frequency-wavenumber ($f-k$) domain (Kennett, 1983). By the use of Fourier transforms (Cooley and Tukey, 1965), the seismic modelling results can be transformed back into the space domain. This modelling is always carried out in a cylindrical coordinate system, so that wave equations can be conveniently reduced to 1D. The method describes wave behavior in stratified earth models in a convenient way, where all wave types can be decomposed into upgoing and downgoing waves and can be decoupled into $P-SV$ and SH waves (Kennett, 1983). Thus e.g. reflections, transmissions,

conversions and multiples can be fully modelled.

The method has the weakness that, as it is a 1D modelling method, other methods such as finite differences are required in the case of more complicated earth models, such as laterally heterogeneous media, and especially for those media with strong lateral velocity gradients.

4.1.2 The reflectivity method

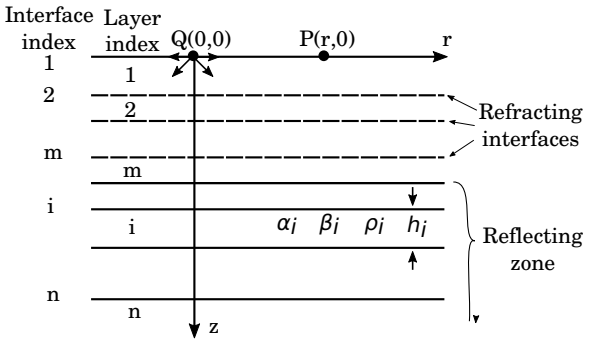

Figure 4.1: Layered medium with the explosive point source Q and the observation point P. Figure redrawn after Fuchs and Müller (1971).

This section is a brief outline of the theoretical background of the reflectivity method as described in Fuchs and Müller (1971).

Fig. 4.1 shows the layered model to which the reflectivity method is applied. It consists of $n-1$ plane, homogeneous and isotropic layers on top of a half-space n. The ith layer has P and S velocity α_i and β_i, respectively, density ρ_i and thickness h_i. An explosive source is assumed at the free surface $z = 0$. The layers 1 to m are assumed to produce only transmission losses and time shifts both for the incident P wave traveling downwards and the reflected P wave traveling upwards to the surface. The compressional reflections are sought from the reflective zone comprising the layers $m+1$ through n.

The potential function of a spherical compressional wave at some distance R from the source in a homogeneous medium is

$$\phi_0(r,z,t) = \frac{1}{R} F\left(t - \frac{R}{\alpha_1}\right) \tag{4.1}$$

where $R^2 = r^2 + z^2$ and $F(t)$ is the excitation function. Its Fourier transform can be expressed as (Fuchs and Müller, 1971)

$$\bar{\phi}_0(r,z,\omega) = \bar{F}(\omega) \int_0^\infty \frac{k}{j v_1} J_0(kr) e^{-j v_1 z} dk \tag{4.2}$$

where $J_0(kr)$ is the Bessel function of the first kind and order zero, j the imaginary unit, k the horizontal wave number and $v_1 = \sqrt{k_{\alpha_1}^2 - k^2}$ the vertical wave number ($k_{\alpha_1} = \omega/\alpha_1$).

Next, the compressional wave is transmitted across the interface 2 and has a potential of the same form as Eq. 4.2, but the integrand includes a transmission coefficient and a second term in the exponential function. The process is continued until layer m is reached, where the incident compressional potential

(upon the reflecting zone) is

$$\bar{\phi_1}(r,z,\omega) = \bar{F}(\omega)\int_0^\infty \frac{k}{jv_1} J_0(kr) P_d(\omega,k) \exp\left[-j\left(\sum_{i=1}^{m-1} h_i v_i + \left(z - \sum_{i=1}^{m-1} h_i\right) v_m\right)\right] dk \tag{4.3}$$

where $P_d(\omega,k)$ is the product of the transmission coefficients of the interfaces 2, 3,..., m for a downgoing wave. Vertical wave numbers of P- (v_i) and S-waves ($v_i' = \sqrt{k_{\beta_i}^2 - k^2}$) occur in $P_d(\omega,k)$.

The potential of the reflected P-wave in layer m is

$$\bar{\phi_2}(r,z,\omega) = \bar{F}(\omega)\int_0^\infty \frac{k}{jv_1} J_0(kr) P_d(\omega,k) \tilde{R}_{pp}(\omega,k) \exp\left[-j\left(\sum_{i=1}^{m} h_i v_i + \left(\sum_{i=1}^{m} h_i - z\right) v_m\right)\right] dk \tag{4.4}$$

where $\tilde{R}_{pp}(\omega,k)$ is the plane wave reflection coefficient (Fuchs and Müller, 1971). The reflected P-wave, transmitted upwards across the interfaces has the following potential in layer 1:

$$\bar{\phi_3}(r,z,\omega) = \bar{F}(\omega)\int_0^\infty \frac{k}{jv_1} J_0(kr) P_d(\omega,k) \tilde{R}_{pp}(\omega,k) P_u(\omega,k) \exp\left[-j\left(2\sum_{i=1}^{m} h_i v_i - z v_i\right)\right] dk \tag{4.5}$$

where $P_u(\omega,k)$ is the product of the transmission coefficients of the interfaces 2, 3,..., m for an upgoing wave.

Finally, the potential of the reflected P-wave at the free surface is

$$\bar{\phi_4} = \bar{F}(\omega)\int_0^\infty \frac{k}{jv_1} J_0(kr) P_d(\omega,k) \tilde{R}_{pp}(\omega,k) P_u(\omega,k) r_{pp}(\omega,k) \exp\left[-j\left(2\sum_{i=1}^{m} h_i v_i + z v_1\right)\right] dk \tag{4.6}$$

and the potential of the reflected S-wave at the free surface is

$$\bar{\psi} = \bar{F}(\omega)\int_0^\infty \frac{k}{jv_1} J_1(kr) P_d(\omega,k) \tilde{R}_{pp}(\omega,k) P_u(\omega,k) r_{ps}(\omega,k) \exp\left[-j\left(2\sum_{i=1}^{m} h_i v_i + z v_1'\right)\right] dk \tag{4.7}$$

where $J_1(kr)$ is the Bessel function of the first order $r_{pp}(\omega,k)$ is the P-P reflection coefficient and $r_{ps}(\omega,k)$ is the P-S reflection coefficient at the free surface.

The horizontal and vertical displacements in layer 1 are:

$$\bar{u} = \frac{\partial\bar{\phi_3}}{\partial r} + \frac{\partial\bar{\phi_4}}{\partial r} - \frac{\partial\bar{\psi}}{\partial z} \tag{4.8}$$

$$\bar{w} = \frac{\partial\bar{\phi_3}}{\partial z} + \frac{\partial\bar{\phi_4}}{\partial z} + \frac{\partial\bar{\psi}}{\partial r} + \frac{\bar{\psi}}{r} \tag{4.9}$$

Thus for $z = 0$, the displacements are:

$$\bar{u} = \bar{F}(\omega) \int_0^\infty \frac{jk^2}{v_1} J_1(kr) P_d \tilde{R}_{pp} P_u \left(1 + r_{pp} - \frac{jv_1'}{k} r_{ps}\right) \exp\left(-2j \sum_{i=1}^{m} h_i v_i\right) dk \tag{4.10}$$

$$\bar{w} = \bar{F}(\omega) \int_0^\infty k J_0(kr) P_d \tilde{R}_{pp} P_u \left(1 - r_{pp} + \frac{k}{jv_1} r_{ps}\right) \exp\left(-2j \sum_{i=1}^{m} h_i v_i\right) dk \tag{4.11}$$

A characteristic feature of the method is the change of the variable of integration from wave number k to the angle of incidence γ at the top of the reflecting zone:

$$k = \frac{\omega}{c} = \frac{\omega}{\alpha_m} \sin\gamma = k_{\alpha_m} \sin\gamma \tag{4.12}$$

With this transformation, P_d, P_u, r_{pp} and r_{ps} depend only on the angle of incidence at the top of the reflecting zone, γ, as long as γ is real. Integration from $k = 0$ to $k = \infty$ becomes $\gamma = 0$ to $\gamma = \pi/2 + j\infty$. For the computation of synthetic seismograms for body waves it is, in general, sufficient to restrict the range of integration from $\gamma = 0$ (vertical incidence) to $\gamma = \pi/2$ (grazing incidence at the top of the reflection zone) (Fuchs and Müller, 1971).

Introducing this change of variable of integration in Equation 4.10 and 4.11 gives:

$$\bar{u} = \bar{F}(\omega) k_{\alpha_m}^2 \int_{\gamma_1}^{\gamma_2} \sin\gamma \cos\gamma J_1(k_{\alpha_m} r \sin\gamma) \tilde{R}_{pp}(\omega, \gamma) G(\gamma) \exp\left(-2jk_{\alpha_m} \sum_{i=1}^{m} h_i \eta_i\right) d\gamma \tag{4.13}$$

$$\bar{w} = \bar{F}(\omega) k_{\alpha_m}^2 \int_{\gamma_1}^{\gamma_2} \sin\gamma \cos\gamma J_0(k_{\alpha_m} r \sin\gamma) \tilde{R}_{pp}(\omega, \gamma) H(\gamma) \exp\left(-2jk_{\alpha_m} \sum_{i=1}^{m} h_i \eta_i\right) d\gamma \tag{4.14}$$

For details of the expressions $G(\gamma)$, $H(\gamma)$ and η_i see Fuchs and Müller (1971).

4.2 Numerical methods

In the calculation of synthetic seismograms using the reflectivity method, the computation of the reflectivity matrix $\tilde{R}_{pp}(\omega, \gamma)$ is the most time consuming step. However, once the reflectivity values have been computed, they are the same for an arbitrary number of distances r (only the argument of the Bessel function is dependent upon the distance). In Equation 4.13 and 4.14 $\tilde{R}_{pp}(\omega, \gamma)$ has to be computed over a range of angles of incidence $< \gamma_1, \gamma_2 >$ with increment $\Delta\gamma$ and over a range of frequencies $< f_1, f_2 >$ with frequency increment Δf. If

$$N_a = \frac{\gamma_2 - \gamma_1}{\Delta\gamma}, \qquad N_f = \frac{f_2 - f_1}{\Delta f} \tag{4.15}$$

are the number of incidence angles and frequencies, respectively, for which $\tilde{R}_{pp}(\omega, \gamma)$ has to be computed, then a total of $N_a \times N_f$ values of $\tilde{R}_{pp}(\omega, \gamma)$ have to be calculated.

Different parameters can be manipulated to minimise computer time. On the one hand, the parameters concerning frequency, duration and angle of incidence (wave number) or phase velocity can be manipulated.

On the other hand, the definition of the reflecting zone, such as the number of overburden layers above the reflecting zone and the number of layers used to approximate transition zones can also be manipulated (Fuchs and Müller, 1971).

The software used for the calculation of synthetic seismograms in this work was developed by Sandmeier (1984), who used a recursive method after Kennett (1983) for the computation of the reflection and transmission matrices. The software is particularly suited to machines with vector and/or parallel processing capabilities.

4.3 Comparison of traveltimes and reflection amplitudes of seismograms obtained using a flat model and a dipping model

In different studies, such as in Fuchs and Müller (1971) and Choy et al. (1980) the computation of synthetic seismograms using the reflectivity method is compared to the computation using other methods (the ray-theoretical method in the former and the full wave theory in the latter, although focusing on core phases). Both studies find that there is a good agreement between the seismograms modelled using both methods, especially when applying a low-pass filter (with cutoff frequency 1 Hz). In particular, they consider it appropriate to apply the reflectivity method to derive models of the Earth's crust.

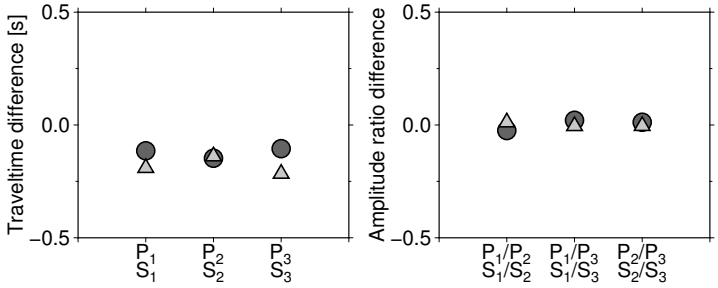

Figure 4.2: Differences in traveltimes (left) and amplitude ratios (right) for three reflections (and pairs of reflections) from a flat model and a dipping layer model. Circles: traveltime and amplitude ratio differences of P-reflections in the vertical component of the synthetic seismograms (flat model minus dipping layer model). Triangles: traveltime and amplitude ratio differences of S-reflections in the radial component of the synthetic seismograms (flat model minus dipping layer model).

As mentioned in Section 4.1.1, the reflectivity method has the weakness of being a 1D modelling method and thus it does not consider the dipping layer interfaces or reflectivity bands, such as those in the reflectivity images of Chapter 3. With the purpose of comparing the effect of neglecting the dip of the reflectors by using a flat-layered model instead of a dipping model to calculate synthetic seismograms, a simple test was carried out. Using the ray-theoretical method (Červený et al., 1977), traveltimes of three different P- and S-reflections and amplitude ratios of each pair of P- and S- reflections were calculated (traveltimes calculated as described in Section 2.1.1) for seismograms obtained using a flat model and a dipping layer model. In the dipping model , a dip of 14° was used, which is similar to the dip derived for the prominent reflection bands in the TIPTEQ NVR data (see e.g. Fig. 3.6). A synthetic source was placed at 20 km along the profile. The amplitude ratios and traveltimes were calculated at 0 km offset. The results can be

observed in Fig. 4.2. The figure shows that the traveltime differences are small and the amplitude ratio differences are negligible for synthetic seismograms calculated using a flat layer model and a dipping layer model, with a dip of 14°.

4.4 Observed amplitude ratios

Synthetic seismograms using the reflectivity method were calculated for two portions (as 1D profiles) along the TIPTEQ CDP line. One portion was chosen in the western part of the profile, at approximately 33 km along the TIPTEQ line and one in the eastern part, at approximately 77 km. In both cases, clear reflectivity bands could be observed in the reflectivity images obtained in Chapter 3. For the location of the profiles, see for example Figs. 3.4, 3.10a (time domain) and Fig. 3.6 (depth domain).

Firstly, the P- and S-reflections to be modelled were identified and located in the time domain (stack image) and depth domain (migrated image) for both profiles. Then, the vertical (P) and radial (SV, or equivalently the EW component) components of the TIPTEQ NVR data were re-processed to obtain stacked images without amplitude enhancers: no automatic gain control (AGC) and no true amplitude recovery (TAR), which change amplitudes in an artificial way, were applied. For each profile, 70 consecutive CDP locations around 33 and 77 km are chosen. For each CDP, the difference between the maximum amplitude and the minimum amplitude of the waveform in a time window containing the reflection of interest was exported from ProMAX and taken as the observed amplitude. Finally, for each pair of P- and S-reflections, the amplitude ratios along the 70 CDPs were obtained. The mean value and standard deviation were calculated for each amplitude ratio along the 70 CDPs. These mean amplitude ratios were the ones which were chosen to be modelled with the reflectivity method.

4.4.1 Western 1D profile

In the western profile at 33 km, three reflections were chosen to model their amplitude ratios and arrival times: two intracrustal, here called $P_{i1}P$ and $P_{i2}P$, and their corresponding S-reflections $S_{i1}S$ and $S_{i2}S$ and one at the top of the oceanic crust, here called $P_{oc}P$, with the corresponding S-reflection $S_{oc}S$. Fig. 4.3 shows the observed reflections and their arrival times in the stacked reflectivity images (with AGC and TAR for visualisation purposes) and for each amplitude ratio along the 70 CDPs, the mean amplitude ratio and corresponding standard deviation are shown. The standard deviations defined the limits that were deemed to be acceptable for the variation in the modelled amplitude ratios with respect to the mean observed ratio.

4.4.2 Eastern 1D profile

In the eastern profile at 77 km, four reflections were chosen to model their amplitude ratios and arrival times: three intracrustal, $P_{i1}P$, $P_{i2}P$ and $P_{i3}P$, and their corresponding S-reflections $S_{i1}S$, $S_{i2}S$ and $S_{i3}S$ and one at the top of the oceanic crust, $P_{oc}P$ and the corresponding S-reflection $S_{oc}S$. Fig. 4.4 shows the observed reflections and their arrival times, as described in Section 4.4.1.

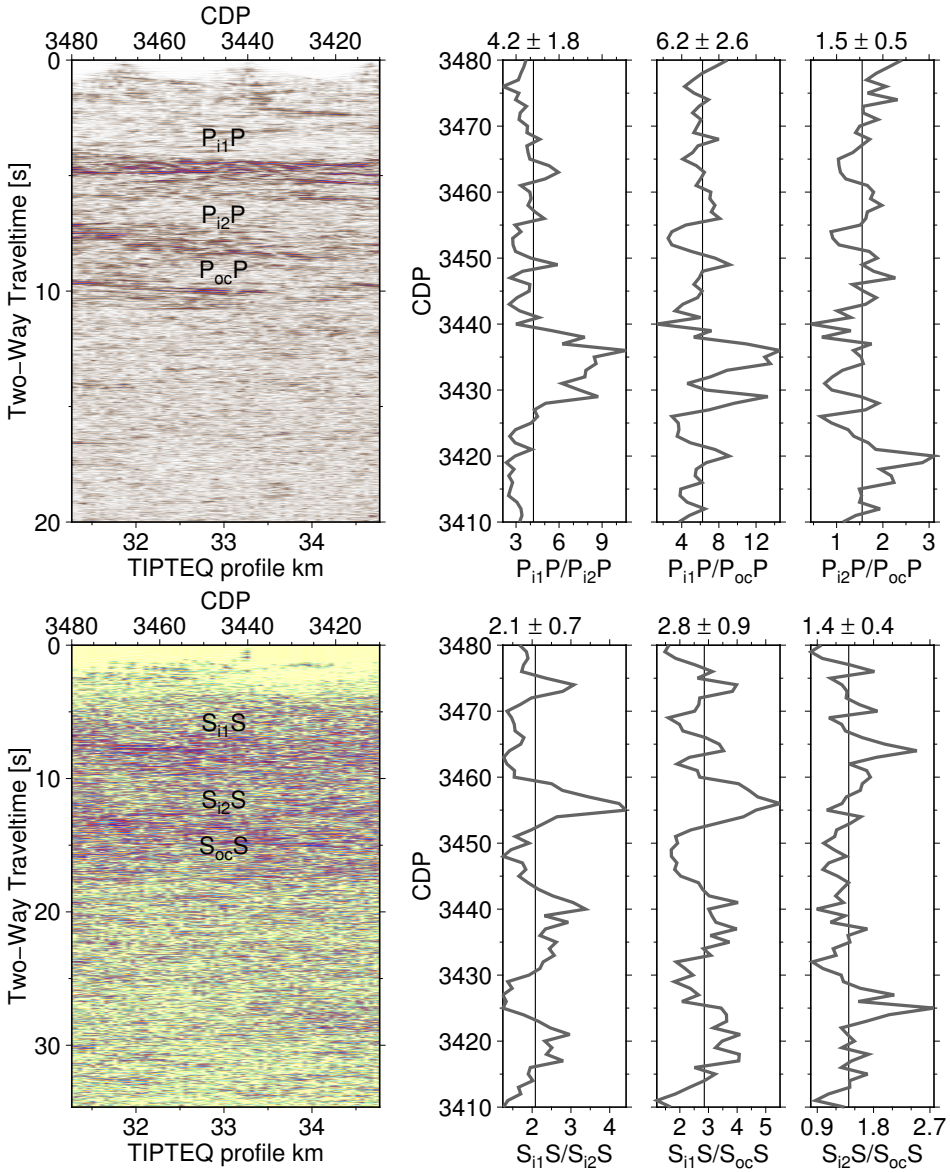

Figure 4.3: Upper panels: the three P-reflections, whose arrival times and amplitude ratios were modelled using the reflectivity method. The right panel shows the observed amplitude ratios for each CDP, with their mean observed amplitude ratio and standard deviation. Lower panels: equivalent observations for the three S-reflections.

4.5 Modelled amplitude ratios and 1D velocity models

Several tests were run on the GFZ high performance computer (HPC) Linux cluster using the software developed by Sandmeier (1984). This software required the setting of some parameters, mostly as switches, of which the following are worth mentioning, e.g. that the full wavefield was calculated, a flat-earth approximation was used, the far-field approximation was used to calculate the Bessel functions (Fuchs and Müller, 1971) and that only the vertical and radial components were calculated (no transversal component). No attenuation (Q_p, Q_s) was used and the density was calculated as a function of the P-velocity for each layer. It also required the 1D P- and S-wave velocity models with their layer thicknesses. These models are

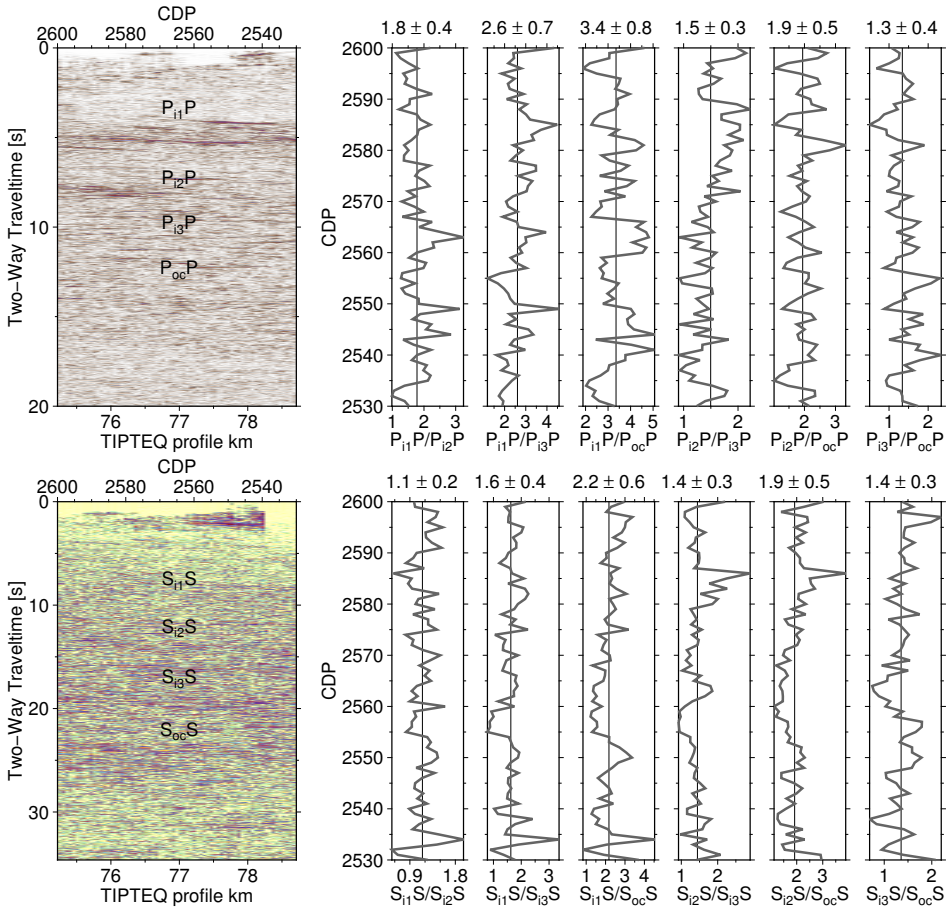

Figure 4.4: Upper panels: the four P-reflections, whose arrival times and amplitude ratios were modelled using the reflectivity method. The right panel shows the observed amplitude ratios for each CDP, with their mean observed amplitude ratio and standard deviation. Lower panels: equivalent observations for the four S-reflections.

described in the following sections for each portion.

One important parameter to consider was the number of ray parameters. Initially, a value of 5000 was used. The program took a few seconds to execute, but a higher level of numerical noise was observed in the synthetic seismograms. In later tests, the used value was 49990. With this increased number of ray parameters, the program took around 10 minutes to execute, but it became more stable and allowed to measure amplitude ratios more accurately.

Velocity gradients between consecutive layers are approximated by steps. The larger the number of steps, the better the approximation, but the longer the execution time. An insufficient number of sub-layers (steps) that approximate a velocity gradient zone can cause false signals or unwanted reflections.

The characteristics of the modelled reflections can be manipulated to fit the observed amplitude ratios or arrival times of the reflections of interest. The arrival time of a reflection of interest can be modified by changing the depth of the velocity interface producing the reflection or the velocity values: shallower interfaces and higher velocities will result in an earlier reflection arrival time. The amplitude of a reflection of interest will be larger for higher velocity contrasts between two consecutive layers and, to a lesser degree, for shallower interface depths. Density plays only a minor role and thus was not manipulated in the different

tests. A reflection with inverse polarity is an indication of a low velocity zone (LVZ). This can be modelled and would represent, for example, the case of the interface of the oceanic crust subducting under the continental mantle, with the oceanic crust having a lower velocity than the continental mantle (see Section 4.5.2).

4.5.1 Western 1D velocity profile

The arrival time windows of the reflections to be modelled ($P_{i1}P$, $P_{i2}P$ and $P_{oc}P$ in the vertical component and $S_{i1}S$, $S_{i2}S$ and $S_{oc}S$ in the radial component) were observed in Figs. 3.4 and 3.10a. To construct the 1D P- and S-wave velocity input models, the depths of the interfaces producing the reflections were observed in Fig. 3.6 and initial velocity values and contrasts were extracted from the SPOC South (at 38.25°S) velocity model (Krawczyk et al., 2006) for the P-wave velocity model. For the 1D S-wave velocity model, the values that were tested always maintained a Poisson's ratio (σ) greater than 0.2 and only varied reasonably with respect to the S-wave velocity values obtained in this work (Section 2.3.2). Thus, a P-wave velocity contrast from 6.3 – 6.6 km s^{-1} at 13 km depth was used, providing the one necessary absolute velocity contrast needed for the amplitude modelling. For this profile, two 1D P- and S-wave velocity

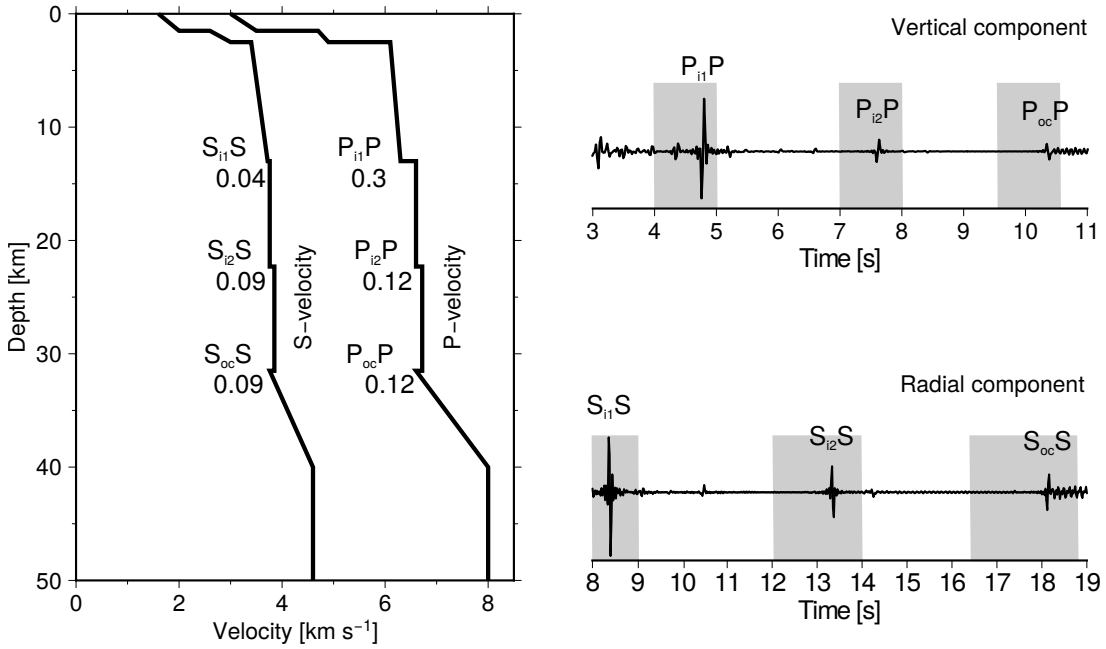

Figure 4.5: Left: first synthetic 1D P- and S-velocity models found to reproduce the observed mean amplitude ratios in the western profile (Fig. 4.3). The numbers indicate the absolute values of the velocity contrasts at each interface. Note the low velocity zone (LVZ) at 31 km depth. Right: synthetic seismograms (vertical and radial components) with the modelled reflectivity phases. The gray shades show the time windows where the reflection phases were observed in the stack images.

models were found among the tests that generated synthetic seismograms whose reflections fit the observed amplitude ratios and arrival times (see Figs. 4.5 and 4.6). Both models are very similar. In fact, the velocity contrasts at the interfaces are identical, except for the interface at 31 km depth (corresponding to the top of the oceanic crust), which produces the reflections $P_{oc}P$ and $S_{oc}S$. One of the models (Fig. 4.5) has a low velocity zone (LVZ) at this depth and thus the reflections $P_{oc}P$ and $S_{oc}S$ show inverse polarity with

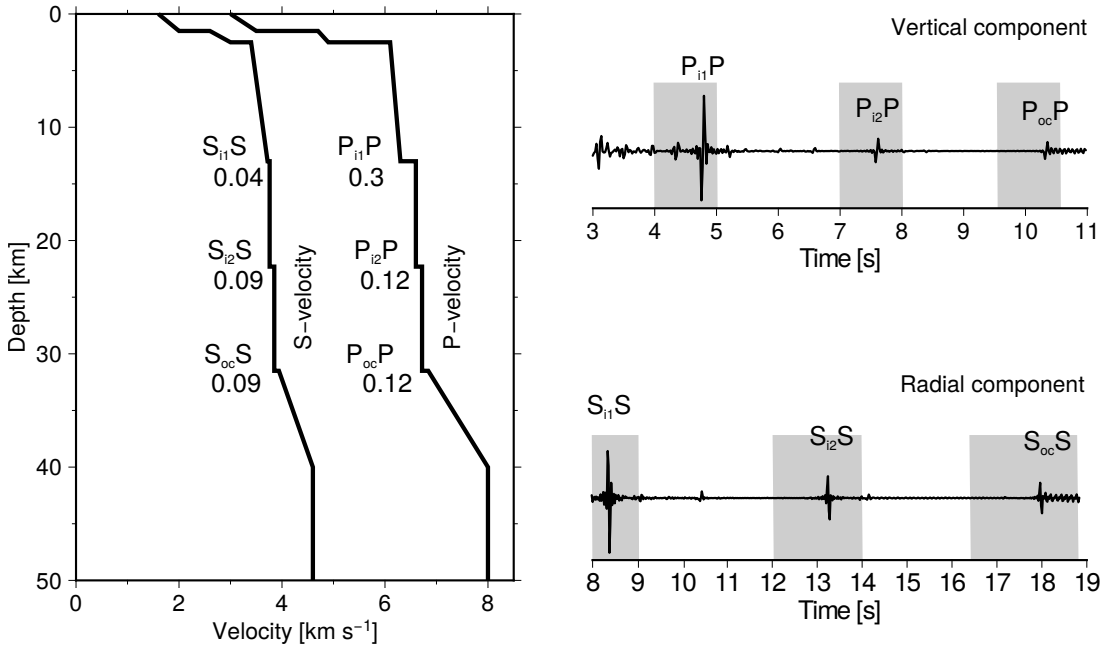

Figure 4.6: Left: second synthetic 1D P- and S-velocity models found to reproduce the observed mean amplitude ratios in the western profile (Fig. 4.3). The numbers indicate the absolute values of the velocity contrasts at each interface. Right: synthetic seismograms (vertical and radial components) with the modelled reflectivity phases. The gray shades show the time windows where the reflection phases were observed in the stack images.

respect to the other reflections. Note also at 13 km depth the high P-velocity and low S-velocity contrast, which could be an indication for a decrease downwards of the quartz content in the rocks. The synthetic seismograms in Figs. 4.5 and 4.6 are plotted without amplitude enhancers (AGC and TAR).

In Fig. 4.7 a comparison was made for each modelled amplitude ratio with respect to the mean observed ones. All of the modelled amplitude ratios lie within one standard deviation of the mean observed amplitude ratios. Although the two shown P- and S-velocity models that produce reflections that fit the observations differ, the absolute velocity contrasts in both models are the same. The two shown P- and S-velocity models are also similar to previously derived models (e.g. Krawczyk et al., 2006; Micksch, 2008; Haberland et al., 2009; Ramos et al., 2016).

4.5.2 Eastern 1D velocity profile

The same considerations as for the western profile were made for the eastern profile. Arrival time windows of the reflections to be modelled ($P_{i1}P$, $P_{i2}P$, $P_{i3}P$ and $P_{oc}P$ in the vertical component and $S_{i1}S$, $S_{i2}S$, $S_{i3}S$ and $S_{oc}S$ in the radial component) were observed in Figs. 3.4 and 3.10a and the depths of the interfaces producing the reflections were observed in Fig. 3.6. Further, initial velocity values and contrasts were extracted from the SPOC South velocity model for the P-wave velocity model and the Poisson's ratio (σ) was kept greater than 0.2. In this profile, the second reflector, generating the phases $P_{i2}P$ and $S_{i2}S$ is considered to be the same event as the first reflector, generating the $P_{i1}P$ and $S_{i1}S$ phases, in the western portion. This is due to eastward dip of the reflection bands (see e.g. Fig. 3.6). Thus, the same P-velocity contrast as was used previously for the $P_{i1}P$ reflection in the western portion was used initially for the $P_{i2}P$

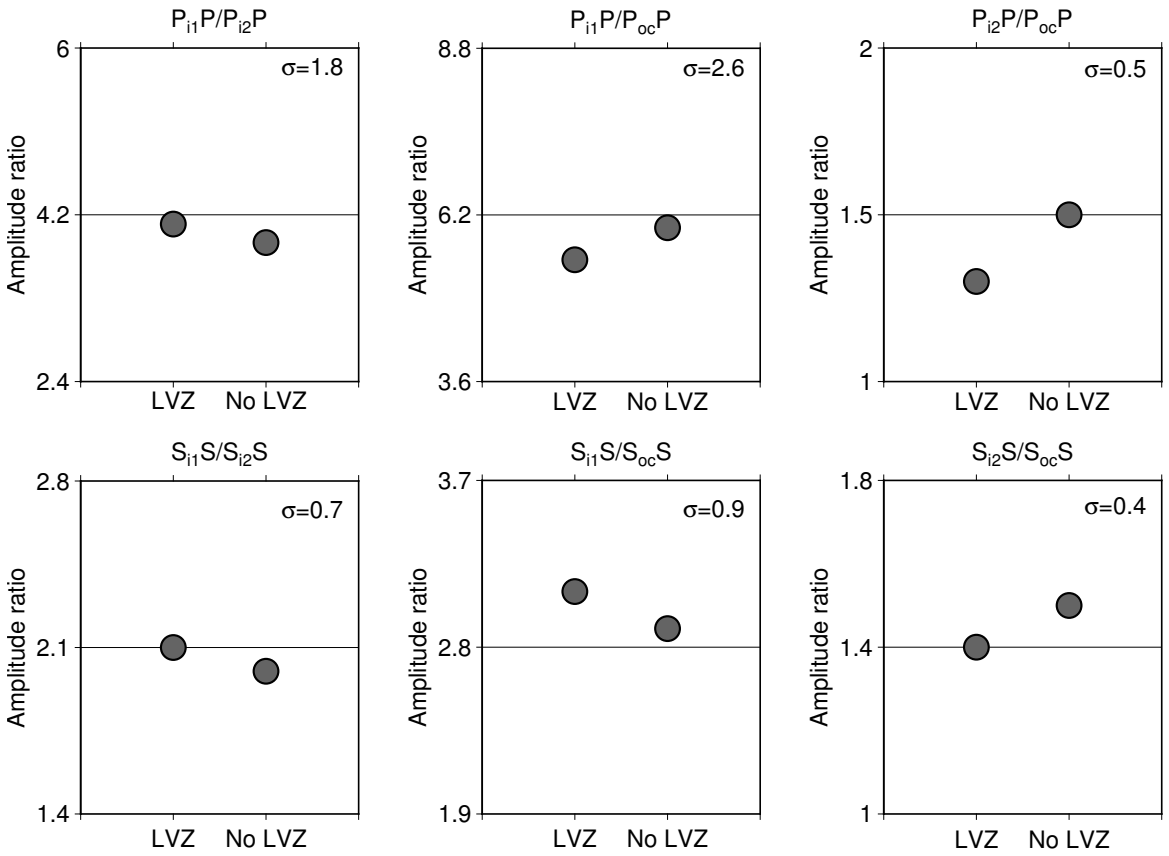

Figure 4.7: Top: calculated P-amplitude ratios for the 1D velocity models with a low velocity zone (LVZ) and without (no LVZ). The line in the centre of each plot marks the observed mean amplitude ratio. The standard deviation (σ) is shown in each case. Bottom: calculated S-amplitude ratios.

reflection in the eastern profile, that is, from 6.3 - 6.6 km s^{-1} at 22 km depth ($\sim$8 s two-way time).

Unlike the western portion, where P- and S-velocity models that fit the observations were found both with and without a LVZ, the absence of a LVZ in this profile could be discarded based on the tectonic geometry as, at 77 km in the TIPTEQ profile, the continental Moho and mantle, with a velocity of $\sim$7.2 km s^{-1} (Krawczyk et al., 2006) lie above the oceanic crust. Not to have a LVZ at the interface between the overlying continental mantle and the underlying oceanic crust would mean that the P-wave velocity of the oceanic crust should be greater than the value of $\sim$7.2 km s^{-1} for the continental mantle, which seems to be unrealistic.

For this profile, two P- and S-wave velocity models were found among the tests that produced synthetic seismograms that fit the observations (see Figs. 4.8 and 4.9). In this case, both models have a LVZ at 42 km depth. Once again, the velocity contrasts for each interface are the same in both models. The two models are shown as an illustration of the non-uniqueness of the 1D velocity models. The first model has a velocity gradient in the layer between the second and third reflections and the second model has a layer with a velocity gradient between the third and fourth reflections. Note the reverberations in the synthetic seismograms between the reflections produced at the top and at the bottom of the layers containing a velocity gradient. These are due to the approximation of the velocity gradient using steps and are nevertheless tiny compared

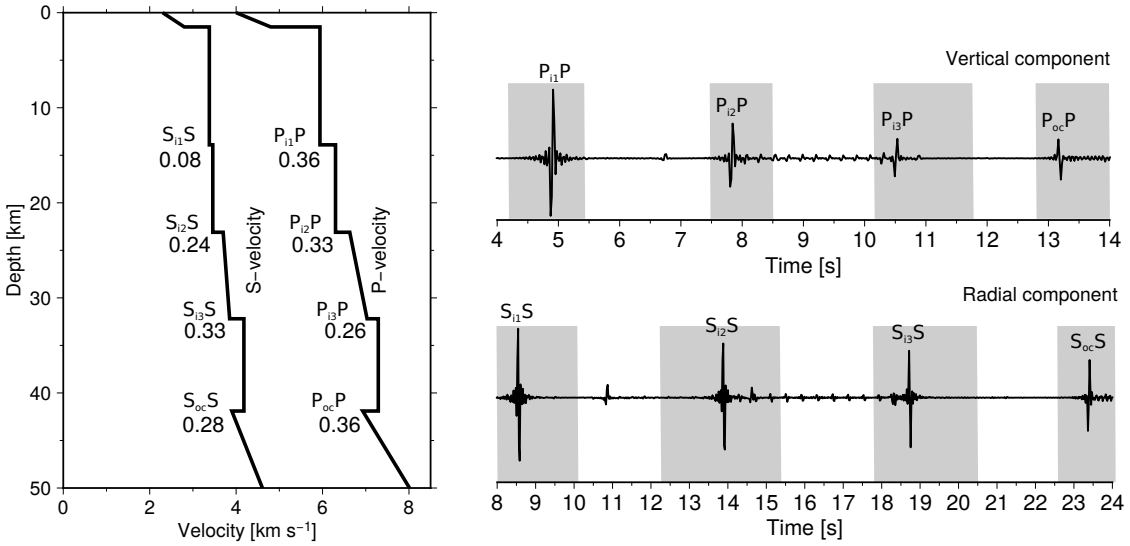

Figure 4.8: Left: first synthetic 1D P- and S-velocity models found to reproduce the observed mean amplitude ratios in the eastern profile (Fig. 4.4). The numbers indicate the absolute values of the velocity contrasts at each interface. Note the low velocity zone (LVZ) at 42 km depth. Right: synthetic seismograms (vertical and radial components) with the modelled reflectivity phases. The gray shades show the time windows where the reflection phases were observed in the stack images.

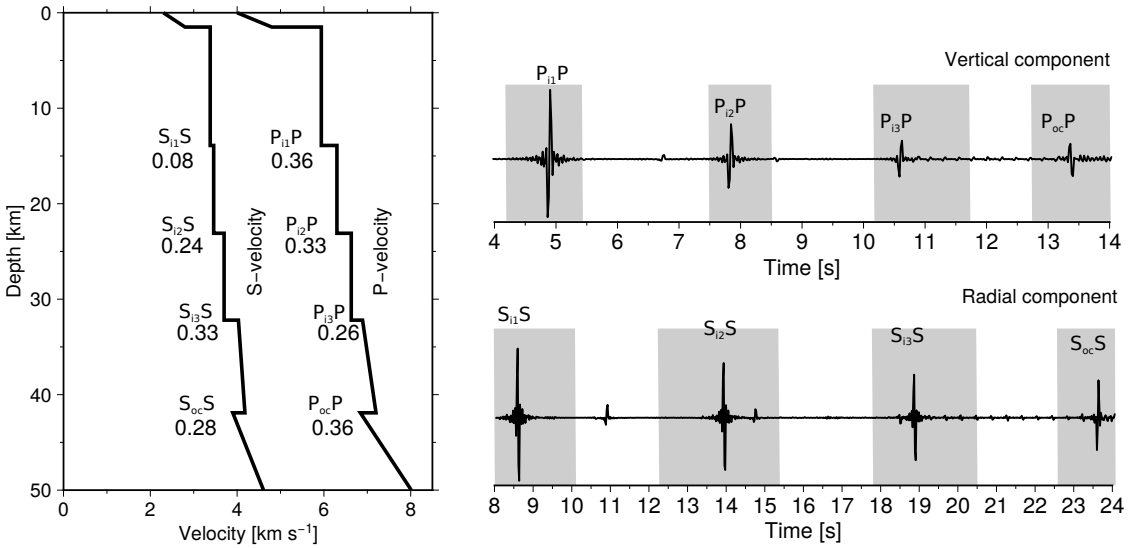

Figure 4.9: Left: second synthetic 1D P- and S-velocity models with a LVZ found to reproduce the observed mean amplitude ratios in the eastern profile (Fig. 4.4). The numbers indicate the absolute values of the velocity contrasts at each interface. Right: synthetic seismograms (vertical and radial components) with the modelled reflectivity phases. The gray shades show the time windows where the reflection phases were observed in the stack images.

to the signals of interest. Also in this case the velocities, although they are non-unique, vary little with respect to those obtained in previous studies (e.g. Krawczyk et al., 2006; Micksch, 2008; Haberland et al., 2009; Ramos et al., 2016). Fig. 4.10 shows the comparison made for each modelled amplitude ratio with respect to the mean observed ones. They deviate with a maximum of one standard deviation from the mean observed amplitude ratios.

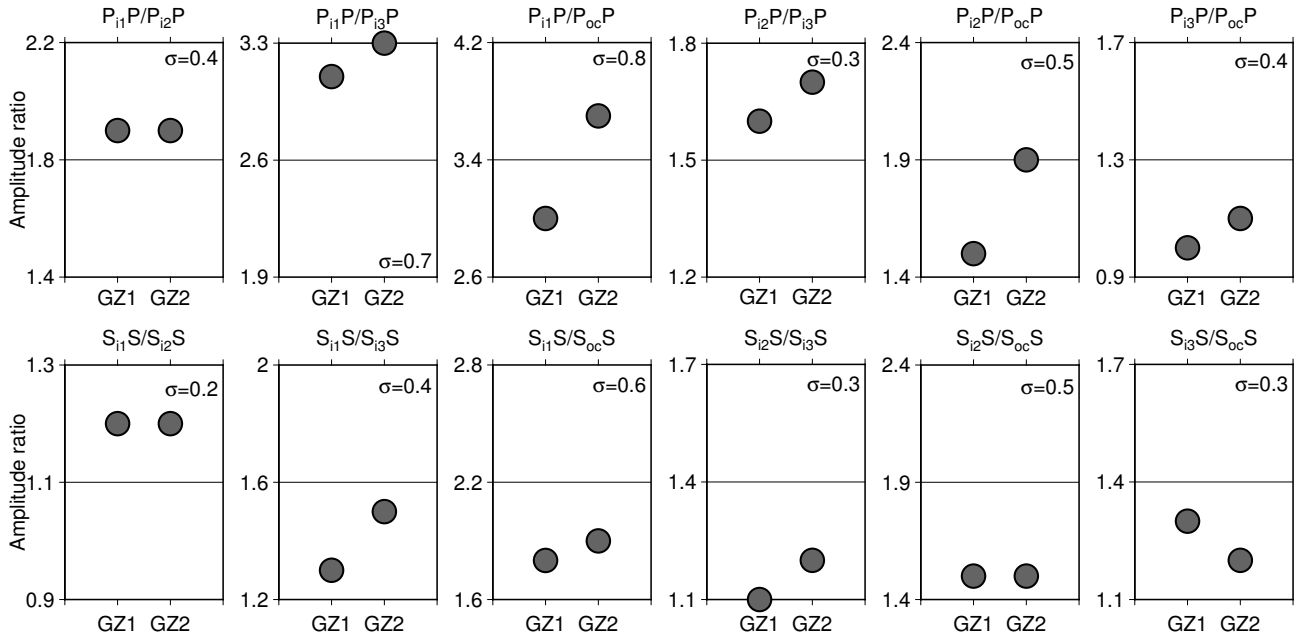

Figure 4.10: Top: calculated P-amplitude ratios for the 1D velocity models: the first with a gradient zone between the second and third intracrustal reflections (GZ1) and the second with a gradient zone between the third intracrustal reflection and the reflection from the top of the oceanic crust (GZ2). The line in the centre of each plot marks the observed mean amplitude ratio. The standard deviation (σ) is shown in each case. Bottom: calculated S-amplitude ratios.

Finally, an attempt was made to find an indication in the P-reflectivity stacked data of the stacked P wavefield of a low velocity zone at the top of the oceanic crust, in the form of a $P_{oc}P$ reflection with reverse polarity. For this purpose, the stacked data in the CDP range corresponding to the eastern profile (CDP 2530 to 2600) were stacked to see if they could be summed constructively to show the different reflections. The result can be observed in Fig. 4.11. The data used for the stack had the TAR and AGC applied. Having enhanced amplitudes should increase the chances of obtaining a constructive sum of the reflections along the CDPs, especially for those generated at greater depths. The stack seems to show at least three of the four modelled reflections, namely, $P_{i1}P$, $P_{i2}P$ and $P_{oc}P$, with the last one possibly having a reverse polarity with respect to the other two. In Fig. 4.11, the stacked data can be compared to the modelled reflections. However, real data have different levels of noise in each trace. This may have caused, for example, that the reflection $P_{i3}P$ stacked only poorly, or at least not to the point to be as recognizable above the noise as the other three.

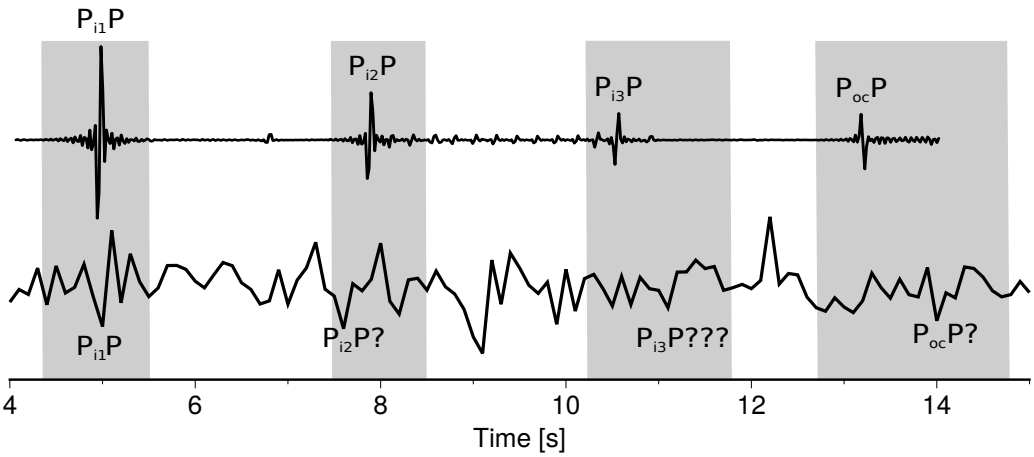

Figure 4.11: Top: synthetic seismogram (vertical component) from Fig. 4.8. Bottom: stacked P-stack (with TAR and AGC) in the CDP range 2530 - 2600. Some of the reflections seem to constructively stack. Gray zones: time windows where the reflections of interest were observed.

Chapter 5

Discussion: integrative interpretation of the results

To obtain a detailed image and knowledge of the petrophysical properties and rock types within the studied portion of the Chilean subduction zone at 38.25°S, the 2D S-wave velocity model obtained in Chapter 2, the P- and S-wave post-stack and pre-stack reflectivity images obtained in Chapter 3 and the synthetic 1D P- and S-wave velocity models from synthetic seismograms and amplitude ratio modelling obtained in Chapter 4 were correlated with the results of other studies in the zone. Such studies included e.g. GPS, magnetotellurics, field geology, thermomecanical and gravimetric research and some of them were carried out in close collaboration between German and Chilean institutions.

Part of the integrative interpretation of the results was published in Ramos et al. (2016). A second publication (submitted) includes the final results of this work, focusing in the post-stack P- and S-reflectivity images and synthetic seismograms and amplitude ratio modelling. A third publication will focus in the pre-stack line-drawing migration images, a comparison with post-stack reflectivity images and their interpretation for this subduction zone.

5.1 2D Poisson's ratio model along 38.25°S

With a P- and S-wave velocity model it is possible to derive a Poisson's ratio model. The Poisson's ratio (σ) is commonly used to evaluate the mineralogical composition, porosity, structure and the existence of fluids within a rock. In addition to P-wave and/or S-wave velocities it narrows the range of possible rock types in an interpretation (Christensen, 1996).

In terms of the S-wave (v_s) and P-wave (v_p) velocity, the Poisson's ratio is

$$\sigma = \frac{v_p^2 - 2v_s^2}{2(v_p^2 - v_s^2)} \tag{5.1}$$

and the Poisson's ratio uncertainty ($\Delta\sigma$) is (see e.g. Contreras-Reyes et al., 2008b)

$$\Delta\sigma = \frac{(v_p/v_s)^2}{((v_p/v_s)^2-1)^2}\sqrt{\left(\frac{\Delta v_p}{v_p}\right)^2+\left(\frac{\Delta v_s}{v_s}\right)^2} \tag{5.2}$$

To obtain a Poisson's ratio model, a P-wave velocity model that covered the same area as the 2D S-wave model obtained in Chapter 2 was necessary. The P-wave velocity model from TIPTEQ active source data obtained by Micksch (2008), down to 2 km depth and the P-wave velocity model from local earthquake tomography obtained by Haberland et al. (2009), starting from 2 km and down to 75 km depth were merged to generate such model. Equation 5.1 was applied in a grid point way using the P- and S-wave velocity

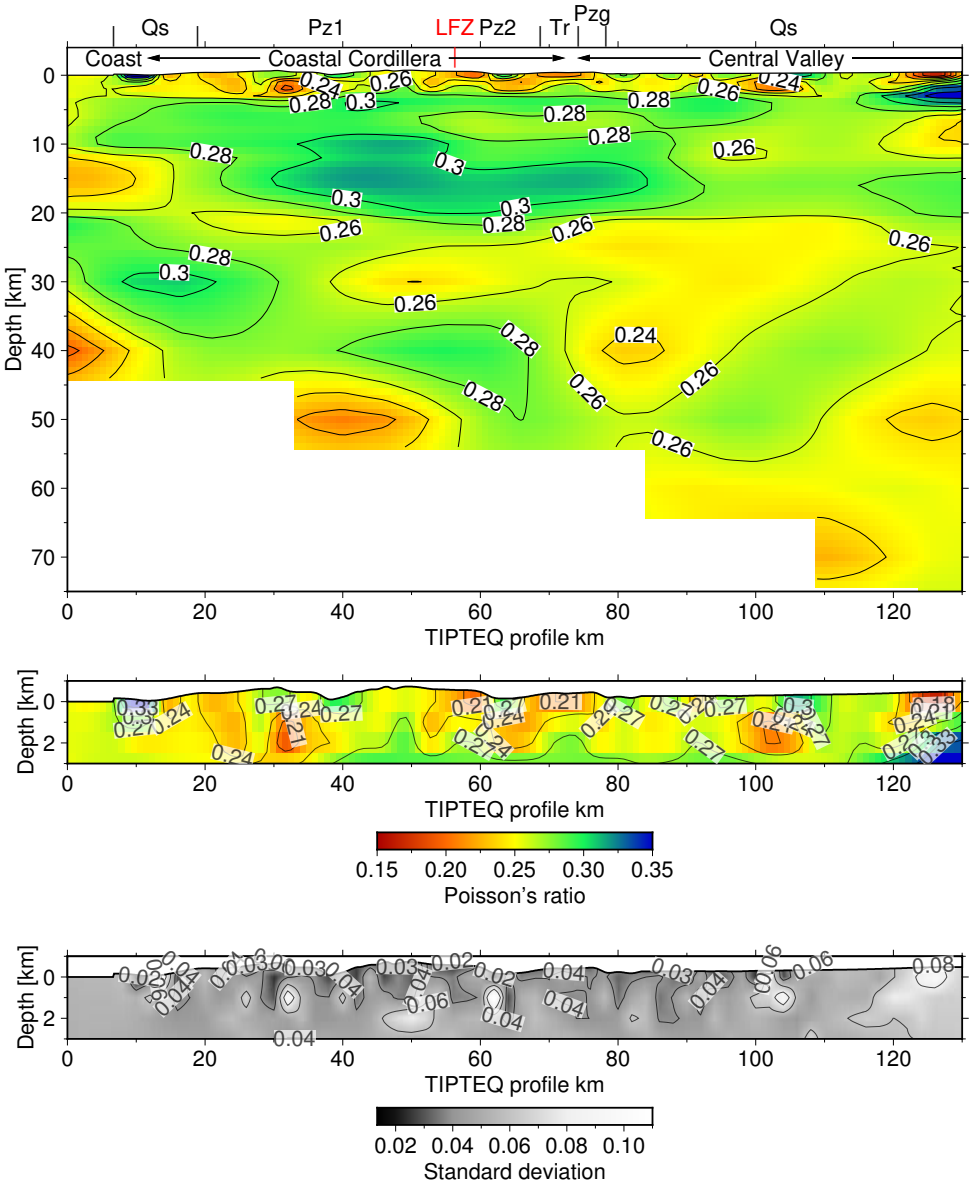

Figure 5.1: Poisson's ratio along 38.25°S. Middle: close-up of the first 3 km depth. Bottom: Poisson's ratio uncertainties in the top kilometres of the profile. Location of the Lanalhue Fault Zone (LFZ) and the geological units as in Fig. 2.7.

models. The Poisson's ratio model along 38.25°S can be observed in Fig. 5.1, along with uncertainties in the topmost part of the Poisson's ratio model (from the P- and S-wave velocity models from the TIPTEQ active source data of Micksch, 2008 and Ramos et al., 2016). The uncertainties in the P-wave velocity model from active source data range between 0.15 and 0.2 km s^{-1} (Ramos et al., 2016). They are slightly higher than those for the S-wave velocity model because of the smaller spacing of 0.5 km horizontally and vertically of the inversion nodes in the P-wave velocity model (Micksch, 2008). Using Equation 5.2, the Poisson's ratio uncertainties are obtained and they range between 0.02 and 0.06 in the area with good ray coverage (see Fig. 2.7). Down to 2 km depth, uncertainties are 0.05 on average. For depths greater than 2 km, Poisson's ratio uncertainties are calculated from the maximum P- and S-wave velocity uncertainties (see Sections 2.2.4 and 2.3.2). The maximum Poisson's ratio uncertainty is 0.02.

A mean Poisson's ratio value of 0.27 is mostly observed along the profile. This value is essentially the same as the global average of 0.265 - 0.27 for continental crust (Zandt and Ammon, 1995; Christensen, 1996). High Poisson's ratio anomalies are observed in different parts of the profile. A clear example is in the central part of the image, between 10 and 20 km depth. This anomaly is significant as it has Poisson's ratios of 0.3 - 0.31 and the maximum uncertainty is 0.02 in this region. They are also observed as clusters just beneath the surface along the profile and also between the top of the subducting plate and the oceanic Moho. Low Poisson's ratio anomalies are also observed in the first few kilometres depth and under the oceanic Moho. The anomalies in the oceanic crust and mantle are probably significant, as they often have Poisson's ratios greater than 0.29 or less than 0.25 and the maximum uncertainty is 0.02 in this region.

5.2 S- and P-wave velocity and Poisson's ratio anomalies from TIPTEQ active source data and observed geological units

The obtained S-wave velocity model from TIPTEQ seismics in Section 2.1.2 shows velocity anomalies that can be compared to those observed in the P-wave velocity model obtained by Micksch (2008) and at the same time with the Poisson's ratios obtained in Section 5.1. Fig. 5.2 summarizes the main P- and S-wave velocity and Poisson's ratio anomalies down to 2 km depth. Similar high- as well as low-velocity anomalies can be observed in both velocity models. High velocity anomalies between 1 and 2 km depth can be repeatedly observed in both models. In the S-wave velocity model, one such anomaly at ∼64 km reaches particularly high values. Although the resolution tests (see Fig. 2.8) suggest that such a small-scale anomaly is difficult to resolve, it is quite faithfully recovered by the model-recovery test (see Fig. 2.9). Similar low-velocity anomalies are observed just beneath the surface in both models, indicating the presence of weathered rock and sedimentary basins. Such anomalies can be observed near the coast at ∼11 km and in the Central Valley at ∼80 - 90 km and ∼98 - 112 km. According to geological maps of the area, young sedimentary rocks are present near the coast and in the Central Valley (SERNAGEOMIN, 2003; Melnick and Echtler, 2006). Jordan et al. (2001) have shown that late Oligocene - early Miocene (ca. 24 million years ago) sediments in the Central Valley in the study region reach thicknesses of up to 3 km. Some low-velocity sediments are also present within the Coastal Cordillera, where hard metamorphic rocks of Paleozoic age (ca. 245 - 570 million years ago) dominate (SERNAGEOMIN, 2003). An anomaly with especially low P- and S-wave velocities is located at ∼64 km, east of the Lanalhue Fault Zone (LFZ) above the high-velocity

anomaly mentioned above. Its location coincides with the location of the eastern series (see Fig. 2.7).

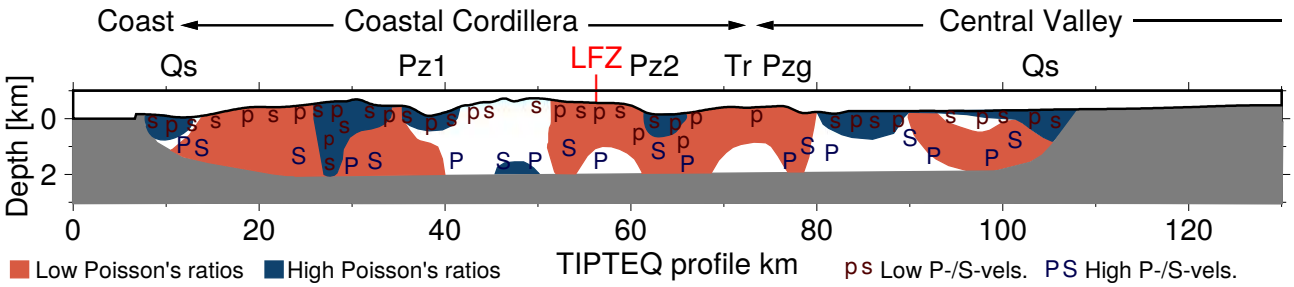

Figure 5.2: P- and S-wave velocity and Poisson's ratio (σ) anomalies from the models obtained using the TIPTEQ active source data. Low σ in bright red, high σ in bright blue. Capital dark blue P and S: high P- and/or S-velocity anomaly. Small dark red p and s: high P- and/or S-velocity anomaly. Low resolution areas (gray zones) are not included in the interpretation. LFZ: Lanalhue Fault Zone. Geological units as in Fig. 2.7.

An interpretation of the petrography can be made using the P- and S-velocities, as well as Poisson's ratios (σ) searching in rocks and mineral catalogues, such as the one of Christensen (1996) or in Stadtlander et al. (1999), with a database available at GFZ. To use it, certain parameters for the study zone (e.g. the heat flux for Chile was taken from Davies, 2013) were specified. For this interpretation it was assumed that the seismic velocities are unaffected by anisotropy.

Very low P-velocities ($\leq$ 4.5 km s^{-1}, Micksch, 2008) and S-velocities ($\leq$ 2.5 km s^{-1}, Ramos et al., 2016) observed at the surface, for example near the Coast (10 km), in the Coastal Cordillera (at 27 - 40 km or around 65 km) or in the Central Valley (80 - 90, 98 - 110 km) do not find a candidate in the catalogues, as the rocks in the catalogues tend to be fresh specimens. Thus, the observations of very low velocities are interpreted as either uncompacted sediments or very weathered igneous and metamorphic rocks. Ardiles (2003), for example, reports a non-uniform coverage composed of marine sedimentites of Miocene-Pliocene age (ca. 3 - 23 million years ago) and sedimentary deposits of aeolian and fluvial origin of Pleistocene-Holocene age (less than 2 million years ago) along the Western Series (WS). Although contrasting mineralogical and petrographic variations are observed when crossing from the Eastern series (ES) to the WS (Burón, 2003), this contrast cannot be observed from the velocity and Poisson's ratio models alone. For the following observations summarized in Fig. 5.2, the P-wave velocities are extracted from Micksch (2008), whereas the S-wave velocities and σ are extracted from Ramos et al. (2016). The catalogue of Christensen (1996) is used considering a pressure of 200 MPa.

The low P- (4.3 - 5.8 km s^{-1}) and S-wave (2 - 3.6 km s^{-1}) velocity and high σ (0.28 - 0.34) anomalies at the coast, around 10 km and down to 1 km depth are probably due to young sediments from the Quaternary (Melnick and Echtler, 2006; SERNAGEOMIN, 2003). However, a non-weathered plagioclase-rick rock, such as andesite, serpentinite or granulite, could explain the anomalies (Christensen, 1996; Stadtlander et al., 1999).

The onset of sediments in the Central Valley is observed at 80 km. The Central Valley is composed by Quaternary sediments (Melnick and Echtler, 2006; SERNAGEOMIN, 2003) and these should thicken east of $\sim$110 km (outside the confidence area). The same non-weathered rocks as near the coast could explain the velocities and σ anomalies in the Central Valley. Around 90 km there is a thinning of the low velocity and high σ anomalies. This was interpreted by Micksch (2008) to be the Coastal Batholith (CB) beneath a

sedimentary cover. The CB is an intrusive body that crops out to the east of the accretionary metamorphic complex and is composed of calc-alkaline granitoids (Deckart et al., 2014). In Fig. 5.2, the low σ anomaly representing the CB merges a low σ anomaly around the LFZ, making it indistinguishable, but searching in the catalogues, some granitoids are found that fit the anomalies corresponding to the CB (Pzg), such as granite gneiss and trondhjemite. Other quartz and plagioclase rich rocks found in the catalogues of Stadtlander et al. (1999) and Christensen (1996) that are observed in the ES (Hervé, 1988; Burón, 2003; Glodny et al., 2008) and fit the anomalies are metagraywacke, amphibolite and granulite.

The onset of the WS at ∼15 km is marked by a low σ anomaly, which reaches values as low as 0.195 at ∼33 km. The petrography on the WS is rich in plagioclase feldspar and quartz (Hervé, 1988; Ardiles, 2003; Glodny et al., 2005). Additionally, serpentinites are present. Their presence is explained by the basal accretion that originated the WS (Glodny et al., 2008). Rocks obtained from the catalogue that fit the observed velocity and σ anomalies, as well as the petrographic observations include granulite, trondhjemite, anorthosite and gneiss. Some high velocity anomalies, faithfully recovered by the resolution tests (e.g. at 45 - 50 km, between 1 - 2 km depth) are part of a high velocity trend beneath the WS. It is interesting that, among others (e.g. diorite, phyllite, gneiss and schist), serpentinite or partially serpentinized peridotite are found in the catalogue of Stadtlander et al. (1999) that explain these high velocities, which would again support the idea of basal accretion of the WS.

5.3 Geometry, composition and processes in the southern Chile subduction zone at 38.25°S

This section summarizes and gives an interpretation of the main results of this work, which was, to some extent, a continuation of the work of Micksch (2008). Thus, it compiles the results of different multidisciplinary studies in the southern Chile subduction zone, to obtain an updated and extended image of this area. Fig. 5.3 shows the integrative interpretation of the geometry, composition and processes in the subduction zone along the TIPTEQ profile at 38.25°S.

5.3.1 Poisson's ratio anomalies in the subduction zone

The uppermost part of the lithosphere of the downgoing Nazca plate is characterized by a large-scale high Poisson's ratio anomaly of 0.28 - 0.30 (see Figs. 5.1 and 5.3), corresponding to v_p/v_s values of about 1.88 (Haberland et al., 2009). This represents the hydrated oceanic crust and serpentinized oceanic mantle that can be observed even down to 70 km depth in the eastern part of the model. According to Haberland et al. (2009), the rocks that explain the values of this large-scale anomaly are gabbro or metamorphosed mid-oceanic ridge basalt (MORB). High Poisson's ratios of ∼0.28 - 0.33 in the oceanic crust and ∼0.29 in the upper mantle have also been observed offshore at 43°S (Contreras-Reyes et al., 2008b). Strong lithospheric hydration, which was independently corroborated by Tilmann et al. (2008) and Contreras-Reyes et al. (2008a), occurs due to bending-related faulting at the outer rise offshore. This allows the percolation of sea water down to the upper oceanic mantle (Contreras-Reyes et al., 2008a). Poisson's ratios in the oceanic crust and upper mantle are lower onshore than they are offshore, showing the effect of the dehydration

of the oceanic plate during the subduction process. Below the oceanic Moho, which can be observed in Fig. 5.3, the Poisson's ratios values locally decrease to 0.22 - 0.26 and thus it is possible to observe the transition between the crust and the upper mantle of the downgoing plate. Unlike in the Poisson's ratio image of Contreras-Reyes et al. (2008b), where uniform Poisson's ratio values of ∼0.29 are observed in the serpentinized upper mantle, the Poisson's ratios onshore alternate between low values (0.22 - 0.26) and high values (0.27 - 0.28). The high Poisson's ratio values would be in agreement with the serpentinization of the subducting oceanic upper mantle.

Another interesting feature is the large region of high Poisson's ratio values between 0.3 and 0.31 at the centre of the model, between 12 and 18 km depth (see Figs. 5.1 and 5.3), with v_p/v_s values of 1.77 - 1.82 in the 2D model of Haberland et al. (2009). These high Poisson's ratios are associated with S-velocities of about 3.6 km s^{-1} and thus P-velocities between 6.7 - 7.0 km s^{-1}. Assuming that the velocities are unaffected by anisotropy (but see e.g. the discussions on this subject in Sections 2.1.2, 2.3.3 and 3.3.3), then searching in Christensen (1996) and the data bank of Stadtlander et al. (1999) (and references therein) reveals that this body is rich in plagioclase (∼70%), pyroxene (ortho-pyroxene) and amphibole. In particular, granulite, anorthosite, gabbro and partially serpentinized peridotite are possible rock types having the appropriate P- and S-velocities and thus appropriate Poisson's ratio at 12 - 18 km depth. Thus, these Poisson's ratio values can be explained by such rock types. Apart from anorthosite, the other three rock types are either found exposed in the western series (partially serpentinized peridotite, see Section 5.2) or their metamorphic equivalents are found exposed in the western series (gabbro) or they could be deeper crustal equivalents of rocks exposed in the western series (granulite; e.g. Hervé 1988; Glodny et al. 2008). If the region with high Poisson's ratio in the centre of the model between 12 and 18 km depth represents the extension at depth of the western series, then the Lanalhue Fault Zone (LFZ), which separates the western and the eastern series (Glodny et al., 2008), must dip towards the east or northeast. The inferred east-dipping LFZ can be observed in Fig. 5.3. In particular, if this body contains granulite, it must have migrated upwards after its formation, because this metamorphic rock-type is formed at a varying pressure of ∼3 - 14 kbar and high temperatures of ∼900°C, which are not the temperatures of the continental crust at ∼15 km depth (see e.g. Völker et al. 2011). In turn, this would be in agreement with the interpretation of Glodny et al. (2008), that the western series is a basally accreted metamorphic complex. Although intraplate events localized along the LFZ show recent seismic activity between 10 and 30 km depth and deep reaching near-vertical faults with a minor dip component (Haberland et al., 2006), evidence exists that favors an east-dipping fault from geological studies (Oyarzún et al. 1986; Burón 2003; Glodny et al. 2008) and from reflection seismics (Groß et al. 2008; Micksch 2008; see also Chapter 3). Thus, the geometry of the LFZ proposed here, coincides with the location of the eastern end of the high Poisson's ratio anomaly, interpreted as the extension at depth of the western series. The resulting seismic velocities above the plate interface in the continental crust of the Coastal Cordillera and the Central Valley in this part of the convergent margin could imply a lack of measurable amounts of present-day fluids, as their presence is not necessary to explain the Poisson's ratio and v_p/v_s values.

5.3.2 Hydration/dehydration processes in the subduction zone

Due to bending-related faulting at the outer rise offshore, the oceanic crust and upper mantle are hydrated (Contreras-Reyes et al., 2008a; Tilmann et al., 2008), explaining the high Poisson's ratios observed offshore (∼0.28 - 0.33 in the oceanic crust and ∼0.29 in the upper mantle; Contreras-Reyes et al. 2008b). Onshore, however, these values decrease. In particular, Poisson's ratios of 0.27 - 0.31 in the western part of the profile can be observed in the subducting oceanic crust until ∼78 km along the TIPTEQ profile and 0.25 - 0.27 east of ∼78 km. A study from Völker and Stipp (2015) could explain this observation. They ran thermal models to estimate the amount of water carried into the south-central Chile subduction zone and released by the oceanic crust and mantle for Nazca plate segments of different age. Considering a segment with an age of 25 million years appropriate for the study region (Sdrolias and Müller, 2006), the oceanic crust would lose ∼10% of the initial water content when it reaches the coast. Then the water content remains constant until ∼70 km from the coast (∼80 km in the TIPTEQ profile). East of this point it begins to release water again. At 38.25°S, at 70 km from the coast, the continental Moho is already above the subducting oceanic plate (see e.g. Figs. 2.21 and 5.3). This would support the idea of a continental crust above the subducting plate showing no indications of present-day measurable amounts of fluids in terms of seismic velocities. On the other hand, it supports the existence of serpentinization in the continental mantle wedge (see also Section 5.3.3) and the suggestion made by Haberland et al. (2009), that the plate interface acts as an impermeable seal down to ∼50 km depth (see Fig. 5.3). According to Völker and Stipp (2015), the release of water to the overlying continental mantle would not be much. However, if it has been happening over a long period of time it could add up to a significant process.

High resistivity (∼100 - 1000 Ωm) is typical of dry, cold crust and upper mantle, while resistivity lower than ∼10 Ωm indicates the presence of a fluid phase such as partial melt and/or aqueous fluids (Unsworth and Rondenay, 2012). The presence of water generally reduces the seismic velocity of rocks and minerals, affecting especially the S-velocities. For example, Thorwart et al. (2015) find evidence of fluid release and melts in the mantle beneath the volcanic arc at 39°S in the form of reduced S-velocities, coinciding with low resistivity observations. In the case of the Chilean subduction zone, resistivity values indicating a dry, cold continental crust are observed, with local exceptions (Kapinos et al., 2016). One such exception lies near the coast, between 10 - 25 km depth (see Fig. 5.3). This high conductivity anomaly coincides with low P- and S-velocities (Haberland et al., 2009; Ramos et al., 2016), with high reflectivity (Krawczyk et al. 2006; Groß et al. 2008; Micksch 2008; see also Chapter 3) and also with a portion of the oceanic crust where Völker and Stipp (2015) model fluids being released to the continental crust. It does not, however, coincide with high v_p/v_s ratios or Poisson's ratios and actually, a low v_p/v_s anomaly is observed (see Fig. 5.3). Such a conductor has been observed in other subduction zones (e.g. in northern Cascadia; Soyer and Unsworth 2006). It has been suggested that such a conductor could represent a region of sheared, imbricated crustal rocks above the subducting plate (Calvert, 2004). Another high conductivity anomaly in the crust obtained by Kapinos et al. (2016) is closely correlated to a zone of very low P- and S-velocities just beneath the surface, at ∼65 km along the TIPTEQ profile, reaching values as low as 2 and 1.7 km s^{-1} , respectively (Micksch, 2008; Ramos et al., 2016). This anomaly is located just east of the mapped LFZ and just above a steep, highly reflective event recovered by the pre-stack line-drawing migration (see Fig. 5.3). It is probably slightly offset from its true location and represents highly conductive and weathered sediments.

The conductor related to the continental mantle wedge in the 2D resistivity model is in the 3D model less conductive and apparently not completely connected to the mantle wedge (Kapinos et al., 2016). Due to this difference between both models, this conductor is not further taken into account in the integrative interpretation in this work.

Different studies have found an effective, although qualitative, correlation between high reflectivity and zones of peak dehydration and/or elevated pore pressure (Ide et al. 2007; Saffer and Tobin 2011 and references therein). The updip limit of the seismogenic zone is marked by evidence of anomalous porosity, low P-wave velocity and high reflectivity, suggesting elevated fluid pressure and extremely low effective stress, whereas the downdip limit is marked by high v_p/v_s ratios and reflectivity (Hyndman and Peacock, 2003; Ide et al., 2007). Observations of low S-velocities and high Poisson's ratios in the subducted oceanic crust in Japan and southern Mexico have been linked to zones of high pore fluid pressure at 25 - 50 km depth and between the locations of the 350 - 450°C isotherms (Saffer and Tobin, 2011). Although in theory, the width of the seismogenic zone should be controlled to first order by the plate temperatures, with 100 - 150°C for the updip and 350 - 450°C for the downdip limit (Völker et al., 2011), high seismicity is observed in different zones along the plate interface. One example is at depths greater than 40 km (Bohm 2004; Haberland et al. 2006; see also Fig. 5.3), which was the preferred continental Moho depth of Micksch (2008), and where the continental Moho abutted against the oceanic crust. Groß et al. (2008) propose that the subduction channel extending even beneath the continental mantle could explain the seismicity in this zone. On the other hand, high microseismicity fading at ∼33 km depth (see Fig. 5.3) is explained by Völker et al. (2011) as the subduction channel controlling the downdip seismic-aseismic transition, as the subducted and accreted (meta)sediments are much weaker than the surrounding rocks of the lower continental crust. Thus, the downdip limit of the seismogenic zone in southern Chile might be controlled by neither a particular crustal structure regime nor by the 450°C isotherm (which lies at ∼70 km depth, beneath the Central Valley in the thermal model of Völker et al. 2011), but by a combination of several factors. Additionally, Völker et al. (2011) propose that microseismicity might not control the updip and downdip limits. In this work, the interpreted width of the seismogenic zone is in agreement with the one suggested by Haberland et al. (2009), extending from ∼20 - 50 km depth (see yellow bar in Fig. 5.3). On the one hand, the updip seismic-aseismic transition coincides with high reflectivity, low P- and S-velocities and a zone of fluids being released from the oceanic crust. On the other hand, the interpreted downdip limit of the seismogenic zone coincides with the point where fluids are newly released from the oceanic crust and a high Poisson's ratio anomaly (see Fig. 5.3). Pre- and post-stack migration images show reflectivity increasing at ∼45 km depth (see Figs. 3.6 and 3.8) The S-reflectivity on the horizontal components at this depth is low in the EW component, but high in the NS component (see Figs. 3.10a and 3.10b). This suggests that probably the stacking velocities in this part of the profile favor the NS over the EW component, indicating once again the possibility of high-scale crustal anisotropy.

5.3.3 Updated reflectivity image of the southern Chile subduction zone

Fig. 5.3 shows the reflectivity of the Chilean subduction zone at 38.25°S, as interpreted from the results of this work. This is currently the most updated image of the study region. Black lines represent the reflectivity observed in the P-wave pre- and post-stack images. Red lines are the reflectivity recovered using the reverse

moveout correction in the pre-stack depth migration. Purple lines represent the reflectivity observed in the horizontal post-stack depth migrated components, but not in the vertical component. Finally, the dark yellow lines represent the post-stack P-reflectivity image using a deconvolution operator. For all of them, the density of the lines represents the intensity of the reflections, as recovered in the different reflectivity images.

In general, all the reflections are depth-migrated to about the same depths in every P- and S-reflectivity image in this work, with differences no larger than some kilometres, and coinciding with previous reflectivity images as well (Krawczyk and the SPOC Team, 2003; Micksch, 2008; Groß et al., 2008). In the case of the S-reflectivity images, it validates the synthetic stacking velocities used during the seismic processing. The oceanic crust is imaged with different intensity along the profile, with especially high intensity in the eastern part, below ∼45 km depth, attributed to a zone of high pore pressure and dehydration processes (see discussion in Section 5.3.2). An interpretation of the top of the oceanic crust was made using the events from the ISSA-2000 and TIPTEQ local seismicity catalogues along with the reflectivity images obtained in Chapter 3 (Ramos et al. 2016; C. Haberland, private communication). The interpreted geometry of the top of the slab and the oceanic Moho results in an oceanic crust with ∼7 - 8 km thickness, in agreement with previous reflectivity studies in the area (e.g. Rauch 2005; Krawczyk et al. 2006; Micksch 2008; Contreras-Reyes et al. 2008a).

The depth of the oceanic Moho in Fig. 5.3, which cannot be identified in the reflectivity images using the TIPTEQ NVR data, was taken from the SPOC wide-angle velocity model (Krawczyk et al., 2006) and corresponds to the depth where the P-velocity attains 8 km s^{-1} . The depth of the continental Moho used in this work for the integrative interpretation is the same as that in Micksch (2008), at ∼40 km depth, which is also the depth at which the P-wave velocities from the SPOC wide-angle model reach 7.2 km s^{-1}.

Aside from the plate interface, horizontal (steeply) dipping intracrustal reflectors could be imaged. This was an advantage of using different processing sequences and methods to depth migrate the TIPTEQ NVR data. Some of these reflectors (e.g. the Permo-Triassic accretionary wedge and the east-dipping LFZ), had already been well imaged. Some others were imaged in this work for the first time (see below). Recent seismic activity has been attributed to intracrustal reflectors in the study region (Bohm, 2004; Haberland et al., 2006).

5.3.3.1 New reflectivity events observed in the TIPTEQ profile

Reflectors that had not been previously imaged were found in this work (see the location of the listed reflectors and/or faults in Fig. 5.3):

- A M_L 5.2 event near the coast, followed by a large number of aftershocks are related to a NNW - SSE striking system of reverse faults close to the coast (Haberland et al., 2006). For the first time, a related steep reflector close to the coast was imaged (using the reverse moveout in the pre-stack depth migration). Although the reflector is slightly shifted from the location of the aftershocks, it is highly probable that this event represents one of these faults.

- The previously interpreted transparent zone in the uppermost 8 km depth range (Micksch, 2008; Groß et al., 2008) also shows coherent seismic events in the pre-stack depth migration and after using the

deconvolution operator in the post-stack processing. For example, an almost horizontal reflector can be observed at 5 km depth, extending from about 15 to almost 100 km along the TIPTEQ profile. This reflector coincides with an intra-crustal discontinuity (Tassara and Echaurren, 2012) and with S-velocities of 3.4 km s^{-1} (Ramos et al., 2016) and P-velocities of 6 km s^{-1} (Haberland et al., 2009).

- The reflector interpreted as the east-dipping Lanalhue Fault Zone (LFZ) is imaged up to ∼2 km depth in the P-wave post-stack migration image using a deconvolution operator. Additionally, a steep, highly reflective event is imaged in the pre-stack depth migration. If extrapolated to the surface however, this steep reflector does not coincide with the location of the LFZ. Possible explanations for this reflector are: i) that it is related to the highly weathered and conductive sediments just east of the LFZ. ii) It is a branch of the LFZ which has not yet been recognised at the surface or which does not reach the surface. A requirement for this to be possible would be that this reflector should merge with the LFZ at depth. iii) It is not a fault, but a material transition between the eastern series andvthe intrusive coastal batholith, as the location of this reflector coincides with the eastern end of the eastern series.

- The reflectivity of the Permo-Triassic accretionary wedge in the western part of the profile near the coast, although clearly imaged already (Krawczyk and the SPOC Team 2003; Micksch 2008; Groß et al. 2008 and in the P- and S-reflectivity images obtained in this work), has its – apparently steep – eastern boundary imaged up to ∼5 km depth in the pre-stack depth migrated image.

- Small reflectivity events in the first kilometres depth are observed almost along the whole profile in the P-reflectivity image from pre-stack depth migration. While some of them may not necessarily have a real meaning, others can be related to boundaries of sedimentary basins, as several such basins are observed in the form of very low velocity anomalies and high Poisson's ratios. One such example is located between 30 - 40 km.

- The steep east-dipping reflector observed in the EW S-reflectivity image, located between ∼95 - 105 km and 10 - 20 km depth has a geometry which is probably difficult to be resolved due to the low data fold at the eastern end of the profile. Its nature will probably remain uncertain unless a new seismic experiment retrieves additional data further east.

5.3.3.2 Continental Moho and serpentinized mantle wedge

The continental Moho is not observed in the TIPTEQ NVR data, probably due to the dewatering of the oceanic crust, which results in serpentinized forearc mantle material that reduces the velocity contrast between the continental crust and the mantle (Groß et al., 2008; Micksch, 2008). No method shows with complete certainty the continental Moho. The depth of the Moho from the gravity modelling of Alasonati-Tašárová (2007) depends on how the high density body in the continental wedge is interpreted. This high-density body overlaps a zone of reduced velocities and there is not a unique interpretation that explains the preferred modelled densities, as well as low P-velocities and high Poisson's ratios. It has been discussed whether this body represents exclusively sim20 - 30% hydrated mantle or if it is mafic crustal material, or a combination of both (Krawczyk et al., 2006). The Moho from the SPOC model is simply defined as the depth at which the P-velocities reach 7.2 km s^{-1} . It is located at 40 km depth, just east of the hypocentre

of the M_w 9.5 Valdivia earthquake, primarily studied by Cifuentes (1989) and relocated by Krawczyk and the SPOC Team (2003). However this interpretation alone of the continental Moho is not conclusive.

Haberland et al. (2009) observe low P-velocities of ∼7 km s^{-1} which would imply a 35% serpentinized mantle wedge, but low v_p/v_s values at the base of the forearc which do not support a large scale serpentinization of the mantle wedge. They interpret this zone as lower crust at depths greater than 35 km, formed by dragged crustal material and they also observed small ∼20% serpentinization clusters. These clusters of low and high Poisson's ratios in the continental mantle wedge can be observed in Figs. 5.1 and 5.3. In particular, a high Poisson's ratio anomaly is related to low P- and S-velocities and high conductivity, as well as high dehydration (see Fig. 5.3). On the other hand, the Poisson's ratios next to it can reach values as low as ∼0.23 (or v_p/v_s ratios of 1.69). Hacker and Abers (2012) suggest that unusually low v_p/v_s ratios of 1.65 (σ = 0.21), with S-velocities of ∼4.7 km s^{-1} can be an indicator of strongly anisotropic peridotites rather than unusual composition, due to a biased overestimation of S-velocities and/or underestimation of P-velocities, when compared to isotropic averages. Although the low Poisson's ratios in the continental mantle wedge are not as low, they are still lower than those for a typical subduction zone mantle wedge of 1.76 - 1.82 (Hacker and Abers, 2012). Similarly, the S-velocities are not as high as 4.7 km s^{-1} (S-velocities even lower than 4 km s^{-1} can be observed; see Fig. 2.21).

Thus, the interpretation for the continental mantle wedge in the study region of this work would be that velocities and Poisson's ratios are too low to be explained by purely serpentinized peridotite, although signs of serpentinization from different results are present in clusters. If anisotropy exists in the mantle wedge, it is not as strong as reported by Hacker and Abers (2012) (see also the discussion on the composition of the eastern profile from 1D synthetic velocities in Section 5.3.4).

5.3.3.3 The steep west-dipping reflector

As previously mentioned, the true nature of any reflector located at the eastern end of the profile or further away, although west-dipping will remain uncertain unless more seismic data are collected. This is valid for the steep, west-dipping reflector in the eastern part of the profile (110 - 155 km). When extrapolated to the surface, it coincides with the location of the seismically active, intra-arc, dextral strike-slip Liquiñe-Ofqui Fault Zone (LOFZ; location after Lange et al. 2008), although this is only valid considering the reflectivity of the post-stack P-reflectivity image. The pre-stack reflectivity image as well as the EW S-reflectivity image suggest an even steeper reflector. Steep, highly reflective events can be followed up to ∼8 km depth, although it is not certain that they correspond to the steep reflector.

Bloch et al. (2014) (and references therein) find a steep, highly reflective event in a high-resolution seismic profile in northern Chile at 21°S. They interpret it to be a rheological boundary between brittle to ductile continental crust, with ascending fluid paths, observed in a region with a high lateral contrast of seismic velocities, high seismic activity and temperature gradients. At 38.25°S however, no global or local seismic catalogue contains seismicity associated to this steep reflector, as it is located mainly in the aseismic continental mantle. Additionally, no existent P-velocity or v_p/v_s ratio model shows low velocity or v_p/v_s anomalies related to this reflector. A low Poisson's ratio anomaly and high P-velocities are observed just west of it in the 2D models of Haberland et al. (2009). However, this region lies at the limits of the validity of both models. No related strong temperature gradient is proposed either in this region (Völker et al.,

2011). It is thus unlikely that this reflector represents either an active fault or a rheological boundary similar to the one observed in northern Chile. Thus, the speculation of Groß et al. (2008), that this reflector is related to a possible ascent path for melts towards the volcanic arc is still the most reasonable hypothesis.

The process of fluids and/or melts ascending upwards through paths towards the volcanic arc, should occur over a period of several million years. In the last years, geodynamic models are being used to study the possible recycling of material in the continental mantle wedge due to the subduction, as the explanation for fluids ascending to the upper continental crust (S. Sobolev, private communication). Such a study in this region might prove to give an interesting insight on the possible nature of this reflector.

5.3.4 Composition of different layers in the continental crust, inferred from the reflectivity method

The synthetic 1D P- and S-velocities that produced synthetic seismograms with traveltimes and amplitude ratios of reflections that fit the observed ones were used to infer the composition and the rocks of different layers in the continental crust. In the western profile, at 33 km, three amplitude ratios (or, equivalently, layer boundaries) were modelled, i.e. the compositions of four layers were analysed: L_{1W}, between ~3 - 13 km depth; L_{2W}, between ~13 - 22 km; L_{3W}, between ~22 - 32 km and L_{4W} , below ~32 km. The last layer, L_{4W} corresponds to the oceanic crust. In the eastern profile, at 77 km, four reflections were modelled, but in this case only four layers were analysed, as the fifth layer, corresponding to the oceanic crust, lies deeper than 40 km. The laboratory samples used to produce the rocks and minerals catalogues used here were not exposed to such high pressures, so no information is available for this layer. L_{1E}, above the LFZ, lies between ~2 - 14 km depth. The rest of the layers are interpreted to be east-dipping. L_{2E}, between 14 - 23 km depth, is interpreted to be the same layer as L_{1W}. L_{3E} , between ~23 - 32 km, is interpreted to be the eastern equivalent of L_{2W} . Finally, L_{4E} , beneath ~32 km depth is interpreted to be the same layer as L_{3W} . The interpretation of the extension of each layer can be observed in Fig. 5.3.

L_{1E} is interpreted to be the intrusive, granitic coastal batholith (covered by sediments near the surface). The modelled P- and S-velocities for this layer were 5.94 and 3.38 km s^{-1} respectively, with the consequent Poisson's ratio (σ) of 0.26. Example rock types found in the catalogues, which fit the velocities and σ in this layer, are granite, diorite and gneiss.

L_{1W} reaches depths of about 23 km in the eastern part (as L_{2E}). This layer had low S-reflectivity in the reflectors related to the LFZ and the Permo-Triassic accretionary wedge and thus the modelled velocity contrasts corresponding to those reflectors were very small (0.04 - 0.08 km s^{-1}; see Figs. 4.5, 4.6, 4.8 and 4.9). In the western part, the modelled P- and S-velocities for this layer were 6.1 - 6.3 and 3.4 - 3.72 km s^{-1} respectively, with σ = 0.27, whilst in the eastern part, they were about 6.3 and 3.46 km s^{-1}, with σ = 0.28. This layer was interpreted to be rich in amphibolite in the western part and changing to metabasite as it dips to greater depths towards the east. Additionally, rocks such as gneiss and gabbro are found to match the modelled velocities. Gabbro in particular, is observed exclusively in the western series (Hervé, 1988; Ardiles, 2003; Glodny et al., 2008) and its presence in this layer would again support an east-dipping LFZ.

L_{2W} , or L_{3E} has in the western part modelled P- and S-velocities of 6.6 and 3.76 km s^{-1} respectively, with σ of about 0.26. In the eastern part, slight variations of the modelled velocities that still fit the

observations did not introduce great changes in the interpretation of the rocks in this layer. Such P- and S-velocities ranged in the eastern part between ∼6.6 - 7 and 3.7 - 3.85 km s^{-1} respectively, with σ ∼0.26 - 0.27. This layer was interpreted as also amphibolite-rich in the western part, changing into granulite as it dips towards the east. Once again, gneiss and gabbro could also be present in this layer.

L_{3W} is constrained below by the oceanic crust. The modelled P- and S-velocities are 6.72 and 3.85 km s^{-1}, with σ slightly smaller than 0.26. As this layer dips in the eastern direction, it becomes L_{4E} , which is interpreted to represent in part the continental mantle wedge. Modelled P- and S-velocities in this part of the profile are ∼6.9 - 7.3 and 4 - 4.2 km s^{-1}, resulting in σ ranging between values as low as 0.24 and 0.26. It is interesting that at 77 km a low Poisson's ratio anomaly reaching values as low as 0.23 can be identified in the continental mantle wedge (see Figs. 5.1 and 5.3). The interpretation of this layer in the western part is that it is more mafic than the overlying layers, with amphibolite starting to become granulite at these depths and with the presence of gabbro and serpentinized peridotite. As one moves to the east, gabbro could also be present in the eastern profile, but although the P- and S-velocities can be explained by 30% serpentinized peridotite (Hacker and Abers, 2004), which would be expected to be observed at these depths in a serpentinized mantle, the corresponding Poisson's ratios are not as low as the modelled ones. As suggested by Hacker and Abers (2012), anisotropy in peridotite in the continental mantle can explain that P- and/or S-velocities are biased with respect to their isotropic laboratory equivalents. Thus, the L_{4E} layer is interpreted to consist of two sub-layers, separated by the continental Moho (which is not identifiable in the observed reflectivity data): mafic, gabbro-rich lower crust, down to 40 km depth and above the continental mantle, which extends down to ∼45 km above the oceanic crust (reflectivity is observed starting at 42 km depth), with ∼20% anisotropic serpentinized peridotite, in agreement with Krawczyk et al. (2006) and Haberland et al. (2009) (see also the discussion in Section 5.3.3).

Finally, L_{4W}, representing the oceanic crust has modelled P- and S-velocities near the top of the layer of ∼6.9 and 3.9 km s^{-1} , with Poisson's ratios of about 0.27. The rock found in the catalogue to match these observations is gabbro, which is in agreement with Haberland et al. (2009), who additionally suggest metamorphosed mid-oceanic ridge basalt (MORB) as a possible explanation for the observations.

The interpreted composition and rocks of each layer are in agreement with geological observations at the surface along the western and eastern series (Hervé 1988; Ardiles 2003; Burón 2003; SERNAGEOMIN 2003; Glodny et al. 2005; Melnick and Echtler 2006; Glodny et al. 2008; see also Section 5.2). The presence of rocks observed in the western series at 77 km along the TIPTEQ profile supports once again an east-dipping LFZ.

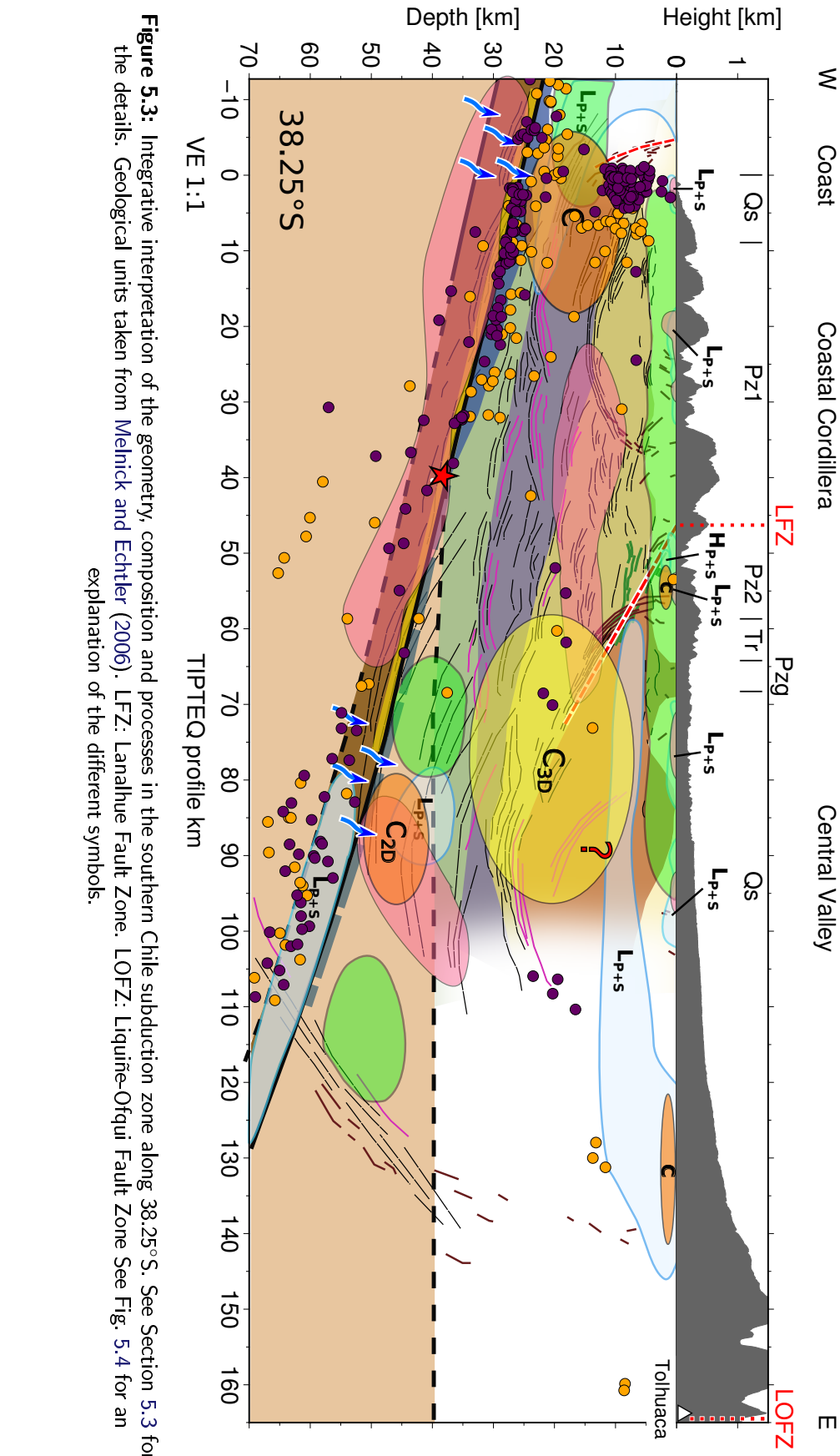

Figure 5.3: Integrative interpretation of the geometry, composition and processes in the southern Chile subduction zone along 38.25°S. See Section 5.3 for the details. Geological units taken from Melnick and Echtler (2006). LFZ: Lanalhue Fault Zone. LOFZ: Liquiñe-Ofqui Fault Zone See Fig. 5.4 for an explanation of the different symbols.

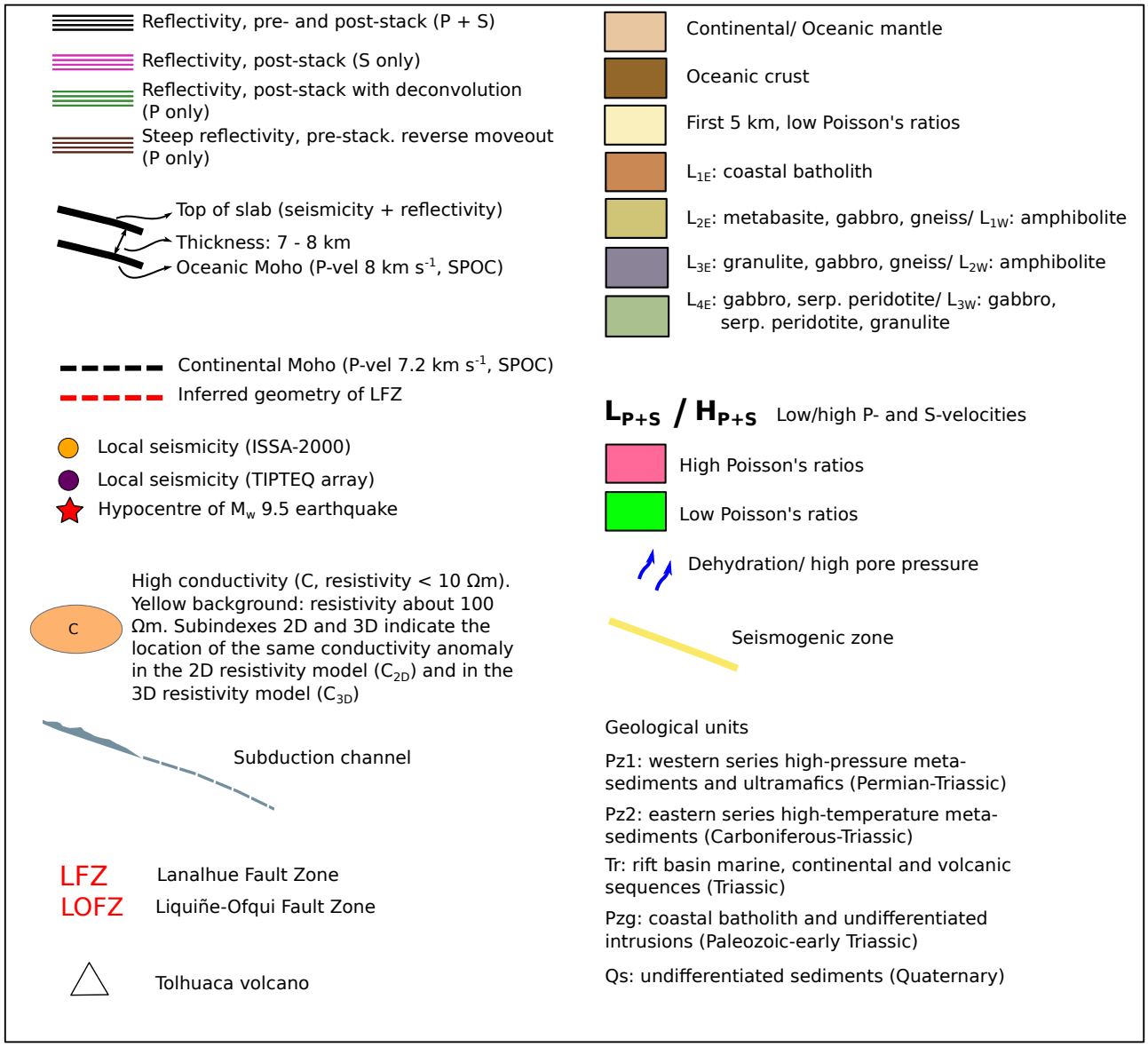

Figure 5.4: The different symbols used in Fig. 5.3. See Section 5.3 for more details.

Chapter 6

Conclusions and outlook

This work aimed to contribute to previous interdisciplinary research on the southern Chilean subduction zone at 38.25°S, to have a better understanding of the composition and processes of one of the most active seismic zones in the world. For this purpose, active and passive source data from the project TIPTEQ were used to obtain a S-wave velocity model and updated P-reflectivity and new S-reflectivity images. Additionally, synthetic seismograms were obtained for two 1D velocity-depth profiles, with reflections having arrival times and amplitude ratios similar to those observed in the different reflectivity images. The 1D synthetic P- and S-velocities producing such seismograms were used to interpret the rock types in the southern Chilean margin.

The use of high resolution active source seismic data allowed to obtain a S-velocity model able to resolve small-scale features, such as repeatedly observed near-surface low velocity anomalies with high Poisson's ratios. Such anomalies correspond to young (Quaternary), weathered sedimentary basins. The high frequency waves generated by the active sources, although easily recognizable using the appropriate bandpass filter, are quickly attenuated and in consequence their good resolution is only between 0 - 2 km depth. The S-velocity model obtained from noise tomography in the period range between 2.41 and 15.1 s using the TIPTEQ array data, resolves structures in the 2 - 20 km depth range. Such structures include an intracrustal discontinuity at 5 km depth and velocities in the central part of the profile, between $\sim$12 - 18 km depth, resulting in a high Poisson's ratio anomaly, interpreted as material that migrated upwards from the base of the continental crust, thus indicating basal accretion. This anomaly can be explained by rocks such as gabbro, serpentinized peridotite and granulite. The two velocity models were merged with an already existent S-wave velocity model from local earthquake tomography, which describes in good detail the plate interface. This merging procedure resulted in a 2D S-wave velocity model, in which transition between any two of the adjacent models is smooth and mostly without abrupt velocity changes, although it is worth mentioning the $\sim$0.4 km s^{-1} velocity difference in the centre of the profile at 20 km depth between the velocity model from noise tomography and the model from local earthquake tomography.

Updated reflectivity images of the southern Chilean subduction zone were obtained by using different depth-migration techniques on the vertical and both the horizontal components. The use of a deconvolution operator in the post-stack migrated P-reflectivity, although only quickly tested, helped to obtain additional information about the east-dipping Lanalhue Fault Zone (LFZ) closer to the surface. Additionally, the

new pre-stack line-drawing migration scheme using a reverse moveout allowed to image steep reflectors not imaged before. One example lies offshore, near the coast, where a steep intra-crustal reflector is related to high seismic activity. Another clear example, just above the LFZ, is discarded as being the continuation of this fault towards the surface, as it does not coincide with the surface location of the fault. Possible interpretations for this reflector are that it is related to nearby highly conductive, weathered sediments just beneath the surface, or that it is a branch of the LFZ not yet recognized at the surface or which does not reach the surface. Interestingly, this reflector coincides with the eastern end of the eastern series, so this highly reflective event could also represent the material transition between the eastern series and the neighbouring, intrusive, granitoid coastal batholith. Steep, small subsurface reflectors observed along the profile could be related to boundaries between sedimentary basins and the western/eastern series. Finally, steep reflectivity reaching very shallow depths ($\sim$8 km) towards the volcanic arc, could be related to the steep west-dipping reflector, which would then indicate a process that extends through the continental crust and mantle. No seismicity is related to this reflector, and the shallow steep reflectivity does not coincide with the surface location of the Liquiñe-Ofqui Fault Zone. Thus this event is either related to another, perhaps as yet unknown, fault or it is not related to a fault at all. The hypothesis that this steep reflector represents melts and/or fluids being released from the mantle to the continental crust still seems to be very attractive.

The input synthetic 1D P- and S-velocities, used to model reflections whose traveltimes and amplitude ratios (for each pair of reflections) fit the observed ones in the P- and S-reflectivity images in two 1D profiles, allowed a first order interpretation of the composition and rocks forming the different layers in the continental crust. Although the input velocity models producing synthetic seismograms that fit the observations are non-unique, they do not vary greatly and the velocity contrasts between adjacent layers are more or less constant. The rocks inferred from the velocities practically do not vary between the different derived velocity models. The modelled velocities and Poisson's ratios show east-dipping layers with compositions which are in agreement with geological observations along the TIPTEQ transect. They show that the layer above the LFZ has a granitic composition, and is probably formed by rocks such as granite, diorite and gneiss. It is thus interpreted as the subsurface, intrusive coastal batholith. The layer below reaches $\sim$22 km depth beneath the eastern 1D profile. It extends between $\sim$3 and $\sim$13 km depth under the western 1D profile. It is interpreted to represent the Permo-Triassic accretionary wedge. This layer is interpreted to be amphibolite-rich in the western part, transitioning as it dips down into metabasite in the eastern part, with gneiss and gabbro as other possible rocks to be found. An elevated Poisson's ratio body in this layer might represent granulite, gabbro or serpentinized peridotite. The layer below, extends down to $\sim$22 km depth below the western 1D profile and $\sim$32 km depth beneath the eastern 1D profile. It is also interpreted as being amphibolite-rich in the west, changing to granulite as it dips towards the eastern part, with the possible presence of gneiss and gabbro. The next layer, just above the oceanic crust probably consists of gabbro, granulite and serpentinized peridotite in the western part. The eastern part of this layer, just east of the location of the M_w 9.5 Valdivia earthquake, is interpreted to be divided into two sub-layers. The upper sub-layer, down to $\sim$40 km depth, probably represents mafic, gabbro-rich lower continental crust. The sub-layer below, overlying the oceanic crust is interpreted as the continental mantle wedge, with clusters that could indicate a $\sim$20% serpentinization of peridotite, but with Poisson's ratios

lower than expected, based on isotropic velocities derived from laboratory samples.

Based on the interpretation of the composition of the lower three layers above the oceanic crust, rocks of the western series are interpreted to be present also in the eastern part of the profile either directly (e.g. gabbro) or as (higher-grade) metamorphic equivalents (e.g. metabasite, granulite). If the LFZ was purely vertical, no rocks of the western series should be present in the eastern part of the profile, as field geology studies do not report their presence at the surface. Thus, an east-dipping LFZ is inferred from seismic velocities, in agreement with geological and reflectivity observations.

The presence of present-day fluids is not necessary to explain the derived seismic velocities and Poisson's ratios in the continental crust of the Coastal Cordillera and the Central Valley in this part of the Chilean margin. This could imply a lack of measurable amounts of present-day fluids according to the seismic velocities, above the plate interface in the continental crust in this part of the convergent margin. From the conductors modelled from magnetotelluric data in the continental crust, only the one near the coast should possibly be related to fluids in the continental crust. This high conductivity anomaly, although related to high P- and S-reflectivity, sporadically low P- and S- velocities and high pore pressure and dehydration, is not related to high Poisson's ratios. If fluids are present in this anomaly, they are not well detected by seismic velocities.

The geometry of the top of the slab at the plate interface is interpreted jointly using local seismicity and reflectivity images. The inferred thickness of the oceanic crust is $\sim$7 - 8 km, in agreement with previous observations. High Poisson's ratios in the oceanic crust offshore decrease towards the coast due to water release, until the oceanic crust loses about 10% of its initial water content as it reaches the coast. The amount of water remains constant until $\sim$80 km east of the coast, where the water release to the overlying continental mantle wedge starts. This would explain the presence of clusters of high Poisson's ratios, coinciding with low P- and S-velocities and possibly high conductivity in the continental mantle wedge, for example at 95 km along the profile. It also supports the interpretation of the composition of the continental crust without the need to call on the existence of present-day fluids.

The anisotropy topic was addressed several times in this work. The presence of a large-scale crustal – and upper-mantle – anisotropy would explain some observations, such as: traveltime differences of refracted S-waves in both horizontal components; S-velocity differences obtained using different sources, e.g. from the inversion of refracted vertically-polarized shear (S_V) and horizontally-polarized shear (S_H) arrivals versus S_V velocities inverted from dispersion measurements; stacking S-velocities resulting in certain reflectors that are better imaged in one horizontal component than in the other; inferred anisotropy in peridotite in the continental mantle wedge, observed as low Poisson's ratios not matching their isotropic laboratory equivalents. The presence of a large-scale crustal anisotropy has also been suggested by magnetotelluric studies in the region. Crustal anisotropy in the southern Chilean subduction zone is to date, however, not quantitatively studied. Such a research could possibly confirm or discard the hypotheses mentioned above.

The reflectivity in the eastern part of the profile and beyond should not be considered as conclusive due to the low data coverage in that part of the profile. For example, due to the field geometry, east-dipping reflectors in this zone are not recovered. The nature of the reflectors in this portion of the profile will probably remain uncertain until the TIPTEQ transect is extended further east.

Based on recent geodynamic modelling of subduction zones, the steep west-dipping reflector, believed to

cross through the continental crust and mantle, could be explained as fluids and/or melts escaping through the continental crust, towards the volcanic arc, due to material recycling in the continental mantle wedge as a result of the subduction process. A more detailed study would certainly yield interesting results that would help to better understand the possible processes that generate such a reflector, still enigmatic to date.

References

Aki, K. and Richards, P., 1980: Quantitative Seismology, vol. 2, WH Free, New York.

Alasonati-Tašárová, Z., 2007: Towards understanding the lithospheric structure of the southern Chilean subduction zone (36°S–42°S) and its role in the gravity field, *Geophys. J. Int.*, **170**(3), 995–1014, URL http://dx.doi.org/10.1111/j.1365-246X.2007.03466.x.

Ardiles, M., 2003: La Serie Occidental del basamento metamórfico, centro sur de la Cordillera de Nahuelbuta, Chile, área Quidico-Capitán Pastene. Petrografía, mesoestructura y análisis microtectónico, Memoria de título, Dept. de Ciencias de la Tierra. Universidad de Concepción, Chile.

Bauer, K., Ryberg, T., Fuis, G.S., and Lüth, S., 2013: Seismic imaging of the Waltham Canyon Fault, California: comparison of ray-theoretical and Fresnel volume prestack depth migration, *Bull. seism. Soc. Am.*, **103**(1), 340–352, URL http://dx.doi.org/10.1785/0120110338.

Bensen, G., Ritzwoller, M.H., Barmin, M.P., Levshin, A.L., Lin, F., Moschetti, M.P., Shapiro, N.M., and Yang, Y., 2007: Processing seismic ambient noise data to obtain reliable broad-band surface wave dispersion measurements, *Geophys. J. Int.*, **169**(3), 1239–1260, URL http://dx.doi.org/10.1111/j.1365-246X.2007.03374.x.

Beyreuther, M., Barsch, R., Krischer, L., Megies, T., Behr, Y., and Wassermann, J., 2010: ObsPy: a Python toolbox for seismology, *Seismol. Res. Lett.*, **81**(3), 530–533, URL http://dx.doi.org/10.1785/gssrl.81.3.530.

Bloch, W., Kummerow, J., Salazar, P., Wigger, P., and Shapiro, S.A., 2014: High-resolution image of the North Chilean subduction zone: seismicity, reflectivity and fluids, *Geophys. J. Int.*, **197**(3), 1744–1749, URL http://dx.doi.org/10.1093/gji/ggu084.

Bohm, M., 2004: 3D Lokalbebentomographie der südlichen Anden zwischen 36° und 40°S, Scientific technical report str04/15, Freie Universität Berlin and Deutsches GeoForschungsZentrum Potsdam, URL http://www.gfz-potsdam.de/bib/pub/str0415/0415.pdf.

Bracewell, R., 1999: Convolution Theorem, in: The Fourier Transform and Its Applications, 3rd ed, pp. 108–112, New York: McGraw-Hill.

Brasse, H., Kapinos, G., Li, Y., Mütschard, L., Soyer, W., and Eydam, D., 2009: Structural electrical anisotropy in the crust at the South-Central Chilean continental margin as inferred from geomagnetic

transfer functions, *Phys. Earth Planet. Inter.*, **173**(1), 7–16, URL http://dx.doi.org/10.1016/j.pepi.2008.10.01.

Bräuer, B., Ryberg, T., and Lindeque, L.S., 2007: Shallow seismic velocity structure of the Karoo Basin, South Africa, *S. Afr. J. Geol.*, **110**(2-3), 439–448, URL http://dx.doi.org/10.2113/gssajg.110.2-3.439.

Burón, P., 2003: Petrografía, estructuras y microtectónica del área de contacto entre las series metamórficas del basamento Paleozoico entre los 38°08' y 38°21'S, Cordillera de Nahuelbuta, Chile., Memoria de título, Dept. de Ciencias de la Tierra. Universidad de Concepción, Chile.

Calvert, A., 2004: Seismic reflection imaging of two megathrust shear zones in the northern Cascadia subduction zone, *Nature*, **428**(6979), 163–167, URL http://dx.doi.org/10.1038/nature0237.

Campillo, M. and Paul, A., 2003: Long-range correlations in the diffuse seismic coda, *Science*, **299**(5606), 547–549, URL http://dx.doi.org/10.1126/science.1078551.

Červený, V., Molotkov, I.A., and Pšenčík, I., 1977: Ray Method in Seismology, Univerzita Karlova, Prague.

Choy, G., Cormier, V.F., Kind, R., Müller, G., and Richards, P.G., 1980: A comparison of synthetic seismograms of core phases generated by the full wave theory and by the reflectivity method, *Geophys. J Int.*, **61**(1), 21–39, URL http://dx.doi.org/10.1111/j.1365-246X.1980.tb04301.x.

Christensen, N., 1996: Poisson's ratio and crustal seismology, *J. geophys. Res.*, **101**(B2), 3139–3156, URL http://dx.doi.org/10.1029/95JB03446.

Cifuentes, I., 1989: The 1960 Chilean earthquakes, *J. geophys. Res.*, **94**(B1), 665–680, URL http://dx.doi.org/10.1029/JB094iB01p00665.

Contreras-Reyes, E., Grevemeyer, I., Flüh, E.R., and Reichert, C., 2008a: Upper lithospheric structure of the subduction zone offshore of southern Arauco peninsula, Chile, at ∼38°S, *J. geophys. Res.*, **113**(B7), B07 303, URL http://dx.doi.org/10.1029/2007JB005569.

Contreras-Reyes, E., Grevemeyer, I., Flüh, E.R., Scherwath, M., and Bialas, J., 2008b: Effect of trench-outer rise bending-related faulting on seismic Poisson's ratio and mantle anisotropy: a case study offshore of Southern Central Chile, *Geophys. J. Int.*, **173**(1), 142–156, URL http://dx.doi.org/10.1111/j.1365-246X.2008.03716.x.

Cooley, J. and Tukey, J., 1965: An algorithm for the machine computation of complex Fourier series, *Math. Comp.*, **19**(90), 297–301, URL http://www.jstor.org/stable/2003354?seq=1.

Davies, J., 2013: Global map of solid Earth surface heat flow, *Geochem. Geophys. Geosyst.*, **14**(10), 4608–4622, URL http://dx.doi.org/10.1002/ggge.20271.

Deckart, K., Hervé, F., Fanning, C.M., Ramírez, V., Calderón, M., and Godoy, E., 2014: U-Pb geochronology and Hf-O isotopes of zircons from the Pennsylvanian Coastal Batholith, South-Central Chile, *Andean Geol.*, **41**(1), 49–82, URL http://dx.doi.org/10.5027/andgeoV41n1-a03.

Dohr, G., 1985a: Development of a procedure for the exploration of areas with poor reflections by the combined application of different geophysical methods, taking the North–West German basin as an example, in: New Technologies for the Exploration and Exploitation of Oil and Gas Resources, edited by De Bouw, R., Millich, E., Joulia, J., and Van Asselt, D., vol. 1, pp. 62–69, Graham and Trotman.

Dohr, G., 1985b: Seismic Shear Waves: Theory, vol. 15A, Geophysical Press.

Dziewonski, A., Bloch, S., and Landisman, M., 1969: A technique for the analysis of transient seismic signals, *Bull. seism. Soc. Am.*, **59**(1), 427–444, URL http://www.bssaonline.org/content/59/1/427.short.

EUROBRIDGE Seismic Working Group, 1999: Seismic velocity structure across the Fennoscandia-Sarmatia suture of the East European Craton beneath the EUROBRIDGE profile through Lithuania and Belarus, *Tectonophysics*, **314**(1), 193–217, URL http://dx.doi.org/10.1016/S0040-1951(99)00244-9.

Feng, M. and An, M., 2010: Lithospheric structure of the Chinese mainland determined from joint inversion of regional and teleseismic Rayleigh-wave group velocities, *J. geophys. Res.*, **115**(B6), B06 317, URL http://dx.doi.org/10.1029/2008JB005787.

Forsyth, D., Webb, S.C., Dorman, L.M., and Shen, Y., 1998: Phase velocities of Rayleigh waves in the MELT experiment on the East Pacific Rise, *Science*, **280**(5367), 1235–1238, URL http://dx.doi.org/10.1126/science.280.5367.1235.

Fuchs, K. and Müller, G., 1971: Computation of synthetic seismograms with the reflectivity method and comparison with observations, *Geophys. J Int.*, **23**(4), 417–433, URL http://dx.doi.org/10.1111/j.1365-246X.1971.tb01834.x.

Glodny, J., Lohrmann, J., Echtler, H., Gräfe, K., Seifert, W., Collao, S., and Figueroa, O., 2005: Internal dynamics of a paleoaccretionary wedge: insights from combined isotope tectonochronology and sandbox modelling of the South-Central Chilean forearc, *Earth Planet. Sc. Lett.*, **231**(1), 23–39, URL http://dx.doi.org/10.1016/j.epsl.2004.12.014.

Glodny, J., Echtler, H., Collao, S., Ardiles, M., Burón, P., and Figueroa, O., 2008: Differential Late Paleozoic active margin evolution in South-Central Chile (37°S–40°S) – the Lanalhue Fault Zone, *J. South Am. Earth Sci.*, **26**(4), 397–411, URL http://dx.doi.org/10.1016/j.jsames.2008.06.001.

Groß, K., Micksch, U., and TIPTEQ research group, 2008: The reflection seismic survey of project TIPTEQ – the inventory of the Chilean subduction zone at 38°S, *Geophys. J Int.*, **172**(2), 565–571, URL http://dx.doi.org/10.1111/j.1365-246X.2007.03680.x.

Haberland, C., Rietbrock, A., Lange, D., Bataille, K., and Hoffmann, S., 2006: Interaction between forearc and oceanic plate at the southcentral Chilean margin as seen in local seismic data, *Geophys. Res. Lett.*, **33**(23), L23 302, URL http://dx.doi.org/10.1029/2006GL028189.

Haberland, C., Rietbrock, A., Lange, D., Bataille, K., and Dahm, T., 2009: Structure of the seismogenic zone of the south–central Chilean margin revealed by local earthquake travel–time tomography, *J. geophys. Res.*, **114**(B1), B01 317, URL http://dx.doi.org/10.1029/2008JB005802.

Hacker, B. and Abers, G., 2004: Subduction Factory 3: An Excel worksheet and macro for calculating the densities, seismic wave speeds, and H_2O contents of minerals and rocks at pressure and temperature, *Geochem. Geophys. Geosyst.*, **5**(1), URL http://dx.doi.org/10.1029/2003GC00061.

Hacker, B. and Abers, G., 2012: Subduction Factory 5: Unusually low Poisson's ratios in subduction zones from elastic anisotropy of peridotite, *J. geophys. Res.*, **117**(B6), B06 308, URL http://dx.doi.org/10.1029/2012JB009187.

Harmon, N., Salas De La Cruz, M., Rychert, C.A., Abers, G., and Fischer, K., 2013: Crustal and mantle shear velocity structure of Costa Rica and Nicaragua from ambient noise and teleseismic Rayleigh wave tomography, *Geophys. J. Int.*, **195**(2), 1300–1313, URL http://dx.doi.org/10.1093/gji/ggt309.

Herrmann, R., 1978: Computer Programs in Earthquake Seismology, vol. 1: General Programs, St. Louis University, Department of Earth and Atmospheric Sciences, St. Louis, Missouri.

Herrmann, R., 2013: Computer programs in seismology: An evolving tool for instruction and research, *Seism. Res. Lettr.*, **84**(6), 1081–1088, URL http://dx.doi.org/10.1785/0220110096.

Hervé, F., 1988: Late Paleozoic subduction and accretion in Southern Chile, *Episodes*, **11**(3), 183–188.

Hicks, S., Nippress, S.E., and Rietbrock, A., 2012: Sub-slab mantle anisotropy beneath south-central Chile, *Earth Planet Sc. Lett.*, **357**, 203–213, URL http://dx.doi.org/10.1016/j.epsl.2012.09.017.

Hyndman, R. and Peacock, S., 2003: Serpentinization of the forearc mantle, *Earth planet. Sci. Lett.*, **212**(3–4), 417–432, URL http://dx.doi.org/10.1016/S0012-821X(03)00263-2.

Ide, S., Beroza, G.C., Shelly, D.R., and Uchide, T., 2007: A scaling law for slow earthquakes, *Nature*, **447**(7140), 76–79, URL http://dx.doi.org/10.1038/nature057.

IRIS, Incorporated Research Institutions for Seismology, 2008: MiniSEED data format, URL http://ds.iris.edu/ds/nodes/dmc/data/formats/miniseed/.

Jordan, T., Burns, W.M., Veiga, R., Pángaro, F., Copeland, P., Kelley, S., and Mpodozis, C., 2001: Extension and basin formation in the southern Andes caused by increased convergence rate: A mid-Cenozoic trigger for the Andes, *Tectonics*, **20**(3), 308–324, URL http://dx.doi.org/10.1029/1999TC001181.

Kanamori, H., 1977: The energy release in great earthquakes, *J. geophys. Res.*, **82**(20), 2981–2987, URL http://dx.doi.org/10.1029/JB082i020p02981.

Kapinos, G., Montahaei, M., Meqbel, N., and Brasse, H., 2016: Three-dimensional electrical resistivity image of the South-Central Chilean subduction zone, *Tectonophysics*, **666**(1), 76–89, URL http://dx.doi.org/10.1016/j.tecto.2015.10.016.

Karplus, M., Zhao, W., Klemperer, S.L., Wu, Z., Mechie, J., Shi, D., Brown, L.D., and Chen, C., 2011: Injection of Tibetan crust beneath the south Qaidam Basin: Evidence from INDEPTH IV wide-angle seismic data, *J. geophys. Res.*, **116**(B7), B07 301, URL http://dx.doi.org/10.1029/2010JB007911.

Kearey, P., Brooks, M., and Hill, I., 2013: An Introduction to Geophysical Exploration, John Wiley & Sons., third edn.

Kendrick, E., Bevis, M., Smalley, R., Brooks, B., Barriga Vargas, R., Lauría, E., and Soto Fortes, L.P., 2003: The Nazca–South America Euler vector and its rate of change, *J. South Am. Earth Sci.*, **16**(2), 125–131, URL http://dx.doi.org/10.1016/S0895-9811(03)00028-2.

Kennett, B., 1983: Seismic Wave Propagation in Stratified Media, Cambridge University Press, URL http://press.anu.edu.au?p=63081.

Korenaga, J., Holbrook, W.S., Kent, G.M., Kelemen, P.B., Detrick, R.S., Larsen, H.-C., Hopper, J.R., and Dahl-Jensen, T., 2000: Crustal structure of the southeast Greenland margin from joint refraction and reflection seismic tomography, *J. Geophys. Res.*, **105**(B9), 21 591–21 614, URL http://dx.doi.org/10.1029/2000JB900188.

Krawczyk, C. and the SPOC Team, 2003: Amphibious seismic survey images plate interface at 1960 Chile earthquake, *EOS, Trans. Am. geophys. Un.*, **84**(32), 301–305, URL http://dx.doi.org/10.1029/2003EO320001.

Krawczyk, C., Mechie, J., Lüth, S., Tašárová, Z., Wigger, P., Stiller, M., Brasse, H., Echtler, H., Araneda, M., and Bataille, K., 2006: Geophysical signatures and active tectonics at the south-central Chilean margin, in: The Andes – Active Subduction Orogeny. Frontiers in Earth Science, edited by Oncken, O., Chong, G., Franz, G., Giese, P., Götze, H., Ramos, V., Strecker, M., and Wigger, P., vol. 1, chap. 8, pp. 171–192, Springer Verlag, Berlin.

Lange, D., Cembrano, J., Rietbrock, A., Haberland, C., Dahm, T., and Bataille, K., 2008: First seismic record for intra-arc strike-slip tectonics along the Liquiñe-Ofqui fault zone at the obliquely convergent plate margin of the southern Andes, *Tectonophysics*, **455**(1), 14–24, URL http://dx.doi.org/10.1016/j.tecto.2008.04.014.

Levander, A., Zelt, C.A., and Symes, W.W., 2007: Crust and Lithospheric Structure – Active Source Studies of Crust and Lithospheric Structure, in: A Treatise on Geophysics, edited by Dziewonski, A. and Romanowicz, B., vol. 1, chap. 1.08, pp. 247–288, Elsevier.

Lin, F., Ritzwoller, M. H., Townend, J., Bannister, S., and Savage, M. K., 2007: Ambient noise Rayleigh wave tomography of New Zealand, *Geophys. J. Int.*, **170**(2), 649–666, URL http://dx.doi.org/10.1111/j.1365-246X.2007.03414.x.

Lüth, S., Wigger, P., and ISSA Research Group, 2003: A crustal model along 39°S from a seismic refraction profile – ISSA 2000, *Revista Geológica de Chile*, **30**(1), 83–101, URL http://dx.doi.org/10.4067/S0716-02082003000100006.

Lutter, W., Nowack, R., and Braile, L., 1990: Seismic imaging of upper crustal structure using travel times from the PASSCAL Ouachita experiment, *J. geophys. Res.*, **95**(B4), 4621–4631, URL http://dx.doi.org/10.1029/jb095ib04p04621.

Ma, Y., Loures, L., and Margrave, G.F., 2004: Seismic modeling with the reflectivity method, *CREWES Research Report*, **16**, URL http://crewes.org/ForOurSponsors/ResearchReports/2004/2004-13.pdf.

Mallick, S. and Frazer, L., 1987: Practical aspects of reflectivity modelling, *Geophysics*, **52**(10), 1355–1364, URL https://doi.org/10.1190/1.1442248.

Mechie, J., Abu-Ayyash, K., Ben-Avraham, Z., El-Kelani, R., Qabbani, I., Weber, M., and DESIRE Group, 2009: Crustal structure of the southern Dead Sea basin derived from project DESIRE wide-angle seismic data, *Geophys. J Int.*, **178**(1), 457–478, URL http://dx.doi.org/10.1111/j.1365-246X.2009.04161.x.

Mechie, J., Yuan, X., Schurr, B., Schneider, F., Sippl, C., Ratschbacher, L., Minaev, V., Gadoev, M., Oimahmadov, I., Abdybachaev, U., Moldobekov, B., Orunbaev, S., and Negmatullaev, S., 2012a: Crustal and uppermost mantle velocity structure along a profile across the Pamir and southern Tien Shan as derived from project TIPAGE wide-angle seismic data, *Geophys. J Int.*, **188**(2), 385–407, URL http://dx.doi.org/10.1111/j.1365-246X.2011.05278.x.

Mechie, J., Zhao, W., Karplus, M.S., Wu, Z., Meissner, R., Shi, D., Klemperer, S.L., Su, H., Kind, R., Xue, G., and Brown, L.D., 2012b: Crustal shear (S) velocity and Poisson's ratio structure along the INDEPTH IV profile in northeast Tibet as derived from wide-angle seismic data, *Geophys. J Int.*, **191**(2), 369–384, URL http://dx.doi.org/10.1111/j.1365-246X.2012.05616.x.

Melnick, D. and Echtler, H., 2006: Morphotectonic and geologic digital map compilations of the south-central Andes (36–43°S), in: The Andes – Active Subduction Orogeny. Frontiers in Earth Science, edited by Oncken, O., Chong, G., Franz, G., Giese, P., Götze, H., Ramos, V., Strecker, M., and Wigger, P., vol. 1, chap. 30, pp. 565–568, Springer Verlag.

Micksch, U., 2008: The Chilean subduction zone at 38.2°S: New geophysical images derived from seismic reflection data of project TIPTEQ; implications for the subduction channel and the seismogenic coupling zone, Scientific technical report str08/14, Freie Universität Berlin and Deutsches GeoForschungsZentrum Potsdam, URL http://www.gfz-potsdam.de/bib/pub/str0814/0814.pdf.

Nolet, G., 2008: A Breviary of Seismic Tomography: Imaging the Interior of the Earth and Sun, Cambridge University Press, New York.

Oyarzún, R., Clemmey, H., and Collao, S., 1986: Geologic and metallogenic aspects concerning the Nahuelbuta mountains banded iron formation, Chile, *Miner. Deposita*, **21**(3), 244–250.

Podvin, P. and Lecomte, I., 1991: Finite difference computation of travel times in very contrasted velocity models: a massive parallel approach and its associated tools, *Geophys. J. Int.*, **105**(1), 271–284, URL http://dx.doi.org/10.1111/j.1365-246X.1991.tb03461.x.

Ramos, C., Mechie, J., and Feng, M., 2016: Shear wave velocity and Poisson's ratio models across the southern Chile convergent margin at 38°15'S., *Geophys. J. Int.*, **204**(3), 1620–1635, URL http://dx.doi.org/10.1093/gji/ggv541.

Rauch, K., 2005: Cyclicity of Peru-Chile trench sediments between 36° and 38°S: a footprint of paleoclimatic variations?, *Geophys. Res. Lett.*, **32**(8), URL http://dx.doi.org/10.1029/2004GL022196.

Rietbrock, A., Haberland, C., Bataille, K., Dahm, T., and Oncken, O., 2005: Studying the seismogenic coupling zone with a passive seismic array, *EOS, Trans. Am. geophys. Un.*, **86**(32), 293–297, URL http://dx.doi.org/10.1029/2005EO320001.

Saffer, D. and Tobin, H., 2011: Hydrogeology and mechanics of subduction zone forearcs: Fluid flow and pore pressure, *Annu. Rev. Earth Planet. Sci.*, **39**, 157–186, URL http://dx.doi.org/10.1146/annurev-earth-040610-133408.

Sandmeier, K., 1984: Veränderung und Erweiterung des Reflektivitäts programms zur Berechnung synthetischer Seismogramme, Ph.D. thesis, University of Karlsruhe.

Saygin, E. and Kennett, B., 2010: Ambient seismic noise tomography of Australian continent, *Tectonophysics*, **481**(1), 116–125, URL http://dx.doi.org/10.1016/j.tecto.2008.11.013.

Scherwath, M., Flüh, E.R., Grevemeyer, I., Tilmann, F., Contreras-Reyes, E., and Weinrebe, W., 2006: Investigating subduction zone processes in Chile, *EOS, Trans. Am. geophys. Un.*, **87**(27), 265–272, URL http://dx.doi.org/10.1029/2006EO270001.

Scherwath, M., Contreras-Reyes, E., Flüh, E.R., Grevemeyer, I., Krabbenhöft, A., Papenberg, C., Petersen, C.J., and Weinrebe, R.W., 2009: Deep lithospheric structures along the southern central Chile margin from wide-angle P-wave modelling, *Geophys. J Int.*, **179**(1), 579–600, URL http://dx.doi.org/10.1111/j.1365-246X.2009.04298.x.

Schneider, W., Ranzinger, K., Balch, A., and Kruse, C., 1992: A dynamic programming approach to first arrival travel-time computation in media with arbitrarily distributed velocities, *Geophysics*, **57**(1), 39–50, URL http://dx.doi.org/10.1190/1.1443187.

Sdrolias, M. and Müller, R. D., 2006: Controls on back-arc basin formation, *Geochem. Geophys. Geosyst.*, **7**(4), Q04016, URL http://dx.doi.org/10.1029/2005GC001090.

SEG, The Society of Exploration Geophysicists, 2002: SEG-y rev 1, URL http://www.seg.org/Portals/0/SEG/News%20and%20Resources/Technical%20Standards/seg_y_rev1.pdf.

Sens-Schönfelder, C., Flores-Estrella, H., Gassenmeier, M., Korn, M., Köllner, F., Milkereit, C., Niederleithinger, E., Parolai, S., Pilz, M., Pomponi, E., Schuck, A., Thiemann, K., and Völkel, J., 2014: MIIC: Monitoring and Imaging Based on Interferometric Concepts, in: Tomography of the Earth's Crust: From Geophysical Sounding to Real-Time Monitoring, edited by Weber, M. and Münch, U., pp. 43–61, Springer International Publishing, URL http://dx.doi.org/10.1007/978-3-319-04205-3_3.

SERNAGEOMIN, 2003: Mapa geológico de Chile, versión digital No. 4, Servicio Nacional de Geología y Minería, Santiago de Chile.

Shapiro, N. and Campillo, M., 2004: Emergence of broadband Rayleigh waves from correlations of the ambient seismic noise, *Geophys. Res. Lett.*, **31**(7), L07 614, URL http://dx.doi.org/10.1029/2004GL019491.

Snieder, E., 2004: Extracting the Green's function from the correlation of coda waves: A derivation based on stationary phase, *Phys. Rev. E*, **69**(4), 046 610, URL http://dx.doi.org/10.1103/PhysRevE.69.046610.

Soyer, W. and Unsworth, M., 2006: Deep electrical structure of the northern Cascadia (British Columbia, Canada) subduction zone: Implications for the distribution of fluids, *Geology*, **34**(1), 53–56, URL http://dx.doi.org/10.1130/G21951.1.

Stadtlander, R., Mechie, J., and Schulze, A., 1999: Deep structure of the southern Ural mountains as derived from wide-angle seismic data, *Geophys. J. Int.*, **137**(2), 501–515, URL http://dx.doi.org/10.1046/j.1365-246X.1999.00794.x.

Stein, S. and Wysession, M., 2009: An Introduction to Seismology, Earthquakes, and Earth Structure, John Wiley & Sons.

Tarantola, A., 1987: Inverse problem theory: Methods for data fitting and parameter estimation, Elsevier, Amsterdam.

Tassara, A. and Echaurren, A., 2012: Anatomy of the Andean subduction zone: three-dimensional density model upgraded and compared against global-scale models, *Geophys. J. Int.*, **189**(1), 161–168, URL http://dx.doi.org/10.1111/j.1365-246X.2012.05397.x.

Thorwart, M., Dzierma, Y., Lieser, K., Buhs, H., and Rabbel, W., 2015: Shear-wave velocity structure of the Chilean subduction zone (39–40°S) based on Rayleigh wave dispersion: evidence of fluid release and melts in the mantle beneath the Villarrica volcano, *Geological Society, London, Special Publications*, **410**(1), 59–70, URL http://dx.doi.org/10.1144/SP410.9.

Tilmann, F., Grevemeyer, I., Flüh, E.R., Dahm, T., and Gossler, J., 2008: Seismicity in the outer rise offshore southern Chile: indication of fluid effects in crust and mantle, *Earth planet. Sci. Lett.*, **269**(1–2), 41–55, URL http://dx.doi.org/10.1016/j.epsl.2008.01.044.

Topping, J., 1972: Errors of Observation and their Treatment, Chapman & Hall, London, 4 edn.

Unsworth, M. and Rondenay, S., 2012: Mapping the distribution of fluids in the crust and lithospheric mantle utilizing geophysical methods, in: Metasomatism and the Chemical Transformation of Rock, chap. 13, pp. 535–598, Springer Berlin Heidelberg, URL http://dx.doi.org/10.1007/978-3-642-28394-9_13.

Van Wagoner, T., Crosson, R.S., Symons, N.P., Medema, G.F., Creager, K.C., and Brocher, T., 2002: Crustal structure and relocated earthquakes in the Puget Lowland, Washington from high resolution

seismic tomography, *J. Geophys. Res.*, **107**(B12), 22–1–22–23, URL http://dx.doi.org/10.1029/2001JB000710.

Vidale, J., 1988: Finite-difference calculation of travel times, *Bull. seism. Soc. Am.*, **78**(6), 2062–2076, URL http://www.bssaonline.org/content/78/6/2062.short.

Völker, D. and Stipp, M., 2015: Water input and water release from the subducting Nazca Plate along southern Central Chile (33°S–46°S), *Geochem. Geophys. Geosyst.*, **16**(6), 1825–1847, URL http://dx.doi.org/10.1002/2015GC005766.

Völker, D., Grevemeyer, I., Stipp, M., Wang, K., and He, J., 2011: Thermal control of the seismogenic zone of southern central Chile, *J. geophys. Res.*, **116**(B10), B10 305, URL http://dx.doi.org/10.1029/2011JB008247.

Wapenaar, K., 2004: Retrieving the elastodynamic Green's function of an arbitrary inhomogeneous medium by cross correlation, *Phys. Rev. Lett.*, **93**(25), 254 301, URL http://dx.doi.org/10.1103/PhysRevLett.93.254301.

Weaver, R. and Lobkis, O., 2001: Ultrasonics without a Source: thermal fluctuation correlations at MHz frequencies, *Phys. Rev. Lett.*, **87**(13), 134 301, URL http://dx.doi.org/10.1103/PhysRevLett.87.134301.

Weber, M., Abu-Ayyash, K., Abueladas, A., Agnon, A., Al-Amoush, H., Babeyko, A., Bartov, Y., Baumann, M., Ben-Avraham, Z., Bock, G., Bribach, J., El-Kelani, R., Förster, A., Förster, H.-J., Frieslander, U., Garfunkel, Z., Grunewald, S., Götze, H.-J., Haak, V., Haberland, C., Hassouneh, M., Helwig, S., Hofstetter, A., Jäckel, K.-H., Kesten, D., Kind, R., Maercklin, N., Mechie, J., Mohsen, A., Neubauer, F.M., Oberhänsli, R., Qabbani, I., Ritter, O., Rümpker, G., Rybakov, M., Ryberg, T., Scherbaum, F., Schmidt, J., Schulze, A., Sobolev, S., Stiller, M., Thoss, H., Weckmann, U., and Wylegalla, K., 2004: The crustal structure of the Dead Sea Transform, *Geophys. J Int.*, **156**(3), 655–681, URL http://dx.doi.org/10.1111/j.1365-246X.2004.02143.x.

Wessel, P., Smith, W. H.F., Scharroo, R., Luis, J., and Wobbe, F., 2013: Generic Mapping Tools: Improved version released, *EOS, Trans. Am. geophys. Un.*, **94**(45), 409–410, URL http://dx.doi.org/10.1002/2013EO450001.

Yang, T., Liu, F., Harmon, N., Le, K.P., Gu, S., and Xue, M., 2015: Lithospheric structure beneath Indochina block from Rayleigh wave phase velocity tomography, *Geophys. J. Int.*, **200**(3), 1582–1595, URL http://dx.doi.org/10.1093/gji/ggu488.

Yang, Y. and Forsyth, D., 2006: Regional tomographic inversion of the amplitude and phase of Rayleigh waves with 2-D sensitivity kernels, *Geophys. J. Int.*, **166**(3), 1148–1160, URL http://dx.doi.org/10.1111/j.1365-246X.2006.02972.x.

Yilmaz, Ö., 2001: Seismic Data Analysis: Processing, Inversion and Interpretation of Seismic Data, vol. I and II, Society of Exploration Geophysicists, Tulsa, OK.

Zandt, G. and Ammon, C., 1995: Continental crust composition constrained by measurements of crustal Poisson's ratio, *Nature*, **374**(6518), 152–154, URL http://dx.doi.org/10.1038/374152a0.

Zelt, C., 1998: Lateral velocity resolution from three-dimensional seismic refraction data, *Geophys. J. Int.*, **135**(3), 1101–1112, URL http://dx.doi.org/10.1046/j.1365-246X.1998.00695.x.

Zelt, C. and Barton, P., 1998: Three-dimensional seismic refraction tomography: a comparison of two methods applied to data from the Faeroe Basin, *J. geophys. Res.*, **103**(B4), 7187–7210, URL http://dx.doi.org/10.1029/97JB03536.

Zelt, C. and Smith, R., 1992: Seismic travel-time inversion for 2-D crustal velocity structure, *Geophys. J. Int.*, **108**(1), 16–34, URL http://dx.doi.org/10.1111/j.1365-246x.1992.tb00836.x.

Zhao, W., Mechie, J., Brown, L.D., Guo, J., Haines, S., Hearn, T., Klemperer, S.L., Ma, Y.S., Meissner, R., Nelson, K.D., Ni, J.F., Pananont, P., Rapine, R., Ross, A., and Saul, J., 2001: Crustal structure of central Tibet as derived from project INDEPTH wide-angle seismic data, *Geophys. J. Int.*, **145**(2), 486–498, URL http://dx.doi.org/10.1046/j.0956-540x.2001.01402.x.

Appendix A

Dispersion measurements, reference velocities, RMS and χ^2

Period [s]	No. of measurements	Reference vel. [km s^{-1}]	RMS [s]	χ^2
15.15	2990	2.9	4.26	1.91
12.82	3552	2.9	2.89	1.33
11.90	4847	2.9	2.28	1.13
10.99	5671	2.9	1.61	0.96
10.10	5961	2.9	1.05	0.52
9.34	5978	2.9	0.85	0.38
8.62	6040	2.9	0.83	0.39
8.00	6096	2.9	0.79	0.42
7.35	6106	2.9	0.74	0.45
6.80	6202	2.8	0.71	0.53
6.29	6301	2.8	0.69	0.61
5.78	6343	2.8	0.67	0.71
5.35	6504	2.7	0.68	0.89
4.93	6570	2.7	0.66	1.02
4.20	6580	2.7	0.76	1.79
3.89	6511	2.6	0.86	2.57
3.31	6252	2.5	1.00	4.81
2.82	6088	2.4	1.42	10.95
2.40	5963	2.3	1.81	24.47

Table A.1: Number of dispersion measurements, constant reference velocity, RMS and χ^2 for each of the 19 periods used in the ambient seismic noise tomography.

Appendix B

Synthetic S-wave velocity model and post-stack time and space variant filter

B.1 Synthetic S-wave velocity model

It was mentioned in Section 3.2.2 that S-waves are more sensitive to velocity variations than P-waves. That is, they are more affected by wrong stacking velocities than P-waves. It is desired then that the velocity model used for the stacking and depth migration is obtained from the same data set as was used for the seismic processing (R. Ghose, private communication). However, the validation tests done in Section 2.1.3 show that the good resolution of the S-velocity model obtained from the TIPTEQ seismic data reaches only the first kilometres depth. It is possible to use a synthetic velocity model for the NMO correction and depth

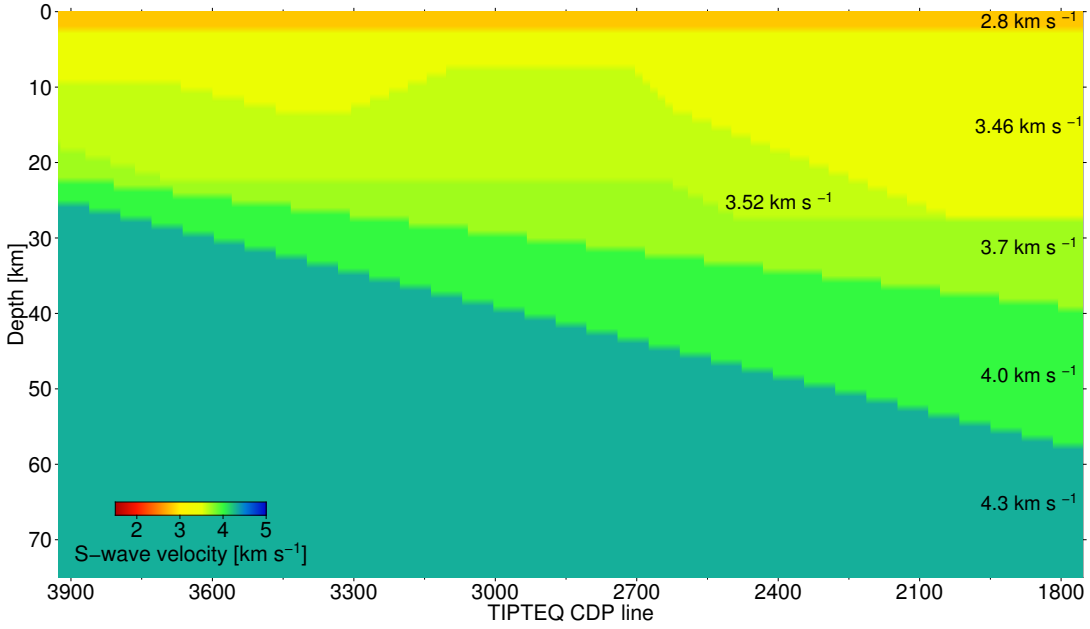

Figure B.1: Synthetic S-wave velocity model used for the normal moveout (NMO) correction and depth migration of S-reflectivity.

migration, so that the velocities of the model allow as constructive a stack as possible. On the other hand, the velocity values have to be in agreement to those obtained in this work (Chapter 2). Fig. B.1 shows the synthetic S-wave velocity model used for the NMO correction (after transforming it in ProMAX to stacking velocities) and depth migration. The model consists of several layers, whose geometry was extracted from Fig. 3.6. The velocities in each layer are constant and their values can be observed in Fig. B.1. This was an interesting test to try, although it did not show much of an improvement with respect to other velocity models present in ProMAX (e.g. the SPOC velocity model from Krawczyk et al., 2006 merged with the model from Micksch, 2008; the model from local earthquake geometry from Haberland et al., 2009 merged with the model from Micksch, 2008, with all of these models divided by $\sqrt{3}$; the S-wave velocity model from Ramos et al., 2016). The tested velocity models yielded similar results, with only small variations of the arrival time windows and intensity of each imaged reflector.

B.2 Post-stack variant bandpass filter

The use of a post-stack time and space variant filter is not uncommon in reflection seismics (Yilmaz, 2001). The Ormsby bandpass filter used to process the S-reflectivity data after stacking consisted of three different CDP-independent filters, so that they spanned larger two-way-time windows for greater offsets. The bandpass filter for the first time interval had corner frequencies 6 - 10 - 35 - 50 Hz (i.e. 0% - 100% - 100% - 0%, with cosine tapers between 0 and 100%), the second was defined as 5 - 8 - 20 - 30 Hz and the last one as 3 - 8 - 15 - 25. The time intervals were 0 - 3 s, 2 - 35 s and 10 - 55 s for smaller offsets. For greater offsets (maximum values were $\sim$40 km) the time intervals for the application of the three bandpass filters were 0 - 4 s, 3 - 40 s and 20 - 55 s.

The aim was to use a filter which passed higher frequencies in the first seconds, so that low-frequency signals become attenuated, at least partially. This is achieved by the first bandpass filter, as can be observed in Figs. B.2 and B.3. The figures show that for both components, NS and EW, noise with high amplitude in the first $\sim$4 s has smaller amplitudes after being filtered. The second and third filters, applied at greater times, pass lower frequencies and were aimed to attenuate high-frequency noise, thus improving the signal-to-noise ratio in general.

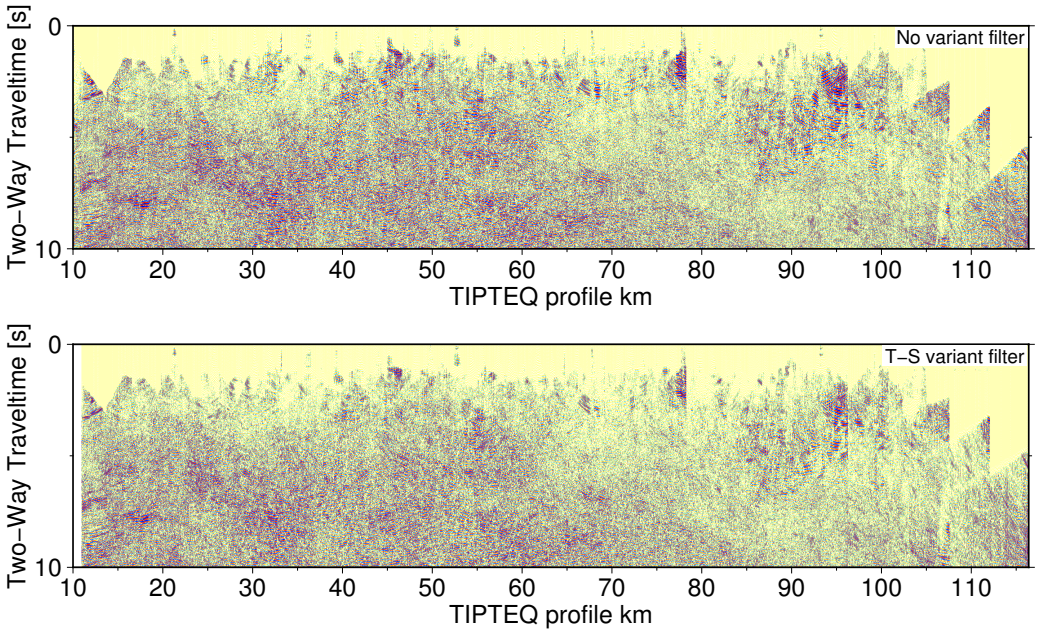

Figure B.2: Comparison between applying a post-stack time and space variant filter (bottom) and not applying a post-stack filter (top). The figure shows the effect in the first 10 s. Radial (east - west) component.

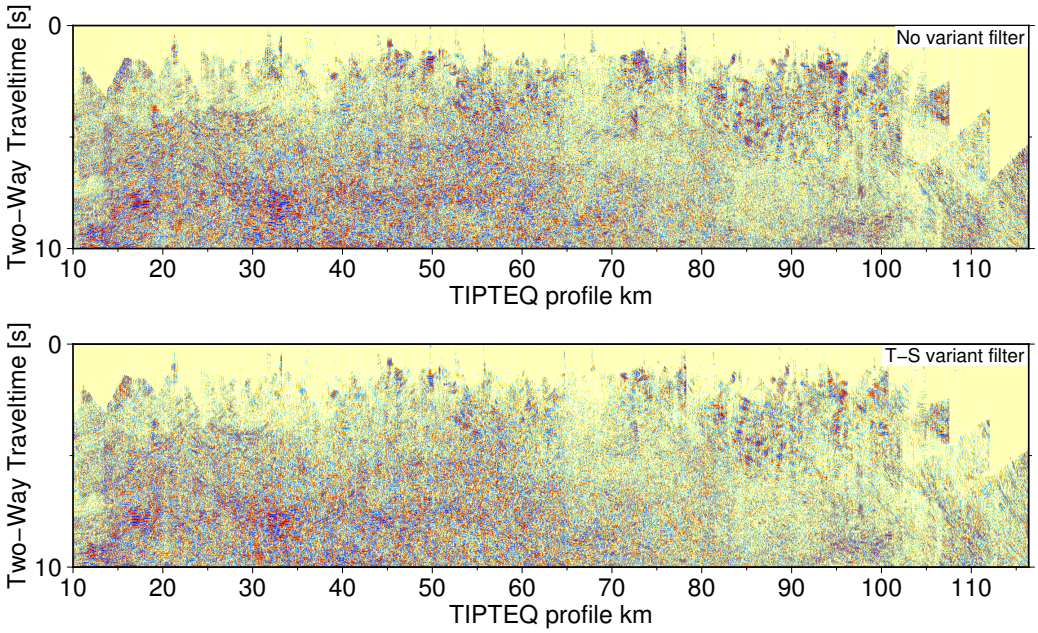

Figure B.3: Comparison between applying a post-stack time and space variant filter (bottom) and not applying a post-stack filter (top). The figure shows the effect in the first 10 s. Transverse (north - south) component.